Development of Numerical Wave Tank Based on Multiphase Flow Model and Its Application to Nonlinear Interaction between Wave and Movable Structure

Han Dinh Ut

Development of Numerical Wave Tank Based on Multiphase Flow Model and Its Application to Nonlinear Interaction between Wave and Movable Structure

Han Dinh Ut

Supervised by

Assoc.Prof. Koji. Kawasaki

Coastal and Ocean Engineering Laboratory
Department of Civil Engineering
Nagoya University
JAPAN

ACKNOWLEDGEMENTS

First of all, I am heartily thankful to my supervisor, Assoc. Prof. Koji Kawasaki, whose encouragement, supervision and support from the preliminary to the concluding level enabled me to develop an understanding of the subject.

I would like to express sincere thanks to Prof. Norimi Mizutani, the Head of Coastal and Ocean Engineering Laboratory at Nagoya University, who gave me knowledgeable advices and recommended valuable materials for this study.

Special appreciation goes to this dissertation committee, which consisted of Assoc. Prof. Koji Kawasaki (Head), Prof. Norimi Mizutani, Prof. Tetsuro Tsujimoto, Nagoya University; and Prof. Shinichi Aoki, Toyohashi University of Technology for their helpful comments, careful review and valuable suggestions on this work.

I also acknowledge the very good research facilities in the Coastal and Ocean Engineering Laboratory at Nagoya University chaired by Prof. Norimi Mizutani and co-chaired by Assoc. Prof. Koji Kawasaki. Moreover, I have learned and experienced a lot from both a serious academic atmosphere in seminars and discussions, and a warm family friendly one in daily life activities at the Coastal and Ocean Engineering Laboratory.

This dissertation would not have been possible without the help of former and present members of the Coastal and Ocean Engineering Laboratory, in particular Assoc. Prof. Kwang-Ho Lee, Assoc. Prof. Tomoaki Nakamura and Dr. Chang-Hoon Kim for their helpful comments, Dr. Masami Kiku and Mr. Kazuki Suzuki for their kind consultancy in computer works, Mr. Toru Funahashi, Mr. Yoshitaka Takasu and Mr. Tetsuya Matsuno for their great cooperation. Heartfelt thanks also go to Mr. Shingo Kuwabara, Ms. Vu Thi Lan Huong, Mr. Peng Wei for their warm friendship.

I extend my gratitude to Prof. Pham Khac Hung, the former Director of Institute of Construction for Offshore Engineering at National University of Civil Engineering, Vietnam, and Assoc. Prof. Dinh Quang Cuong, the Director of the Institute of Construction for Offshore Engineering, for their constant encouragement.

I am grateful to National University of Civil Engineering and Institute of Construction for Offshore Engineering, for granting study leave during the doctor course at Nagoya University (2008~2011). The financial support (Monbukagakusho Scholarship) from the Japanese Government is also highly acknowledged.

Last but not the least, I would like to express my deep sense of gratitude to my parents, Mr. Han Van Luu and Mrs. Nguyen Thi Chien, for bringing me into this world and rising me up, to my beloved wife, Mrs. Nguyen Thanh Tu, and my kids, Binh Nguyen and An Nguyen, for their great love and understanding, and to my sister and brothers for their encouragement and helps in all aspects of my life.

ABSTRACT

Development of Numerical Wave Tank Based on Multiphase Flow Model and Its Application to Nonlinear Interaction between Wave and Movable Structure

In order to explore and exploit natural resources of seas and oceans such as water, food and energy as well as to provide means for transport and other substructures, variety of coastal and offshore structures have been built and utilized. No matter what type they are and what functions they are used for, one thing is common, they are all under wave actions, which have been noted nonlinear, severe in harsh sea conditions, dominant compared with other impacts such as wind and current. Understanding the interaction between wave and structure is therefore, one of the most important requirements to design and install safe, functional and economical coastal/offshore structures. The experimental wave tank has proven its applicability of studying the above-mentioned complex interactions, but its application is limited because of high cost and technical limitations of the experimental facilities. Compared with the experimental wave tank, the numerical wave tank possesses not only advantages such as lower cost, higher efficiency, no reduce-scale effects, but also the large extensibility in the spatio-temporal scale and the controllability. In the present study, this motivation was realized by developing a numerical wave tank model capable of reproducing nonlinear wave-structure interaction for both fixed and movable structures, considering the interaction between air and water phase.

Starting with the idea that the interaction between wave and coastal/offshore structures may be considered as representation of the interaction among the solid phase (structures), the gas phase (air) and the liquid phase (water), a multiphase flow model with solid-gas-liquid interaction proposed by Kawasaki and co-workers (2005~2009) is utilized to develop a numerical wave tank in this study. In the model, the multiphase flow includes liquid phase (water), gas phase (air) and solid phase (rigid body). The flow is represented by one set of governing equations, and no special treatments need for boundary among three phases. In order to realize the numerical wave tank, a non-reflective wave generator employing a source/sink method for wave generation (Brorsen and Larsen, 1987), energy dissipation zone treatments (Cruz et al., 1993; Hinatsu, 1992) are furthermore incorporated in the multiphase flow model. The validity and utility of the proposed numerical wave tank model were then verified by a series of simulations on wave propagation and energy dissipation zone effects, wave propagation over a submerged dike and wave breaking process on the different uniform slopes. More importantly, the proposed model was utilized to analyze the nonlinear interaction between wave and a floating panel for wave overtopping reduction countermeasure proposed by Kawasaki (2011). Good comparisons between the numerical and experimental results in all simulations demonstrated that the proposed numerical wave tank is capable of reproducing the nonlinear interaction between wave and both fixed and movable structures, considering the interaction between air and water phase.

Keywords: Numerical wave tank; Numerical simulation; Multiphase flow model; Nonlinear interaction between wave and structure.

Table of Contents

CHAPTER 1

CHAPTER 2

CHAPTER 3

CHAPTER 4

CHAPTER 1
INTRODUCTION

1.1 Study Background and Motivation

The seas and oceans play a very important role for our world not just because they give the natural beauty for sightseeing but because they contribute to a variety of other resources such as water, food and energy and provide means for transport and other substructures. In order to explore and exploit all these resources indicated in Fig.**1.1**, many vehicle and facilities are required (Moan, 2003). In the field of offshore oil and gas industry, for example, several types of platforms such as fixed platforms, floating platforms and so on have been built, as shown in Fig.**1.2**. On the other hand, in order to protect coastal zones from a threat of storm surge, wave overtopping and erosion, a variety of coastal structures such as vertical seawalls, wave absorbing breakwaters and submerged breakwaters have so far been constructed and installed in coastal sea areas. An overview of the various types of coastal structures and their applications presented in Coastal Engineering Manual (CEM,2003) is shown in Fig.**1.3**. Although owning different structural types as well as being used for different purposes, coastal and offshore structures are all under wave actions. It is known that these actions are very severe in hash sea conditions, random, and dominant compared with other impacts such as wind and current. In order to meet the safe, functional and economical requirements for these structures, one of the most important is that the interaction between waves and structures has to be understood completely.

It is known that when waves propagate from deepwater into shallow region, they shoal, refract, reflect and their profiles may break at certain depths. When encountering coastal structures, some wave energy are dissipated and some energy are reflected. The remaining energy may pass through the structure or pass over structures, cause running-up on the front face of the structures, overtopping the structure crest, generating waves in the lee of structures. For coastal structures having land in their lee, the remaining energy may result in wave overtopping, which possibly produce flooding and possible damage to the area behind the structures (Sorensen, 2006). Moreover, violent fluid motions are observed in many cases such as wave breaking and

Figure **1.1** A sea of development for coastal and ocean engineering (Source: Moan, 2003)

Figure **1.2** Various types of offshore plattform (Source: http:/en.wikipedia/wiki/Oil-plaform)

wave overtopping. as shown in Figs.**1.4**. The interaction between wave and coastal structures are, therefore naturally nonlinear. Laboratory experiments have been considered as a unique approach to understand the real interaction between waves and coastal structures. However, it is known that the effects of this interaction are very dependent on the specific characteristics of coastal structures such as the geometry and the surface roughness. Consequently, although many experimental studies about the characteristics of the interaction between waves and structures have been conducted, the coastal designers still may face problems in determining specific data for their projects. Numerical investigations on the interaction between wave and coastal structures therefore should be required.

On the other hand, it was noted from a number of works (Faltinsen et al., 1995; Swan et al., 1997, Stansberg, 2005; Buchner and Bunnik, 2007; Norsok, 2007) that the strong nonlinear interaction between waves and offshore structures possibly might result in violent impacts such

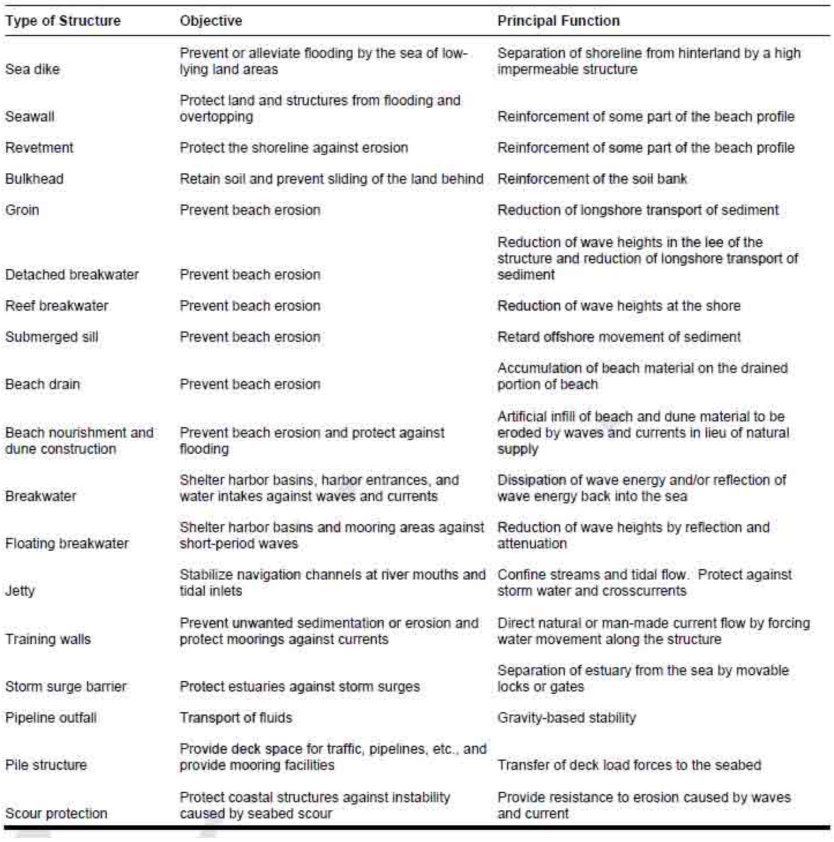

Type of Structure	Objective	Principal Function
Sea dike	Prevent or alleviate flooding by the sea of low-lying land areas	Separation of shoreline from hinterland by a high impermeable structure
Seawall	Protect land and structures from flooding and overtopping	Reinforcement of some part of the beach profile
Revetment	Protect the shoreline against erosion	Reinforcement of some part of the beach profile
Bulkhead	Retain soil and prevent sliding of the land behind	Reinforcement of the soil bank
Groin	Prevent beach erosion	Reduction of longshore transport of sediment
Detached breakwater	Prevent beach erosion	Reduction of wave heights in the lee of the structure and reduction of longshore transport of sediment
Reef breakwater	Prevent beach erosion	Reduction of wave heights at the shore
Submerged sill	Prevent beach erosion	Retard offshore movement of sediment
Beach drain	Prevent beach erosion	Accumulation of beach material on the drained portion of beach
Beach nourishment and dune construction	Prevent beach erosion and protect against flooding	Artificial infill of beach and dune material to be eroded by waves and currents in lieu of natural supply
Breakwater	Shelter harbor basins, harbor entrances, and water intakes against waves and currents	Dissipation of wave energy and/or reflection of wave energy back into the sea
Floating breakwater	Shelter harbor basins and mooring areas against short-period waves	Reduction of wave heights by reflection and attenuation
Jetty	Stabilize navigation channels at river mouths and tidal inlets	Confine streams and tidal flow. Protect against storm water and crosscurrents
Training walls	Prevent unwanted sedimentation or erosion and protect moorings against currents	Direct natural or man-made current flow by forcing water movement along the structure
Storm surge barrier	Protect estuaries against storm surges	Separation of estuary from the sea by movable locks or gates
Pipeline outfall	Transport of fluids	Gravity-based stability
Pile structure	Provide deck space for traffic, pipelines, etc., and provide mooring facilities	Transfer of deck load forces to the seabed
Scour protection	Protect coastal structures against instability caused by seabed scour	Provide resistance to erosion caused by waves and current

Figure **1.3** Clasiffication of coastal structures (Source: Coastal Engineering Manual, 2003)

(a) Wave breaking

(b) Wave Overtopping

Figure **1.4** Violent fluid motion on coastal structures (Source: a) http://www.nrc-cnrc.gc.ca/eng/ibp/chc/coastal/structures.html; b) http://www.mlit.go.jp/hkb/river-e.html)

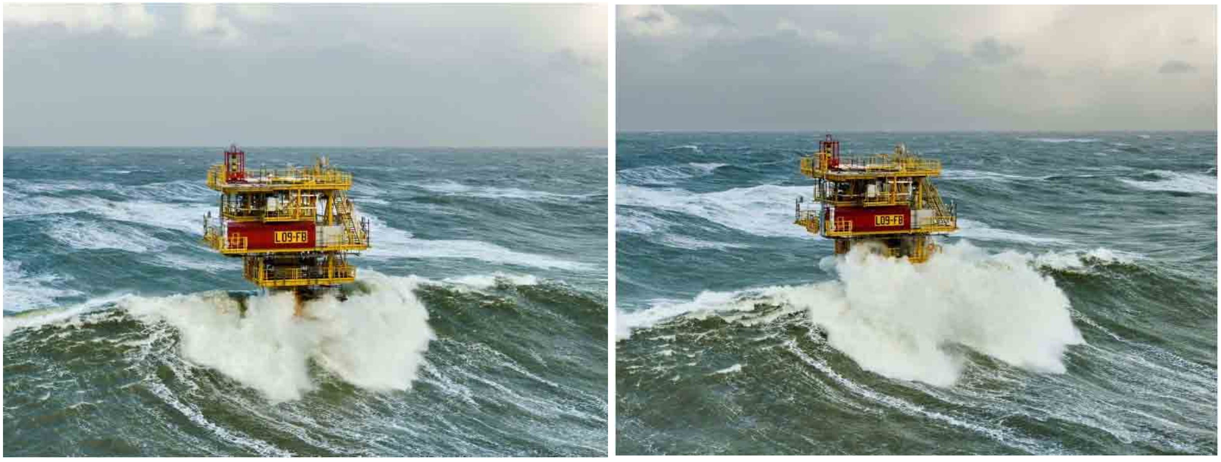

Figure **1.5** interaction between extreme wave and a fixed offshore structure (Source: Buchner, 2007)

Figure **1.6** Green water on a ship under extreme wave (Source: Buchner, 2007)

as slamming, green water on deck and ringing which can damage to the strength of offshore structures and the operation of the facilities on the top side of the offshore platforms. Some of these impacts are shown in Figs.**1.5** and **1.6**. Moreover, Sheikh and Swan (2005) presented new laboratory observations concerning the interaction between a series of steep incident waves and a vertical, surface-piercing column. It was shown from their study that if the incident wave were steep, a strong and apparently localized interaction was clearly observed at water surface. This, in turn, resulted in the scattering of high frequency waves, which could produce a significant increase in the maximum crest elevation relative to those in the absence of the structure. They concluded that this complex phenomenon was caused by the nature of wave-structure interaction as well as nonlinear wave interaction. It is also noted from Buchner and Bunnik (2007) that in case of the movable structures such as floating offshore structures, the relative motion of structure under wave action was very important factor in determining the effects of wave-structure interaction.

Moreover, Moan (2005) and Moan (2007) reviewed important developments regarding safety management of offshore structure, accidents and near-misses in the offshore oil and gas industry. It was shown from his works that the hazards were caused by a technical-physical and/or human and organizational issues. For both issues, an improvement of knowledge about wave-structure interaction was considered as a means to control the hazards and associated risks, meaning the improvement of the reliability of structures.

It is demonstrated from the above-mentioned discussions that it is necessary to develop numerical models for simulating the real wave-structure interaction. The laboratory experiment with wave flume or wave basin is the most practical approach but its application is limited because of high cost and technical limitations of the experimental facilities. Compared with the laboratory experiment, the numerical simulation possesses advantages such as lower cost, higher efficiency and so on. Turn back that the interaction between air and water as well as the relative motions of the structure (in case of a movable structure) should be considered in order to realize the interaction between wave and the structure. The motivation of this study is, therefore, to develop a numerical wave tank model capable of reproducing wave-structure interaction for both fixed and movable structures considering the interaction between air and water phase.

Sea level rise is now acknowledged as a real threat to coastal zones. Additionally, the global climate change increasingly causes frequency and severity of storms. As a result, coastal areas are at risk of ocean-related disasters such as tsunami, wave overtopping, flooding and so on. A countermeasure for wave overtopping reduction including a vertical seawall and a floating panel installed in the steel frame, which is attached at the upright of the seawall, newly proposed by Kawasaki et al. (2011), as shown in Figs.**1.7**, may be considered as an useful adaptive solution for preventing coastal zones from above-mentioned disasters. However, wave overtopping reduction performance of this countermeasure should be numerically investigated to confirm experimental results as well as to obtain the further parameters, which has not completely achieved in the laboratory experiments such as the water surface field around the system, wave pressure acting on the front and back sides of floating panel. It is expected that these challenges could be realized by the proposed model.

1.2 Literature Survey

It is known that wave impacts on coastal and offshore structures are generally dominant compared with other impacts such as wind and current. A good understanding of the mechanism

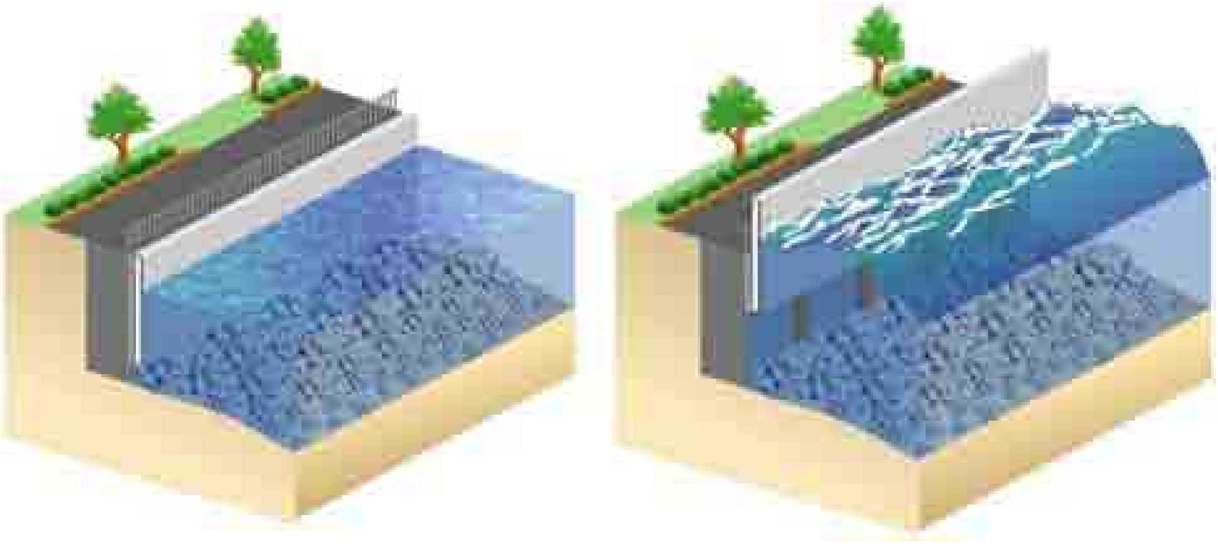

(a) Under calm condition

(b) Under wave action

Figure **1.7** A wave overtopping reduction countermeasure using a floating panel

of the wave-structure interaction therefore will help the coastal and offshore designer giving suitable design solutions in order to meet both the safe and economical requirements for the structures. Because of this reason, several experimental, analytical and numerical studies on the nonlinear interaction between wave and structure therefore have been preformed in literature. Among them, researchers have been developed numerical wave tanks (NWT) in order to reproduce as closely as possible the interaction between wave and structures. In this section, some aspects of NWT such as the generation of the wave in the NWT and NWT's applications are reviewed. Further information could be found in Kim et al. (1999), Tanizawa (1999), Idelsohn (2006) and Ma et al. (2009).

It was noted from Kim et al. (1999) that the methods of wave generation in a NWT were categorized into five options as follows. The first one was the generation of " space periodic waves " , which was firstly proposed by Longuet-Higgins and Cokelet (1976). In their study, the evolution of steady progressing waves was treated by imposing space-periodic boundary conditions for the wave at the walls of the tank. No open boundary conditions were therefore required. A similar work was also found in Xu and Yue (1992). In the second one, wave was generated by the implement of " user-prescribed motions " at tank wall. Following this idea, the piston-type wave maker, flap-type wave maker and plunger-type wave maker were employed (Grilli et al., 1989; She et al., 1992; Kashiwagi et al., 2000). " Feeding velocity on inflow boundary " was named for the third option, in which the fluid in the wave tank was initially at rest and the numerical velocity or velocity potential of Stokes 2nd-order or solitary waves were imposed at the inflow boundary (see Boo et al., 1994). In the fourth option, a prescription of incident wave field was implemented in the numerical wave tank whereas a time marching simulation was started smoothly and a ramp function was applied to the boundary condition (Ferrant, 1995). In the last option, a “ discrete set of singularity ” was introduced. The characteristics including strength and position were set up by the user (Brorsen and Larsen, 1987; Ohyama and Nadaoka, 1991)

Various numerical wave tanks have been widely applied to investigate the wave-structure interaction with both fixed and floating bodies. For the former problem, Ohayama and Nadaoka (1994) studied transformation of a nonlinear wave train passing over a submerged rectangular obstacle by using a NWT developed by the authors (see Ohayama and Nadaoka , 1991), in which two absorption filters were proposed at both ends of the computational domain, and a non-reflective wave generator introduced by Brorsen and Larsen (1987) was also incorporated in the computational domain. Zhang et al. (1996) applied a Mixed Eulerian-Laragian (MEL) boundary intergral scheme, which was originally proposed by Longuet-Higgins and Cokelet (1976), to simulate plunging wave impact on a vertical wall. In their study, a computational tank included a piston wave maker at one end, and a rigid vertical wall on the other end. For the latter problem, Shirakura et al. (2000) investigated interaction between wave and floating body by three-dimensional (3D) wave tank. In their studies, a Quadratic Boundary Element Method (QBEM) was used to solve velocity and acceleration field considering the interaction between wave and motions of floating body. Recently, Ma and Ya (2009) developed the Quasi Arbitrary Laragian-Eulerian Finite Element Method (QALE-FEM) based on a fully nonlinear potential theory to simulate nonlinear responses of 3D moored floating bodies to steep waves. In their numerical wave tank, the wave maker was setup on the left side of the domain and a damping zone with a Sommerfeld condition was applied at the right side of the computational domain (see Ma et al., 2001 for detail). It was further found from their studies that numerical results were well agreement with experimental results.

Through the above-mentioned investigations, it can be said that numerical studies have obtained impressive results in analyzing nonlinear interaction between wave and both fixed and floating bodies. However, it should be noted that all numerical models were solved based on the potential theory for an ideal fluid with the assumption is that viscosity is neglected. Therefore, their applications may not be suitable in case of the rotational flows as well as vortex forms, which have been reported where wave breaks or near breaks, and where the bodies are not large compared with wave length. To overcome this limitation, several studies based on solving the Navier-Stokes equation, in which the viscosity effects were involved, have been proposed. In this approach, the pioneer works were presented by Welch et al (1965) for marker and cell (MAC) method and Hirt and Nichols (1981) for volume of fluid (VOF) method. In the MAC method, virtual market particles were used to track the free surface, whereas in the VOF method, the free surface was reconstructed by a use of volumes of fluid in computational cells. Compared with MAC method, the implementation of VOF was easier and less computationally intensive (see Ashgriz and Poo, 1991), therefore many researcher have used the VOF method to simulate fluid motion. Among them, Kawasaki (1998) is the pioneer incorporating the VOF method into a numerical wave tank to study the interaction between wave and impermeable structures. In his study, the non-generation source introduced by Brorsen and Larsen (1987) was used for wave generator, and the added dissipation zones proposed by Hinatsu (1992) and an open boundary treatment were combined in the numerical wave tank. Hur (2000) expanded Kawasaki's model by using a porous model to study the interaction between wave and permeable submerge breakwater. All these studies, however, were based on sing-phase flow models, in which the effect of air movement on the surface was neglected. Consequently, the trapped air bubbles inside the water as well as the splash water in the air might not fully treated when the interaction between wave and structure results in violent surface such as wave breaking or wave overtopping.

To deal with water-air interaction, some studies have been proposed recently. Hieu and Tanimoto (2006) presented a VOF-based two-phase flow model for studying wave breaking and wave-structure interaction. The numerical results were compared with not only the experimental one (conducted by King and Kirby, 1994) but the numerical results simulated by some previous sing-phase models such as CADMAS-SURF model (2001) and Zhao et al. (2004). It was found from the comparisons that the presented model could provide accurate numerical results. Furthermore, the simulated results by the presented model are much more accurate than those by using CADMAS-SURF model and others. Noted that CADMAS-SURF model was known as one of the most accurate sing-phase flow models for simulating the interaction between wave and coastal structures, the author concluded that the incorporation of air motion in their model had contributed significant improvement to the accuracy of reproducing wave breaking, and therefore the effect of air movement on the wave motion under wave breaking process should be considered. On the other hand, the applicability of the above-mentioned studies in analyzing the interaction between wave and movable structures has not been addressed.

Further review is discussed at beginning of relevant chapter in this dissertation.

1.3 Study Objectives and Scopes

As discussed above, it is necessary to develop a numerical wave tank capable of simulating the nonlinear interaction between waves and both fixed and movable structures, considering the interaction between air and water phase. In order to realize this target, a numerical wave tank based on a multiphase flow model with solid-gas-liquid interaction is proposed in this study. The specific content of this study are as follows,

- Develop a numerical wave tank;
- Verify the validity and utility of the proposed numerical wave tank;
- Apply the proposed numerical wave tank to analyze the nonlinear interaction between wave and a floating panel for wave overtopping reduction;

Although a three-dimensional wave tank is developed, all investigations are conducted in the frame of two-dimensional applications. Investigations on three-dimensional applications such as the generation of multi-direction wave, nonlinear interaction between wave and a three-dimension floating body and so on will be addressed in subsequent studies.

1.4 Thesis Outline

The present study develops a numerical wave tank capable of reproducing nonlinear wave-structure interaction by using a multiphase flow model with solid-gas-liquid interaction. The content of this thesis is summarized as follows,

Chapter 2 develops a numerical wave tank model based on a multiphase flow model with solid-gas-liquid interaction and verifies its validity and utility. First, a literature survey about multiphase flow studies on wave-structure interaction is introduced. The formulations of the multiphase flow model and numerical solutions are then addressed. In order to realize a numerical wave tank, a “ source ” to generate waves is established in the computational domain by a use of a non-reflective wave generator presented by Kawasaki (1998), energy dissipation zone treatments (Cruz et al., 1993; Hinatsu, 1992) representing for wave absorber are employed to prevent wave reflection from open boundaries, and the tangent transformed CIP proposed by Yabe and Xiao (1993) is used to capture interfaces among phases. In the verification part of the proposed numerical wave tank, wave propagation and effect of energy dissipation zone in the numerical wave tank are first examined to verify the validity of non-reflective wave generation method and numerical treatments of energy dissipation zones. The validity and utility of the numerical wave tank in reproduce nonlinear interaction between wave and a fixed structure, considering the interaction between air and water phases is then investigated through applications for analyzing wave propagation over a submerged dike and simulating wave breaking process on different uniform slopes.

Chapter 3 discusses nonlinear interaction between wave and a floating panel for wave overtopping reduction. First, the data of laboratory experiment is analyzed to identify key characteristics of the wave overtopping reduction countermeasure. Next, numerical study is then conducted. In order to consider the influence of the friction force induced by the collision between the floating panel and the steel frame on the floating panel motion, a damping term was introduced into the motion equation of floating panel in the vertical direction. The numerical model with modified equation of motion is then used to investigate characteristics of the countermeasure for wave overtopping reduction and verify the experimental results. The pressure acting on the side of the floating panel, which has not obtained in the laboratory experiment is further examined.

Finally, an overview of the main conclusions of this study and the recommendation for future research are presented in Chapter 4.

The flow chart of the present dissertation is shown in Fig.**1.8**

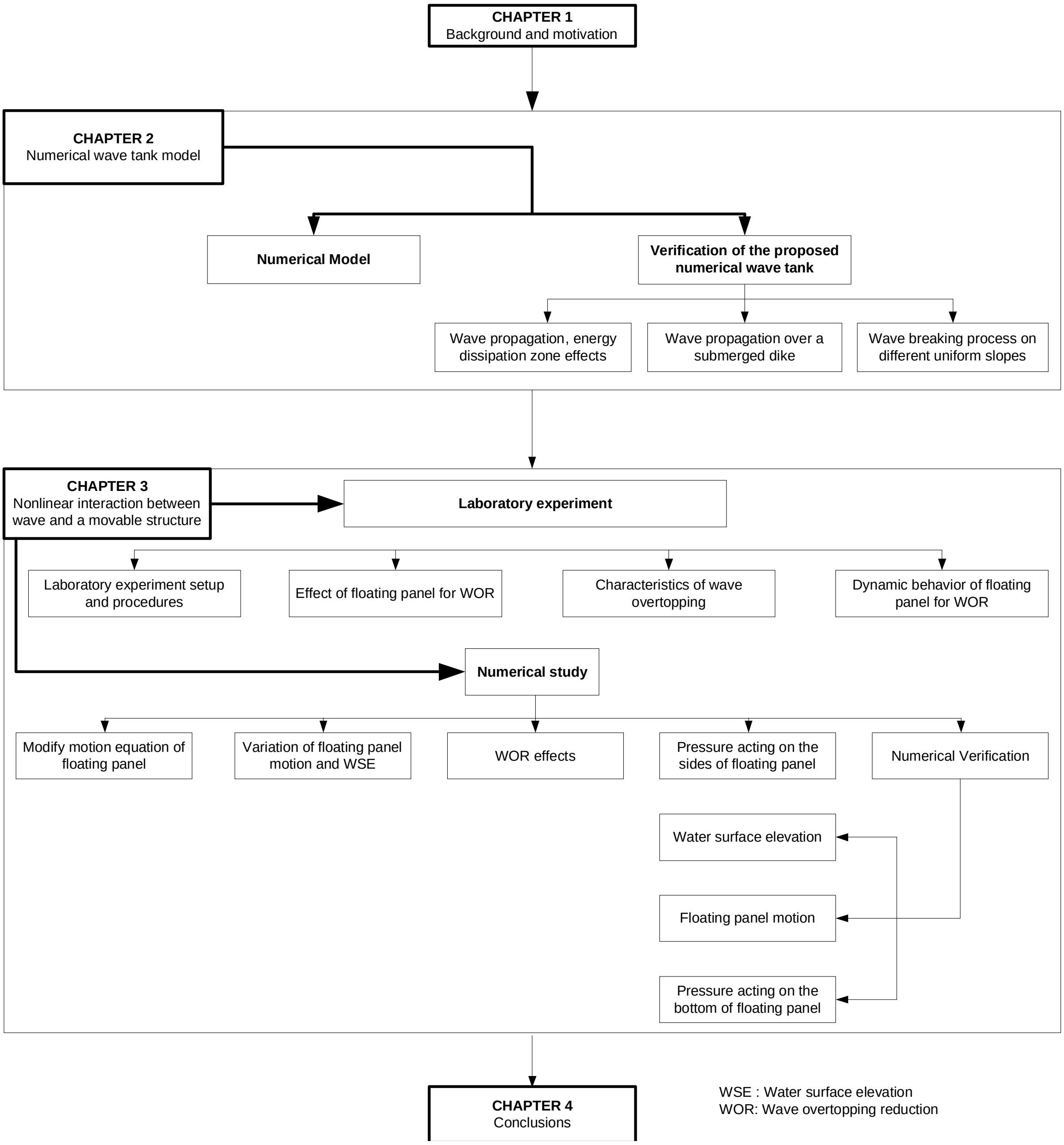

Figure **1.8** Flow chart of the present dissertation

CHAPTER 2
NUMERICAL WAVE TANK MODEL

2.1 General

Starting with the concept that the interaction between waves and structures in coastal and ocean fields may be considered as a representation of the interaction among the solid phase (structures), the gas phase (air) and the liquid phase (wave, water), a numerical model can well reproduce complex wave-structure interaction if all phases are treated in the model. Therefore, this study pursues a multiphase flow model with solid-gas-liquid interaction in order to realize the NWT model. The term “ multiphase flow ” is used to refer to any fluid flow consisting of more than one phase or component (Brennen, 2005).

Various multiphase flow studies have been applied to coastal and ocean field, chemical environmental processes and so on. However, for coastal and ocean applications, only some studies about the interaction between waves and structures have been introduced since a decade ago. Kawasaki (2005a) and Kawasaki (2005b) developed two- and three-dimensional numerical models of multiphase flow by employing a CIP (Cubic Interpolated Propagation) method and an extended SMAC (Simplified Marker And Cell) method in order to analyze complex physical phenomena with solid-gas-liquid interaction. Kawasaki and Hakamata (2006) proposed a new two-dimensional numerical model of solid-gas-liquid phase flows by improving the computational algorithm to resolve mass conservation problem and introducing a LES (Large Eddy Simulation) based on the Smagorinsky model. Furthermore, Kawasaki and Mizutani (2007) confirmed the utility and validity of the model by comparing the numerical results with the experimental ones regarding wave pressures acting on rigid bodies under bore action, which was induced by the collapse of a water column. However, the model has been limited to the numerical analysis of dynamic behavior of only one rigid body. Kawasaki and Ogiso (2009) developed a three-dimensional solid-gas-liquid phase flow model in order to analyze the dynamic behavior of multiple rigid bodies. The previous models have achieved in some applications, but still have some problems relating to the conservation of mass. These models also have not had the functions of a numerical wave flume including wave generator and non-reflective boundary treatment. Hu and Kashiwagi (2004) introduced another two dimensional numerical model based on the CIP method for simulating violent free surface. It is shown from their study that multiphase flow also includes liquid (water), gas (air) and solid (floating body) phases as in Kawasaki (2005a, 2005b), however, a wave-maker was newly assumed as a solid phase and a dissipation zone treatment for boundaries was considered, so functions of a numerical wave tank were established. Zhu et al. (2005) and Hu et al. (2005) developed this model to investigate interaction between waves and a horizontal circular cylinder, and to simulate dynamic behavior of freely floating body under wave action. These studies have shown good results, but it was noted that the numerical wave tank may encounter difficulties in analyzing the large amplitude motions for long time simulations (Zhu, 2006).

In this chapter, a multiphase flow model proposed by Kawasaki and co-workers is chosen to develop a NWT model. In order to enhance the computational accuracy, a CIP-CSL2 (Constrained Interpolation Profile- Conservative Semi-Lagragian 2) method and the third-order Adams-Bashforth scheme are incorporated in the numerical model. Moreover, a non-reflective wave generator proposed by Kawasaki et al. (1998), and energy dissipation zone treatments presented by Cruz et al (1993) and Hinatsu (1992) are employed in order to realize the numerical wave tank.

This chapter starts with the formulations of multiphase flow model with solid-gas-liquid interaction, the computational algorithm and numerical methods for solving the formulations. A “ source ” to generate waves and dissipation zone treatments to prevent the reflection from boundary are then presented. Next, a series of simulations are conducted to verify the validity and utility of the proposed numerical wave tank model. The chapter ends with some conclusions.

2.2 Numerical Wave Tank

A schematic sketch of the proposed NWT is shown in Fig.**2.1**. As found in this figure, a source to generate waves is introduced in the analysis zone, whereas energy dissipation zones are added at both sides of the computational domain. Detailed explanation of wave generation and energy dissipation zones will be presented at next sections.

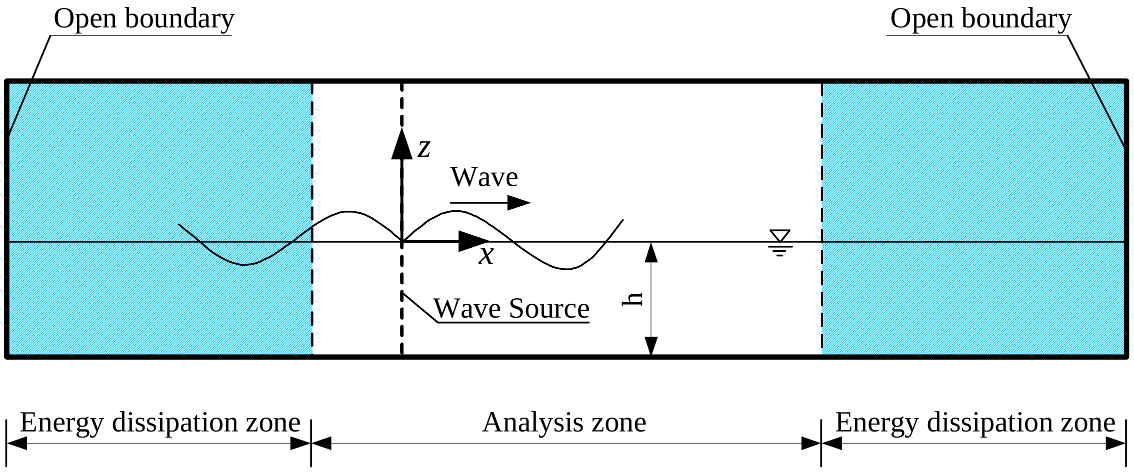

Figure **2.1** Schematic sketch of the proposed NWT

2.3 Numerical Model

2.3.1 Governing Equations

The governing equations consist of the conservation equation of mass Eq.(2.1), the Navier-Stokes equations Eq.(2.2), the pressure equation for compressible fluid Eq.(2.3), the advection equation of density functions Eq.(2.4) and the equation of state for barotropic fluid Eq.(2.5). The equations allow us to precisely compute not only incompressible but also compressible multiphase flows.

$$\frac{\partial \rho}{\partial t} + \frac{\partial \left(u_j \rho\right)}{\partial x_j} = \rho q \tag{2.1}$$

$$\frac{\partial u_i}{\partial t} + u_j \frac{\partial u_i}{\partial x_j} = -\frac{1}{\rho}\frac{\partial p}{\partial x_i} + g_i + \frac{f_{si}}{\rho} + \frac{\partial}{\partial x_j}\left(-\tau_{ij} + 2\frac{\mu}{\rho} S_{ij}\right) - D_i u_i \tag{2.2}$$

$$\frac{\partial p}{\partial t} + u_j \frac{\partial p}{\partial x_j} = -\rho C_{ls}^2 \left(\frac{\partial u_j}{\partial x_j} - q\right) \tag{2.3}$$

$$\frac{\partial \phi_I}{\partial t} + u_j \frac{\partial \phi_I}{\partial x_j} = 0 \tag{2.4}$$

$$\rho = f(p) \tag{2.5}$$

$$q = \begin{cases} 0 & (x \neq x_s) \\ q^* & (x = x_s) \end{cases} \tag{2.6}$$

where, x_i is position vector (x, y, z), u_i is velocity component in the direction of i, ρ is fluid density, p is pressure, g_i is gravitational acceleration vector $(0, 0, -g)$, f_{si} is surface tension term,

τ_{ij} is turbulence term, μ is the coefficient of viscosity, S_{ij} is strain rate tensor $(\partial u_i/\partial x_j+\partial u_j/\partial x_i)$, D_i is dissipation coefficient used in added dissipation zones, C_{ls} is local sound speed, t is time and ϕ_I ($I = 1\sim3$) are density functions for respective phases (ϕ_1: solid phase; ϕ_2: liquid phase; ϕ_3: gas phase) that represent the rate of fractional volume for each phase in a cell and these functions need to satisfy the relationship: $\phi_1 + \phi_2 + \phi_3 = 1 \ \ (0 \le \phi_I \le 1)$ in a cell, $q = q\,(y, z, t)$ is wave generation source with its strength q^* assigned only at source line ($x = x_s$).

2.3.2 The Fractional Step Approach

By making use of the fractional step approach, the governing equations including the conservation of mass, the Navier-Stokes equations, and the pressure equation Eqs.(2.7)$\sim$(2.11) are divided into an advection step and a non-advection step. The CIP method developed by Yabe and Aoki (1991) is used to calculate the hyperbolic equations for all variables at the advection step, while equations at the non-advection step are solved with an extended SMAC method proposed by Kawasaki (2005a), which can simulate both compressible and incompressible fluid.

[Advection Step]

$$\frac{\partial u_i}{\partial t} + u_j \frac{\partial u_i}{\partial x_j} = 0 \tag{2.7}$$

$$\frac{\partial p}{\partial t} + u_j \frac{\partial p}{\partial x_j} = 0 \tag{2.8}$$

[Non-Advection Step]

$$\frac{\partial u_i^{n+1}}{\partial t} = -\frac{1}{\rho^n} \frac{\partial p^{n+1}}{\partial x_i} + F_i^* \tag{2.9}$$

$$\frac{\partial p^{n+1}}{\partial t} = -\rho^n C_{ls}^2 \left(\frac{\partial u_j^{n+1}}{\partial x_j} - q \right) \tag{2.10}$$

$$\frac{\partial \rho^{n+1}}{\partial t} + \frac{\partial \left(u_j^{n+1} \rho^{n+1} \right)}{\partial x_j} = \rho^{n+1} q \tag{2.11}$$

Where, the superscript $*$ and $n + 1$ respectively represent the time step after the advection step and the next time step, F_i^* represents external force term in the right hand side of Eq.(2.2) such as gravity , viscous, surface tension and dissipation zone terms.

In this model, the resultant equations are discretized by employing non-uniform staggered mesh grids, as shown in Fig.**2.2**. The velocities are defined on the grids, whereas the other physical quantities are defined at the center of the cells. By using the non-uniform grid, the computational load can be reduced.

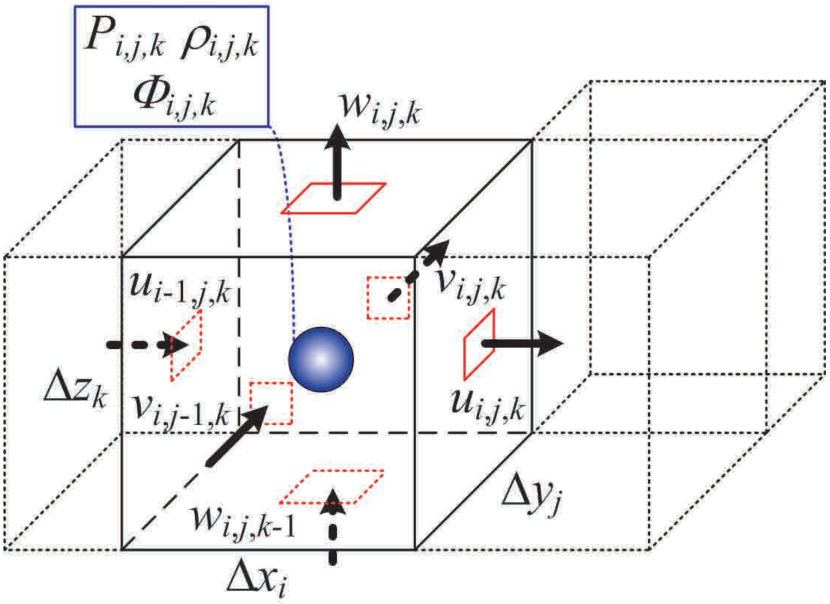

Figure **2.2** Definition of the three dimensional non-uniform staggered grid

2.3.3 Computational Algorithm

Fig.**2.3** presents the computational procedure of the numerical model. At first, the initial and boundary conditions are set up and the wave source strength is distributed at all cells in the computational domain. Next, the advection equations are solved by the CIP method to get all variables. At the non-advection phase, by making use of the resultant variables after the advection step, the extended SMAC method is applied to obtain all physical variables at the next time step. The effect of surface tension on the gas-liquid interface is evaluated by using a CSF (Continuum Surface Force) model presented by Brackbill et al. (1992), which interprets surface tension as a continuous mass force across the interface. A LES (Large Eddy Simulation) based on a DTM (Dynamic Two-parameter Mixed) model developed by Salvetti and Banerjee (1995) is applied for estimating turbulence quantities. After calculating the non-advection phase, the conservative equation with the updated velocity variables is solved by CIP - CSL2 (Constrained Interpolated Profile - Conservative Semi-Lagrangian-2) proposed by Nakamura et al. (2000). Finally, all physical quantities are updated after the calculation of the positions of multiple rigid bodies at the next time step is finished.

By applying the above-mentioned procedure, the numerical model might be assumed as a numerical multiphase turbulence model, which can simulate the dynamic behavior of the solid-gas-liquid interaction.

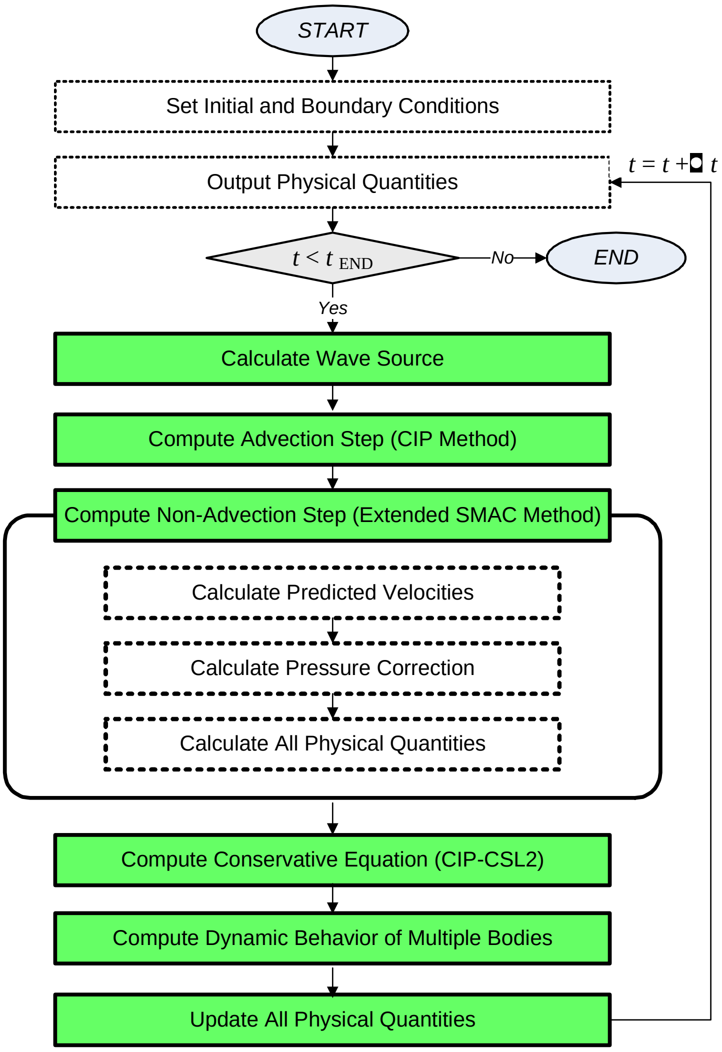

Figure **2.3** Flow chart of the multiphase flow model

2.4 Numerical Solutions at the Advection Step

Various CIP schemes are used for solving governing equation in the advection step. Therefore, this section will start with a brief review of the CIP scheme development.

2.4.1 Development of CIP Schemes

Takewaki et al. (1984) proposed a new cubic-polynomial interpolation method for solving hyperbolic-type equations, where the gradient of the quantity is a free parameter, which may be corrected by using the values of quantity in order to get low diffusion and stable results.

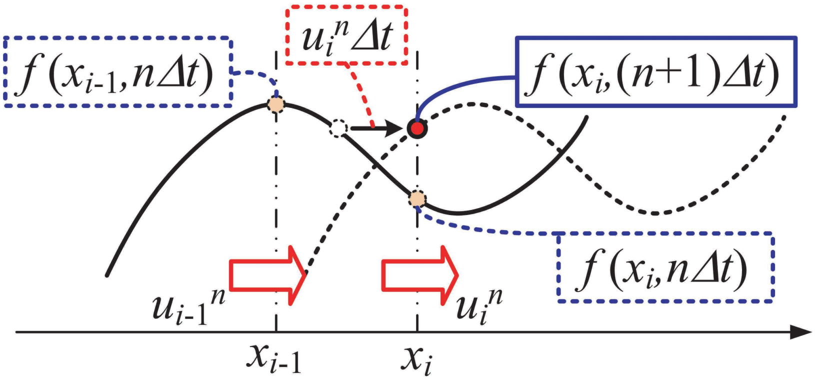

Figure **2.4** Concept of one-dimensional CIP Scheme

The scheme uses a Cubic polynomial for Interpolating the Propagation of the quantity and its spatial derivative so it was named the “ CIP ” scheme from that time on. Yabe and Aoki (1991) proposed a compact CIP scheme (type A-CIP scheme) for solving general hyperbolic equations in one dimension. The scheme divides the equations into advection and nonadvection phases. The nonadvection phase is solved with a finite-difference method whereas the advection phase uses a spatial profile interpolated with a cubic polynomial within a grid cell by assuming that both a physical quantity and its spatial derivative obey the master equation. Yabe et al. (1991) extended straightforward the one-dimensional compact CIP scheme to two and three dimensional scheme (type 2A and 3A-CIP scheme). Nakamura and Yabe (1999) proposed a new CIP method in which multi dimensional case is extended from one dimension by using time splitting technique for solving the hyper-dimensional Vlasov-Poisson equation in phase space. The method was found easy to program in multi dimensions and guarantee mass conservation, however, it is difficult to directly apply this scheme for solving general hyperbolic equations (Nakamura et al., 2001). Yabe et al. (2000) developed conservative semi- Lagrangian scheme called CIP-CSL2 for solving hyperbolic equations in one dimension, in which an additional constraint condition of cell integrated value (mass) is incorporated in the CIP method to construct the interpolation functions. This CIP-CSL2 scheme is then extended for multi-dimensional hyperbolic equations with directional splitting technique by Nakamura et al. (2000). It is stated that the newly CIP-CSL2 scheme provides high accuracy and low diffusion with guaranteeing exact mass conservation.

2.4.2 The Type-A CIP Scheme

(1) One-dimensional CIP Scheme

Yabe and Aoki (1991) presented the CIP scheme for solving the advection equation precisely, taking advantage of the hyperbolic equation, as shown in Eq.(2.12), which indicates one dimensional advection equation of a physical quantity f with the velocity u in the propagation direction x. The concept of the 1-D (one-dimensional) CIP scheme is based on an assumption of $f(x,t) = f(x-ut,0)$, as described in Fig.**2.4**. As shown in Fig.**2.4**, the physical quantity at the next time step $f\left(x_i,(n+1)\Delta t\right)$ can be interpolated from the physical quantity at the present step $f\left(x_i - u_i\Delta t, n\Delta t\right)$ in the range of the interval $[x_{i-1}, x_i]$.

On the other hand, if we differentiate Eq.(2.12) with the variable x, Eq.(2.13) is obtained, in which f_x stands for the spatial derivative of f in x direction. In the simplest case, where the velocity u is constant, the right hand side of Eq.(2.13) becomes 0. Therefore, Eq.(2.13) coincides with Eq.(2.12) and represents the propagation of f_x with the velocity u. By these equations, we can trace time evolution of f and f_x.

$$\frac{\partial f}{\partial t} + u\frac{\partial f}{\partial x} = 0 \tag{2.12}$$

$$\frac{\partial f_x}{\partial t} + u\frac{\partial f_x}{\partial x} = -\frac{\partial u}{\partial x} f_x \tag{2.13}$$

When both the values of f_i and its spatial derivative f_{ix} are given at two grid points, the profile between these points can be interpolated by a cubic polynomial, as shown in Eq.(2.14)

$$F_i\left(x\right) = A1_i X^3 + A2_i X^2 + A3_i X + A4_i \tag{2.14}$$

where, $X = x - x_i$.

The profile at time step after the advection step $*$, is then obtained by shifting the profile at the time step t^n by $u\Delta t$, as shown in Eq.(2.15) and Eq.(2.16).

$$f_i^* = F\left(x_i - u\Delta t\right) = A1_i\xi^3 + A2_i\xi^2 + f_{xi}\xi + f_i \tag{2.15}$$

$$f_{xi}^* = dF\left(x_i - u\Delta t\right)/dx = 3A1_i\xi^2 + 2A2_i\xi + f_{xi} \tag{2.16}$$

where, $\xi = -u\Delta t$. The four unknown coefficients in Eq.(2.14) are determined in Eq.(2.17)$\sim$

(2.20) as follows:

$$A1_i = \frac{f_{xi} + f_{xim1}}{\Delta x_i^2} + \frac{2\left(f_i - f_{im1}\right)}{\Delta x_i^3} \tag{2.17}$$

$$A2_i = \frac{3\left(f_{im1} - f_i\right)}{\Delta x_i^2} - \frac{2\left(f_i - f_{im1}\right)}{\Delta x_i^3} \tag{2.18}$$

$$A3_i = f_{xi} \tag{2.19}$$

$$A4_i = f_i \tag{2.20}$$

where, $\Delta x_i = x_{im1} - x_i$, $im1 = i - sign(u)$. f_i, f_{i-1}, f_{xi} and f_{xi-1} stand for $F\left(x_i\right), F\left(x_{i-1}\right), F_x\left(x_i\right)$, $F_x\left(x_{i-1}\right)$ respectively. In the steady flow, the velocity u is constant and therefore the advection equation can be solved by the above calculation. However, in the real flow where the velocity u varies spatially, the right hand side of Eq.(2.13) can not be neglected. For such cases, Eq.(2.13) is divided into Eq.(2.21) and Eq.(2.22). The non-advection part of Eq.(2.21) is solved by Eq.(2.22), in which the finite difference method is used. The updated value f_x^* is obtained after solving Eq.(2.21).

$$\frac{\partial f_x^n}{\partial t} + u\frac{\partial f_x^n}{\partial x} = 0 \tag{2.21}$$

$$\frac{\partial f_x^{ad}}{\partial t} = -f_x^*\frac{\partial u}{\partial x} \tag{2.22}$$

The key the CIP scheme is in the way of determining a physical quantity and its of the spatial derivative. First, a physical quantity and its spatial derivatives are taken as dependent variables to construct a profile. Consequently, a cubic polynomial can be determined by making use of the information at grid points of only a grid cell. Moreover, the use of spatial derivatives makes the profile inside a grid cell well-constructed. This means that in order to obtain a given computational accuracy, the CIP scheme may need the number of grid points less than those required by other high-order schemes.

(2) The Type 3A-CIP Scheme

As mentioned above, one-dimensional type A-CIP (1A-CIP) can be extended into three-dimensional (3A-CIP) in a straightforward way. The advection equation of a physical quantity f in three-dimensional Eq.(2.23) is derived with respect to x, y, z in order to achieve the governing equation for its spatial derivatives $\frac{\partial f}{\partial x_j}$, as shown in Eq.(2.24),

$$\frac{\partial f}{\partial t} + u_j\frac{\partial f}{\partial x_j} = 0 \tag{2.23}$$

$$\frac{\partial}{\partial t}\left(\frac{\partial f}{\partial x_i}\right) + u_j\frac{\partial}{\partial x_j}\left(\frac{\partial f}{\partial x_i}\right) = -\frac{\partial u_j}{\partial x_i}\left(\frac{\partial f}{\partial x_j}\right) \tag{2.24}$$

The profile for f is derived by the procedures similar to one dimension, as shown in Eq.(2.25)

$$\begin{aligned} F_{i,j,k} = {} & [(C1_{i,j,k}X + C2_{i,j,k}Y + C3_{i,j,k}Z + C4_{i,j,k})X + C5_{i,j,k}Y + f_{xi,j,k}]X \\ & +[(C6_{i,j,k}Y + C7_{i,j,k}Z + C8_{i,j,k}X + C9_{i,j,k})Y + C10_{i,j,k}Z + f_{yi,j,k}]Y \\ & +[(C11_{i,j,k}Z + C12_{i,j,k}X + C13_{i,j,k}Y + C14_{i,j,k})Z + C15_{i,j,k}X + f_{zi,j,k}]Z \\ & +C16_{i,j,k}XYZ + f_{i,j,k} \end{aligned} \tag{2.25}$$

where, $X = x-x_i$, $Y = y-y_j$, $Z = z-z_k$, $C1 \sim C16$ are sixteen coefficients of cubic interpolation functions in three dimensions.

The physical quantity after the advection step $f^*_{i,j,k}$ and its spatial derivatives $f^*_{xi,j,k}$, $f^*_{yi,j,k}$, $f^*_{zi,j,k}$ are required to be continuous in order to determine the coefficient of $C1 \sim C16$. As a result, we obtain.

$$\begin{aligned} f^*_{i,j,k} = {} & [(C1_{i,j,k}\xi + C2_{i,j,k}\zeta + C3_{i,j,k}\eta + C4_{i,j,k})\xi + C5_{i,j,k}\zeta + f_{xi,j,k}]\xi \\ & +[(C6_{i,j,k}\zeta + C7_{i,j,k}\eta + C8_{i,j,k}\xi + C9_{i,j,k})\zeta + C10_{i,j,k}\eta + f_{yi,j,k}]\zeta \\ & +[(C11_{i,j,k}\eta + C12_{i,j,k}\xi + C13_{i,j,k}\zeta + C14_{i,j,k})\eta + C15_{i,j,k}\xi + f_{zi,j,k}]\eta \\ & +C16_{i,j,k}\xi\zeta\eta + f_{i,j,k} \end{aligned} \tag{2.26}$$

$$\begin{aligned} f^*_{xi,j,k} = {} & (3C1_{i,j,k}\xi + 2C2_{i,j,k}\zeta + 2C3_{i,j,k}\eta + 2C4_{i,j,k})\xi + C5_{i,j,k}\zeta + f_{xi,j,k} \\ & +C8_{i,j,k}\zeta^2 + C12_{i,j,k}\eta^2 + C15_{i,j,k}\eta + C16_{i,j,k}\zeta\eta \end{aligned} \tag{2.27}$$

$$\begin{aligned} f^*_{yi,j,k} = {} & (3C6_{i,j,k}\zeta + 2C7_{i,j,k}\eta + 2C8_{i,j,k}\xi + 2C9_{i,j,k})\zeta + C10_{i,j,k}\eta + f_{yi,j,k} \\ & +C13_{i,j,k}\eta^2 + C2_{i,j,k}\xi^2 + C5_{i,j,k}\xi + C16_{i,j,k}\xi\eta \end{aligned} \tag{2.28}$$

$$\begin{aligned} f^*_{zi,j,k} = {} & (3C11_{i,j,k}\eta + 2C12_{i,j,k}\xi + 2C13_{i,j,k}\zeta + 2C14_{i,j,k})\eta + C15_{i,j,k}\xi + f_{zi,j,k} \\ & +C3_{i,j,k}\xi^2 + C7_{i,j,k}\zeta^2 + C10_{i,j,k}\zeta + C16_{i,j,k}\xi\zeta \end{aligned} \tag{2.29}$$

where, $\xi = -u\Delta t$, $\zeta = -v\Delta t$, $\eta = -w\Delta t$.

2.4.3 The Type-M CIP Scheme

Although the type A-CIP scheme is a high-precision numerical scheme, the implementation of this scheme in multi dimensions requires a very complicated in programming. Further more, the type A-CIP scheme might cost high computational load. Therefore, the type-M CIP scheme proposed by Nakamura et al. (1999) with a high efficiency in solving multi dimensions is introduced in the present model. As shown in Fig.**2.5**, far from the type A-CIP scheme, in which three-dimensions is extended straight forwards from the one-dimensional case, the type M-CIP scheme uses the fractional step technique to extend one dimension to multi dimensions, and therefore a complicated implement for the codes can be avoided.

In this section, the factional step technique for extending one dimension to three dimensions and the differential equation for solving by the central difference method are introduced. For

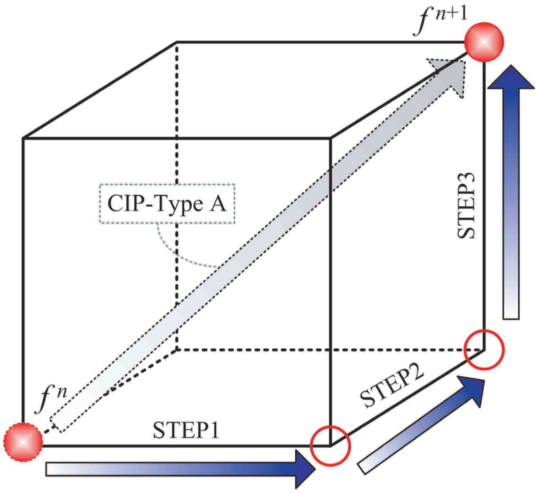

Figure **2.5** The concept of M-CIP scheme

simplicity, the equation for calculating the advection step Eq.(2.30) and equation for updating the spatial difference by central difference method Eq.(2.31) in one dimension are expressed,

$$CIP-\psi \quad \left(F^n, F^n_\psi \longrightarrow F^{n+1}, F^{n+1}_\psi\right) \tag{2.30}$$

$$CENTER-\chi \quad \left(F^n_\chi \longrightarrow F^{n+1}_\chi\right) \tag{2.31}$$

where, ψ, χ represent for x, y, z.

By the above expression, the above equations for type M-CIP scheme in three dimensions are extended into Eqs.(2.32)∼(2.40).

The updating procedure can be explained by STEP 2, for example. In this step, the value after advection in x direction is used for solving the advection equation in y direction equation. However, it must be noted that, F^1_y and F^1_z is not yet obtained after Eq.(2.32), but is obtained after Eqs.(2.33) and (2.34). To solve Eq.(2.33) and Eq.(2.34), the central difference method is proposed by Nakamura (1999) is used.

[STEP1]

$$CIP-X \quad \left(F^n, F^n_x \longrightarrow F^1, F^1_x\right) \tag{2.32}$$

$$CENTER-X \quad \left(F^n_y \longrightarrow F^1_y\right) \tag{2.33}$$

$$CENTER-X \quad \left(F^n_z \longrightarrow F^1_z\right) \tag{2.34}$$

[STEP2]

$$CIP-Y \;\left(F^1, F_y^1 \longrightarrow F^2, F_y^2\right) \tag{2.35}$$

$$CENTER-Y \;\left(F_x^1 \longrightarrow F_x^2\right) \tag{2.36}$$

$$CENTER-Y \;\left(F_z^1 \longrightarrow F_z^2\right) \tag{2.37}$$

[STEP3]

$$CIP-Z \;\left(F^2, F_z^2 \longrightarrow F^{n+1}, F_z^{n+1}\right) \tag{2.38}$$

$$CENTER-Z \;\left(F_x^2 \longrightarrow F_x^{n+1}\right) \tag{2.39}$$

$$CENTER-Z \;\left(F_y^2 \longrightarrow F_y^{n+1}\right) \tag{2.40}$$

Herein, the procedure for solving Eq.(2.33) is summarized. First, taking a derivation of the advection equation in x direction Eq.(2.41) in y direction. we obtained Eq.(2.42). Using the central difference method for Eq.(2.42), Eq.(2.43) is formed, in which the value of $\partial f/\partial x$, which is advanced of after advection in STEP1, $\partial f^1/\partial x$, is used for solving Eq.(2.43).

$$\frac{\partial f}{\partial t} + u\frac{\partial f}{\partial x} = 0 \tag{2.41}$$

$$\frac{\partial}{\partial t}\left(\frac{\partial f}{\partial y}\right) + \frac{\partial}{\partial y}\left(u\frac{\partial f}{\partial x}\right) = 0 \tag{2.42}$$

$$\frac{g_y^* - g_y^n}{\Delta t} + \frac{\left(u\dfrac{\partial f}{\partial x}\right)_{i,j+1} - \left(u\dfrac{\partial f}{\partial x}\right)_{i,j-1}}{\Delta y_j + 0.5\left(\Delta y_{j-1} + \Delta y_{j+1}\right)} = 0 \tag{2.43}$$

where, $g_y = \partial f/\partial y$.

2.4.4 Exactly Conservative Semi-Lagrangian Method CIP-CSL2

This section presents exactly conservative semi-Lagrangian Method CIP-CSL2 schemes for solving the equation of mass, introduced by Yabe et al. (2000) and Nakamura et al. (2000). These schemes are used in the model in order to enhance the accuracy of the computational results. Since the method based on the ”Constrained Interpolation Profile” scheme, which provides a more general concept than original CIP in involving a larger variety or a wider spectrum of the numerical technique to construct a semi-Lagrangian scheme but keeps the many good characteristics of the original CIP scheme, the authors adopt CIP as a phrase standing for ”Constrained Interpolation Profile”.

(1) One-dimensional CIP-CSL2 scheme

Herein, a method to solve the conservation of mass Eq.(2.44) is presented,

$$\frac{\partial f}{\partial t} + \frac{\partial (uf)}{\partial x} = 0. \tag{2.44}$$

Starting with the following advection equation,

$$\frac{\partial D}{\partial t} + u\frac{\partial D}{\partial x} = 0. \tag{2.45}$$

Taking a spatial derivative of Eq.(2.45) and defining $D' = \int D dx$, a conservative-type equation Eq.(2.46) is obtained,

$$\frac{\partial D'}{\partial t} + \frac{\partial (uD')}{\partial x} = 0. \tag{2.46}$$

Because Eq.(2.46) is the same as Eq.(2.44), the idea of using $D' = f$ in Eq.(2.46) and $D = \int f dx$ in Eq.(2.45) is suggested. On the other hand, the Eq.(2.45) is exactly an advection form, therefore the CIP procedure can be applied. However, the original CIP scheme given in the previous section uses the value of f and its first-order spatial derivative $\partial f/\partial x$ at the computational grid points to construct a profile inside the grid cell, herein the value of f and its integral function, $D = \int f dx$ are used.

By this analogy, a function of D_i is presented in Eq.(2.47), and an approximation of its profile by a cubic polynomial is shown in Eq.(2.48),

$$D_i\left(x\right) = \int_{x_i}^{x} f\left(\alpha\right) d\alpha, \tag{2.47}$$

$$D_i\left(x\right) = A1_i X^3 + A2_i X^2 + f_i^n X, \tag{2.48}$$

where,

$$f\left(x\right) = \frac{\partial D_i\left(x\right)}{\partial x} = 3A1_i X^2 + 2A2_i X + f_i^n. \tag{2.49}$$

From the definition of D in Eq.(2.47), it is clear that,

$$D_i\left(x_i\right) = 0 \tag{2.50}$$

$$D_i\left(x_{im1}\right) = -\mathrm{sign}\left(u\right)\rho^n_{\mathrm{icell}} \tag{2.51}$$

where, ρ^n_{icell} is the total mass of upwind cell defined at the cell center $i \pm 1/2, im1 = i - \mathrm{sign}\left(u\right)$ and $\mathrm{icell} = i - \mathrm{sign}\left(u\right)/2$.

It is also noted that $\partial D/\partial x = f$, therefore Eq.(2.52) and Eq.(2.53) are also obtained,

$$\frac{\partial D_i\left(x_i\right)}{\partial x} = f_i^n, \tag{2.52}$$

$$\frac{\partial D_i\left(x_{im1}\right)}{\partial x} = f_{im1}^n, \tag{2.53}$$

Therefore, the coefficient $A1_i$ and $A2_i$ are determined in order to satisfy the constraints of Eqs.(2.50)∼(2.53) as follows,

$$A1_i = \frac{f_i^n + f_{im1}^n}{\Delta x^2} + \frac{2\mathrm{sign}(u)\rho_{icell}^n}{\Delta x^3}, \tag{2.54}$$

$$A2_i = -\frac{2 f_i^n + f_{im1}^n}{\Delta x} - \frac{3\mathrm{sign}(u)\rho_{icell}^n}{\Delta x^2}, \tag{2.55}$$

where, $\Delta x = x_{im1} - x_i$. Based on the values of $A1_i$,$A2_i$, the value of f after the advection phase f_i^* is obtained,

$$f_i^* = \frac{\partial D_i\left(x_i + \xi\right)}{\partial x} = 3A1_i\xi^2 + 2A2_i\xi + f^n \tag{2.56}$$

where, ξ is the coefficient defined by the remapping procedure, which is explained in Nakamura et al. (2000).

Now turn back to the time evolution of f, which is calculated in the same way as the original scheme. The conservation of mass Eq.(2.44) is split into two steps:

[Advection step]

$$\frac{\partial f}{\partial t} + u\frac{\partial f}{\partial x} = 0, \tag{2.57}$$

[Non-advection step]

$$\frac{\partial f}{\partial t} = -f\frac{\partial u}{\partial x}. \tag{2.58}$$

After the advection phase is solved, the non-advection phase is calculated with the results of the advection phase by using the finite difference method as follows:

$$f_i^{n+1} = f_i^* - f_i^*\frac{u_{i+1/2} - u_{i-1/2}}{\Delta x_i}\Delta t \tag{2.59}$$

where, f_i^* is the the value of f after the advection phase, as shown in Eq.(2.56).

(2) The Type 3M-CIP-CSL2

The CIP-CSL2 scheme is a high-accuracy numerical scheme. However, the supplementation of the constrained conditions makes the extension to three dimensions complex, and further heavy computational load. Therefore, the fractional step technique is used to extend this scheme to three-dimensional case. By using the fractional step technique, the implementation for extension is programmed easily.

First, using the fractional step technique for extending the conservation of mass Eq.(2.60) in three direction x, y, z, Eqs.(2.61)～(2.63) are obtained. The CIP-CSL2 scheme for one dimension is then applied.

$$\frac{\partial f}{\partial t} + \frac{\partial (uf)}{\partial x} + \frac{\partial (vf)}{\partial y} + \frac{\partial (wf)}{\partial z} = 0 \tag{2.60}$$

$$\frac{\partial f}{\partial t} + \frac{(uf)}{\partial x} = 0 \tag{2.61}$$

$$\frac{\partial f}{\partial t} + \frac{(vf)}{\partial y} = 0 \tag{2.62}$$

$$\frac{\partial f}{\partial t} + \frac{(wf)}{\partial z} = 0 \tag{2.63}$$

The CIP-CSL2 algorithm in one dimension is introduced in Eq.(2.64).

$$CIPCSL1d\left(u, f^n \to f^{n+1}, \rho^n \to \rho^{n+1}, x\right) \tag{2.64}$$

where, f is an advection function, ρ is cell-integrated quantity.

Make a use of the type 3M-CIP for Eqs.(2.61)～(2.63), Eq.(2.60) is solved by the procedure shown in Eqs.(2.65)～(2.76).

[Step1:x-direction]

$$CIPCSL1d\left(u, f^n \to f^{step1}, \sigma_x^n \to \sigma_x^{n+1}, x\right) \tag{2.65}$$

$$CIPCSL1d\left(u, \sigma_y^n \to \sigma_y^{step1}, S_{xy}^n \to S_{xy}^{step1}, x\right) \tag{2.66}$$

$$CIPCSL1d\left(u, \sigma_z^n \to \sigma_z^{step1}, S_{zx}^n \to S_{zx}^{step1}, x\right) \tag{2.67}$$

$$CIPCSL1d\left(u, S_{yz}^n \to S_{yz}^{n+1}, \rho^n \to \rho^{step1}, x\right) \tag{2.68}$$

[Step2:y-direction]

$$CIPCSL1d\left(v, f^{step1} \to f^{step2}, \sigma_y^{step1} \to \sigma_y^{step2}, y\right) \tag{2.69}$$

$$CIPCSL1d\left(v, \sigma_x^{step1} \to \sigma_x^{step2}, S_{xy}^{step1} \to S_{xy}^{step2}, y\right) \tag{2.70}$$

$$CIPCSL1d\left(v, \sigma_z^{step1} \to \sigma_z^{step2}, S_{yz}^{step1} \to S_{yz}^{step2}, y\right) \tag{2.71}$$

$$CIPCSL1d\left(v, S_{zx}^{step1} \to S_{zx}^{step2}, \rho^{step1} \to \rho^{step2}, y\right) \tag{2.72}$$

[Step3:z-direction]

$$CIPCSL1d\left(w, f^{step2} \to f^{n+1}, \sigma_z^{step2} \to \sigma_z^{n+1}, z\right) \tag{2.73}$$

$$CIPCSL1d\left(w, \sigma_x^{step2} \to \sigma_x^{n+1}, S_{zx}^{step2} \to S_{zx}^{n+1}, z\right) \tag{2.74}$$

$$CIPCSL1d\left(w, \sigma_y^{step2} \to \sigma_y^{n+1}, S_{yz}^{step2} \to S_{yz}^{n+1}, z\right) \tag{2.75}$$

$$CIPCSL1d\left(w, S_{xy}^{step2} \to S_{xy}^{n+1}, \rho^{step2} \to \rho^{n+1}, z\right) \tag{2.76}$$

where, σ and S represent the line density and surface density, respectively. The locations of all variables are shown in Fig.**2.6**. The determination of line density and surface density cell-integrated mass is found in Eqs.(2.77)～(2.83).

$$\sigma_{x,i-1/2,j,k} = \int_{x_i}^{x_{i-1}} f\left(x, y_j, z_k\right) dx \tag{2.77}$$

$$\sigma_{y,i,j-1/2,k} = \int_{y_j}^{y_{j-1}} f\left(x_i, y, z_k\right) dy \tag{2.78}$$

$$\sigma_{z,i,j,k-1/2} = \int_{z_k}^{z_{k-1}} f\left(x_i, y_j, z\right) dz \tag{2.79}$$

$$S_{xy,i-1/2,j-1/2,k} = \int_{x_i}^{x_{i-1}} \int_{y_j}^{y_{j-1}} f\left(x, y, z_k\right) dxdy \tag{2.80}$$

$$S_{yz,i,j-1/2,k-1/2} = \int_{y_j}^{y_{j-1}} \int_{z_k}^{z_{k-1}} f\left(x_i, y, z\right) dydz \tag{2.81}$$

$$S_{zx,i-1/2,j,k-1/2} = \int_{z_k}^{z_{k-1}} \int_{x_i}^{x_{i-1}} f\left(x, y_j, z\right) dzdx \tag{2.82}$$

$$\rho_{i-1/2,j-1/2,k-1/2} = \int_{z_k}^{z_{k-1}} \int_{y_j}^{y_{j-1}} \int_{x_i}^{x_{i-1}} f\left(x, y, z\right) dxdydz \tag{2.83}$$

As mentioned in M-CIP procedure, to solve Eq.(2.69) in STEP2, σ_y^{step1} must be advected by Eq.(2.66).

Herein, the procedure for solving σ_y^{step1} is described. Taking a intergation of Eq.(2.61) in y direction, Eq.(2.84) is obtained. And then, use of the definition of the line density in Eq.(2.84), the advection equation of the line density σ_y is formed in Eq.(2.85).

$$\int_{y_j}^{y_{j+1}} \left\{\frac{\partial f}{\partial t} + \frac{\partial (uf)}{\partial x}\right\} dy = 0 \tag{2.84}$$

$$\frac{\partial \sigma_y}{\partial t} + \frac{\partial\left(u\sigma_y\right)}{\partial x} = 0 \tag{2.85}$$

In Eq.(2.85), σ_y is advected by using the surface density S_{xy}. Time evolution of S_{xy} is

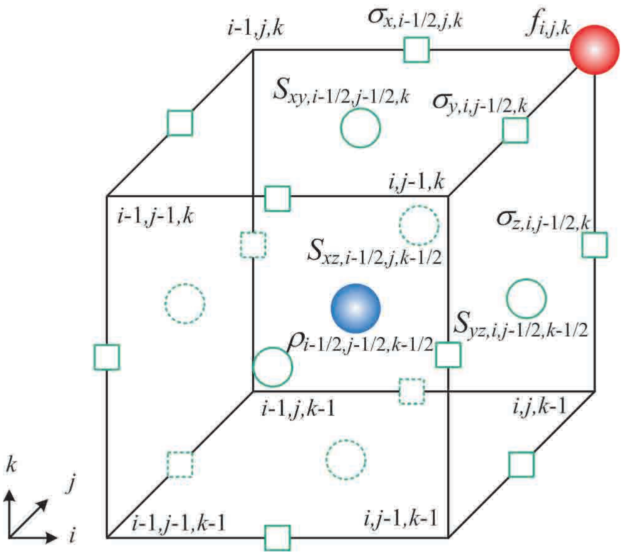

Figure **2.6** The locations of the variable in 3M-CIP-CSL2 scheme

calculated using Eq.(2.86) and Eq.(2.87).

$$S^{step1}_{xy,i+1/2,j+1/2,k} = S^{n}_{xy,i+1/2,j+1/2,k} + \Delta S_{xy,i+1,j+1/2,k} - \Delta S_{xy,i,j+1/2,k} \tag{2.86}$$

$$\Delta S_{xy,i,j+1/2,k} = \int_{x_i}^{x_{i+\xi}} \sigma_{y,i,j+1/2,k} dx \tag{2.87}$$

Next, the procedure for solving Eq.(2.68) is explained. Taking a integration of the advection equation of f in y, z direction, as shown in Eq.(2.88), and then making a use of surface density of S_{yz}, it leads to the advection equation of S_{yz}, Eq.(2.89),

$$\int_{z_i}^{z_{i+1}} \int_{y_j}^{y_{j+1}} \left\{ \frac{\partial f}{\partial t} + \frac{\partial (uf)}{\partial x} \right\} dydz = 0 \tag{2.88}$$

$$\frac{\partial S_{yz}}{\partial t} + \frac{\partial \left(uS_{yz} \right)}{\partial x} = 0 \tag{2.89}$$

Finally, the cell-integrated mass after STEP1 is advected by using S_{yz} obtained from Eq.(2.89), as shown in Eq.(2.90) and Eq.(2.91).

$$\rho^{step1}_{i,j,k} = \rho^{n}_{i,j,k} + \Delta\rho_{i+1,j,k} - \Delta\rho_{i,j,k} \tag{2.90}$$

$$\Delta\rho_{i,j,k} = \int_{x_i}^{x_i+\xi} S_{yz}(x)\, dx \tag{2.91}$$

where, $\xi = -u_{i,j,k}\Delta t$.

By applying the above-mentioned procedure, Eqs.(2.65)～(2.76) are solved. Consequently, the conservation of mass in three dimensions is completely calculated.

2.5 Numerical Solutions at the non-Advection Step

2.5.1 SMAC Scheme

As the above-mentioned, the values of physical quantities after the advection step are used to calculate the non-advection step. However, Eq.(2.9) and Eq.(2.10) at the non-advection step cannot be solved explicitly since the unknown variables at the next time step are included in both the left and the right sides of the equations. Therefore, the extended SMAC method is used in this model to compute for both compressible and incompressible fluids.

First, a predicted velocity $\tilde{u}_i$ is computed with the help of variables after the advection step u_i^*, p^*, as shown in Eq.(2.92). Moreover, the third-order Adams-Bashforth method is applied for calculating the external force term after the advection step in order to achieve the high accuracy for calculation results.

$$\frac{\tilde{u}_i - u_i^*}{\Delta t} = -\frac{1}{\rho^n}\frac{\partial p^*}{\partial x_i} - g_i + \frac{23}{12}A_i^* + \frac{4}{3}A_i^n + \frac{5}{12}A_i^{*-1} \tag{2.92}$$

$$A_i^* = \frac{f_{si}^*}{\rho^n} + \frac{\partial}{\partial x_j}\left(-\tau_{ij}^* + 2\frac{\mu}{\rho^n}S_{ij}^*\right) - D_i u_i^* \tag{2.93}$$

$$A_i^n = \frac{f_{si}^n}{\rho^n} + \frac{\partial}{\partial x_j}\left(-\tau_{ij}^n + 2\frac{\mu}{\rho^n}S_{ij}^n\right) - D_i u_i^n \tag{2.94}$$

$$A_i^{*-1} = \frac{f_{si}^{*-1}}{\rho^{n-1}} + \frac{\partial}{\partial x_j}\left(-\tau_{ij}^{*-1} + 2\frac{\mu}{\rho^{n-1}}S_{ij}^{*-1}\right) - D_i u_i^{*-1} \tag{2.95}$$

where, superscript $*$ represents for the time step after advection; superscript n represents for the current time step, and superscript $* - 1$ represents for the previous time step.

Next, take a divergence of Eq.(2.9) and substituting Eq.(2.92) in the left side of the resultant equation, Eq.(2.96) is obtained,

$$\frac{u_i^{n+1} - \tilde{u}_i}{\Delta t} = -\frac{1}{\rho^n}\frac{\partial}{\partial x_i}\delta p \tag{2.96}$$

where, $\delta p = p^{n+1} - p^*$.

The Poission equations for the pressure correction $\partial u_j^{n+1}/\partial x_j$, which is shown in Eq.(2.97), is derived by taking the divergence of Eq.(2.10) and substituting $\partial u_j^{n+1}/\partial x_j$ using Eq.(2.96)

$$\frac{\partial}{\partial x_j}\cdot\left(\frac{1}{\rho^n}\frac{\partial}{\partial x_i}\delta p\right) = \frac{1}{\rho^n C_{ls}^2 \Delta t^2}\delta p + \frac{1}{\Delta t}\frac{\partial \tilde{u}_j}{\partial x_j} - \frac{1}{\Delta t}q \tag{2.97}$$

It is shown in Eq.(2.97) that the first term of the right-hand side contains the local sound speed in the denominator, therefore this term is automatically ignored in comparison with other term in the case of C_{ls} is large, which mean the fluid is compressible. This is the same procedure as a SMAC method for the incompressible fluid. Consequently, the computational algorithm proposed is considered as a SMAC method extended to compressible fluid (Kawasaki, 2005a). Interestingly, a unique algorithm can be used for both compressible and incompressible fluid. In this model, the Poisson equation is solved by an ILUCGS (Incomplete LU decomposition Conjugate Gradient Squared method).

Then, the variables at the next time step, u_i^{n+1} and p^{n+1} are updated by Eq.(2.98) and Eq.(2.99).

$$u_i^{n+1} = \tilde{u}_i - \frac{\Delta t}{\rho^n}\frac{\partial}{\partial x_i}\delta p \tag{2.98}$$

$$p^{n+1} = p^* + \delta p \tag{2.99}$$

On the other hand, the conservation of mass Eq.(2.11) is solved by splitting technique. First, Eq.(2.100) is calculated by the 3M-CIP-CSL2. The value of density obtained from Eq.(2.100) is then used to update the density at the next time step ρ^{n+1}, as shown in Eq.(2.101)

$$\frac{\rho^* - \rho^n}{\Delta t} + \frac{\partial\left(u_j^{n+1}\rho^n\right)}{\partial x_j} = 0 \tag{2.100}$$

$$\rho^{n+1} = \rho^* + \rho^* q \Delta t \tag{2.101}$$

Finally, the first spatial derivatives of physical quantity f in three direction f_x, f_y, f_z are updated by Eqs.(2.102)∼(2.104).

$$f_{xi,j,k}^{n+1} = f_{xi,j,k}^{*} + \frac{2\left(f_{i+1,j,k}^{n+1} - f_{i-1,j,k}^{n+1} - f_{i+1,j,k}^{*} + f_{i-1,j,k}^{*}\right)}{\Delta x_{i+1} + 2\Delta x_i + \Delta x_{i-1}} \tag{2.102}$$

$$f_{yi,j,k}^{n+1} = f_{yi,j,k}^{*} + \frac{2\left(f_{i,j+1,k}^{n+1} - f_{i,j-1,k}^{n+1} - f_{i,j+1,k}^{*} + f_{i,j-1,k}^{*}\right)}{\Delta y_{j+1} + 2\Delta y_j + \Delta y_{j-1}} \tag{2.103}$$

$$f_{zi,j,k}^{n+1} = f_{zi,j,k}^{*} + \frac{2\left(f_{i,j,k+1}^{n+1} - f_{i,j,k-1}^{n+1} - f_{i,j,k+1}^{*} + f_{i,j,k-1}^{*}\right)}{\Delta z_{k+1} + 2\Delta z_k + \Delta z_{k-1}} \tag{2.104}$$

2.5.2 Iterative Method for Solving Poisson Equation

The pressure correction δp in the Poisson equation Eq.(2.97) is discretized as follows,

$$\begin{aligned} &AKM_{i,j,k}\cdot\delta p_{i,j,k-1} + AJM_{i,j,k}\cdot\delta p_{i,j-1,k} + AIM_{i,j,k}\cdot\delta p_{i-1,j,k} + AD_{i,j,k}\cdot\delta p_{i,j,k} \\ &+AIP_{i,j,k}\cdot\delta p_{i+1,j,k} + AJP_{i,j,k}\cdot\delta p_{i,j+1,k} + AKP_{i,j,k}\cdot\delta p_{i,j,k+1} = B_{i,j,k} \end{aligned} \tag{2.105}$$

where, the coefficients of Eq.(2.105) are determined based on the values of densities after the advection step, whereas $B_{i,j,k}$ contains the wave source terrm $q/\Delta t$ and the predicted velocity

$\tilde{u}_{i,j,k}$

$$AKM_{i,j,k} = \frac{2}{\rho^*_{i,j,k}\Delta z_{k-1} + \rho^*_{i,j,k-1}\Delta z_k} \cdot \frac{1}{\Delta z_k} \tag{2.106}$$

$$AJM_{i,j,k} = \frac{2}{\rho^*_{i,j,k}\Delta y_{j-1} + \rho^*_{i,j-1,k}\Delta y_j} \cdot \frac{1}{\Delta y_j} \tag{2.107}$$

$$AIM_{i,j,k} = \frac{2}{\rho^*_{i,j,k}\Delta x_{i-1} + \rho^*_{i-1,j,k}\Delta x_i} \cdot \frac{1}{\Delta x_i} \tag{2.108}$$

$$\begin{aligned} AD_{i,j,k} = & -\left(\frac{2}{\rho^*_{i,j,k}\Delta x_{i-1} + \rho^*_{i-1,j,k}\Delta x_i} + \frac{2}{\rho^*_{i+1,j,k}\Delta x_i + \rho^*_{i,j,k}\Delta x_{i+1}} \right) \cdot \frac{1}{\Delta x_i} \\ & -\left(\frac{2}{\rho^*_{i,j,k}\Delta y_{j-1} + \rho^*_{i,j-1,k}\Delta y_j} + \frac{2}{\rho^*_{i,j+1,k}\Delta y_j + \rho^*_{i,j,k}\Delta y_{j+1}} \right) \cdot \frac{1}{\Delta y_j} \\ & -\left(\frac{2}{\rho^*_{i,j,k}\Delta z_{k-1} + \rho^*_{i,j,k-1}\Delta z_k} + \frac{2}{\rho^*_{i,j,k+1}\Delta z_k + \rho^*_{i,j,k}\Delta z_{k+1}} \right) \cdot \frac{1}{\Delta z_k} \\ & -\frac{1}{\rho^*_{i,j,k} C^2_{si,j,k} \Delta t} \end{aligned} \tag{2.109}$$

$$AIP_{i,j,k} = \frac{2}{\rho^*_{i+1,j,k}\Delta x_i + \rho^*_{i,j,k}\Delta x_{i+1}} \cdot \frac{1}{\Delta x_i} \tag{2.110}$$

$$AJP_{i,j,k} = \frac{2}{\rho^*_{i,j+1,k}\Delta y_j + \rho^*_{i,j,k}\Delta y_{j+1}} \cdot \frac{1}{\Delta y_j} \tag{2.111}$$

$$AKP_{i,j,k} = \frac{2}{\rho^*_{i,j,k+1}\Delta z_k + \rho^*_{i,j,k}\Delta z_{k+1}} \cdot \frac{1}{\Delta z_k} \tag{2.112}$$

$$B_{i,j,k} = \frac{1}{\Delta t}\left(\frac{\tilde{u}_{i,j,k} - \tilde{u}_{i-1,j,k}}{\Delta x_i} + \frac{\tilde{v}_{i,j,k} - \tilde{v}_{i,j-1,k}}{\Delta y_j} + \frac{\tilde{w}_{i,j,k} - \tilde{w}_{i,j,k-1}}{\Delta z_k} \right) - \frac{q}{\Delta t} \tag{2.113}$$

2.5.3 Surface Tension Model

A CSF tension model developed by Brackbill et al.(1992) is introduced in the Navier-Stokes equations to evaluate effect of surface tension between gas and liquid phase. The CSF model assumes that the interface between gas and liquid phase, the thickness of which is in fact 0 has some transition ranges, as shown in Fig.**2.7**. The surface tension f_{is} is formed as Eq.(2.114).

$$f_{is} = \sigma\kappa \frac{\nabla\phi_2}{[\phi_2]} \frac{\phi_2}{< \phi_2 >} \tag{2.114}$$

where, σ is the coefficient of the surface tension, κ is the curvature, $[\phi_2] = 1, \; < \phi_2 >= 1/2$. The curvature κ is calculated by Eq.(2.115), in which $\boldsymbol{n}$ is the unit normal vector to the surface.

$$\kappa = -(\nabla \cdot \hat{\boldsymbol{n}}) \tag{2.115}$$

In principle, the curvature κ can be directly calculated based on ϕ_2. However, it might be difficult to obtain the curvature κ by this way because the values of ϕ_2 at the interface changes rapidly. In order to obtain proper values of the curvature, a smoothing equation for ϕ_2 at the interface is used as follows,

$$
\begin{aligned}
\phi_{2_{i,j,k}} =& \frac{1}{2}\phi_{2_{i,j,k}} + \frac{1}{2}\frac{1}{1+6C_1+12C_2+8C_3}\Big[\phi_{2_{i,j,k}} + C_1(\phi_{2_{i-1,j,k}} + \phi_{2_{i+1,j,k}} + \phi_{2_{i,j-1,k}} + \phi_{2_{i,j+1,k}} \\
&+\phi_{2_{i,j,k-1}} + \phi_{2_{i,j,k+1}}) + C_2(\phi_{2_{i-1,j-1,k}} + \phi_{2_{i-1,j+1,k}} + \phi_{2_{i+1,j-1,k}} + \phi_{2_{i+1,j+1,k}} + \phi_{2_{i-1,j,k-1}} \\
&+\phi_{2_{i-1,j,k+1}} + \phi_{2_{i+1,j,k-1}} + \phi_{2_{i+1,j,k+1}} + \phi_{2_{i,j-1,k-1}} + \phi_{2_{i,j-1,k+1}} + \phi_{2_{i,j+1,k-1}} + \phi_{2_{i,j+1,k+1}}) \\
&+C_3(\phi_{2_{i-1,j-1,k-1}} + \phi_{2_{i-1,j-1,k+1}} + \phi_{2_{i-1,j+1,k-1}} + \phi_{2_{i-1,j+1,k+1}} + \phi_{2_{i+1,j-1,k-1}} + \phi_{2_{i+1,j-1,k+1}} \\
&+\phi_{2_{i+1,j+1,k-1}} + \phi_{2_{i+1,j+1,k+1}})\Big]
\end{aligned}
\tag{2.116}
$$

where, $C_1 = 1/\left(6 + 12/\sqrt{2} + 8/\sqrt{3}\right)$, $C_2 = C_1/\sqrt{2}$, $C_3 = C_1/\sqrt{3}$.

It is noted that the smoothed values of ϕ_2 are used only for determining the curvature. For other calculations, non-smoothed values of ϕ_2 are used as normal.

2.5.4 Turbulence Model

The turbulence formed by a complex interaction between different scale vorties is always observed in the real flows. For the analysis of such turbulence flows, in the large eddy simulation (LES), only the large-scale field greater than the grid-scale (GS) is directly resolved while the effect of the unresolved small-scale field named the subgrid-scale (SGS) is modeled. In early LES calculations, the SGS was modeled by pioneering Smagorinsky model (Smagorinky, 1963), dynamic Smagorinsky model (DSM; Germano et al., 1991), dynamic mixed model (DMM; Zang et al., 1993). These models, however, have shown the lack of accounting for backscatter of energy from small scales to large scales. In this study, the DTM (Dynamic Two-parameter Model) model proposed by Salvetti and Banerjee (1995) is used for calculating SGS.

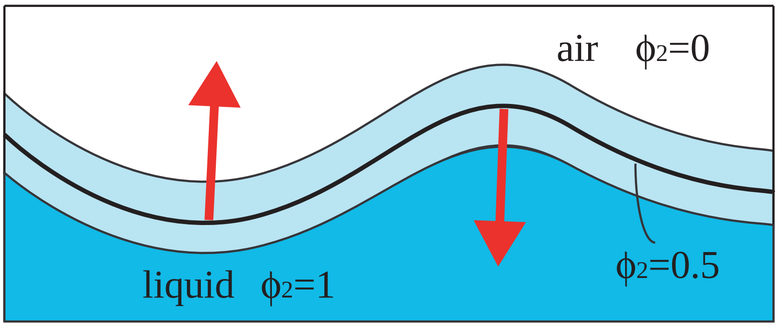

Figure **2.7** The concept of the CSF model

In the DTM, SGS stress term τ_{ij} is devided into three components as shown in Eq.(2.117)

$$\tau_{ij} = L_{ij}^{m} + C_{ij}^{m} + R_{ij}^{m} \tag{2.117}$$

where, L_{ij}^{m} is the modified Leonard tensor, C_{ij}^{m} is the modified cross tensor, R_{ij}^{m} is the modified SGS Reynold tensor. Each tensor is separately Galilean invariance.

L_{ij}^{m}, C_{ij}^{m} expressed in Eq.(2.117) are formed by two components, which are the GS (Grid Scale) component and the SGS component. In the DTM, the relation between L_{ij}^{m} to C_{ij}^{m} is assumed. Therefore, only C_{ij}^{m} needs to be evaluated. For the determination of the modified SGS Reynold tensor R_{ij}^{m} only the second component is neglected. By using grid filter and test filter, the SGS tensor τ_{ij}^{a} and T_{ij}^{a} are obtained as follows,

$$\tau_{ij}^{a} = L_{ij}^{ma} - C_s \overline{\Delta}^{2} |\overline{S}| \overline{S}_{ij} \tag{2.118}$$

$$T_{ij}^{a} = L_{ij}^{Ta} - C_s \tilde{\overline{\Delta}}^{2} |\tilde{\overline{S}}| \tilde{\overline{S}}_{ij} \tag{2.119}$$

$$L_{ij}^{m} = \overline{\overline{u}_i \overline{u}_j} - \overline{\overline{u}}_i \overline{\overline{u}}_j \tag{2.120}$$

$$L_{ij}^{T} = \widetilde{\overline{\overline{u}_i \overline{u}_j}} - \tilde{\overline{\overline{u}}}_i \tilde{\overline{\overline{u}}}_j \tag{2.121}$$

where, over bar represents grid filter, $\tilde{}$ represents test filter, τ_{ij}^{a} is denoted by $\tau_{ij}^{a} = \tau_{ij} - \delta_{ij}\tau_{kk}/3$.

In the DTM, the SGS tensor τ_{ij}^{a} is calculated by Eq.(2.122),

$$\tau_{ij}^{a} = C_L L_{ij}^{ma} - C_s \left|\overline{S}\right| \overline{S}_{ij} \tag{2.122}$$

where, model coefficient C_L and C_s are determined by,

$$C_L = \frac{\langle \mathcal{L}_{ij}^{a} \mathcal{H}_{ij}^{a} \rangle \langle \mathcal{M}_{ij} \mathcal{M}_{ij} \rangle - \langle \mathcal{L}_{ij}^{a} \mathcal{M}_{ij} \rangle \langle \mathcal{H}_{ij}^{a} \mathcal{M}_{ij} \rangle}{\langle \mathcal{H}_{ij}^{a} \mathcal{H}_{ij}^{a} \rangle \langle \mathcal{M}_{ij} \mathcal{M}_{ij} \rangle - \langle \mathcal{H}_{ij}^{a} \mathcal{M}_{ij} \rangle \langle \mathcal{H}_{ij}^{a} \mathcal{M}_{ij} \rangle} \tag{2.123}$$

$$C_s = \frac{\langle \mathcal{L}_{ij}^{a} \mathcal{M}_{ij} \rangle \langle \mathcal{H}_{ij}^{a} \mathcal{H}_{ij}^{a} \rangle - \langle \mathcal{L}_{ij}^{a} \mathcal{H}_{ij}^{a} \rangle \langle \mathcal{H}_{ij}^{a} \mathcal{M}_{ij} \rangle}{\langle \mathcal{H}_{ij}^{a} \mathcal{H}_{ij}^{a} \rangle \langle \mathcal{M}_{ij} \mathcal{M}_{ij} \rangle - \langle \mathcal{H}_{ij}^{a} \mathcal{M}_{ij} \rangle \langle \mathcal{H}_{ij}^{a} \mathcal{M}_{ij} \rangle} \tag{2.124}$$

$$\mathcal{L}_{ij} = \widetilde{\overline{u}_i \overline{u}_j} - \tilde{\overline{u}}_i \tilde{\overline{u}}_j \tag{2.125}$$

$$\mathcal{M}_{ij} = \alpha^{2} |\tilde{\overline{S}}| \tilde{\overline{S}}_{ij} - \widetilde{|\overline{S}| \overline{S}_{ij}} \tag{2.126}$$

$$\mathcal{H}_{ij} = \widetilde{\overline{\overline{u}}_i \overline{\overline{u}}_j} - \tilde{\overline{\overline{u}}}_i \tilde{\overline{\overline{u}}}_j \tag{2.127}$$

where, α is the ratio between the width of test and grid filters ($\tilde{\overline{\Delta}}/\overline{\Delta}$).

Unlike the Smagorinsky model using a simple turbulence model, the DTM model computes dynamically 2 model coefficients by using the GS (Grid Scale) component. Consequently, the transportation of the energy from SGS to GS is considered and the DTM takes the advantage in keeping small fluctuation of model coefficients as well as maintaining the local stability. Therefore, the DTM can be well calculate the turbulence flow with complex changes.

2.6 Dynamic Motion Analysis of Multiple Rigid Bodies

The motions of rigid bodies are solved similarly to the numerical procedure proposed by Xiao et al. (1997). The assumption is that rigid bodies are a high viscous fluid, the entire computational domain including the region of rigid bodies is calculated by the above-mentioned computational algorithm. However, the distortion of the rigid bodies occurs because they are treated as a fluid. In order to overcome this problem, the translation velocity and angular velocity at the center of mass of the rigid bodies are computed first. Then, the positions of each body at the next time step are calculated by applying the computed velocities, which is the sum of the translational and angular velocities only to cells in the solid phase. This also indicates that the motions of rigid bodies are simulated without setting any boundary conditions between solid and other phases. It should be noted that the total of density functions of solid phase in a computational cell is less than 1. In this section, the motion analysis for a rigid body is explained in detail.

2.6.1 Translational Motion Analysis of a Rigid Body

The position of the center of mass $\overline{\boldsymbol{x}_l}$ of a rigid body is calculated as

$$\overline{\boldsymbol{x}_l} = \frac{1}{M_l} \int\int\int_S \boldsymbol{x} \phi_{1l}\left(x, y, z\right) \rho_{sl} ds \tag{2.128}$$

where, l represents the order number of the rigid body, ρ_{sl} is the density of the rigid body order l, S denotes the computational domain, $\boldsymbol{x}$ is position vector, and M_l is the total amount of mass of the rigid body order l, which denotes as Eq.(2.129),

$$M_l = \int\int\int_S \phi_{1l}\left(x, y, z\right) \rho_{sl} ds = \sum_{i,j,k} \left(\phi_{1l}\right)_{i,j,k} \rho_{sl} \Delta x_i \Delta y_j \Delta z_k \tag{2.129}$$

Next, the velocity of the center of mass $\overline{\boldsymbol{u}_l}$, and the acceleration of the center of mass $d\overline{\boldsymbol{u}_l}/dt$ are calculated by Eq.(2.130) and Eq.(2.131),

$$\overline{\boldsymbol{u}_l} = \frac{d\overline{\boldsymbol{x}_l}}{dt} = \frac{1}{M_l} \int\int\int_S \frac{d\boldsymbol{x}}{dt} \phi_{1l} \rho_{sl} ds \tag{2.130}$$

$$\frac{d\overline{\boldsymbol{u}_l}}{dt} = \frac{1}{M_l} \int\int\int_S \frac{d\boldsymbol{u}}{dt} \phi_{1l} \rho_{sl} ds = \frac{1}{M_l} \sum_{i,j,k} \left(\frac{d\boldsymbol{u}}{dt}\right)_{i,j,k} \left(\phi_{1l}\right)_{i,j,k} \rho_{sl} \Delta x_i \Delta y_j \Delta z_k \tag{2.131}$$

Using the pressure solved at all cells, $d\boldsymbol{u}/dt$ is calculated by

$$\left(\frac{d\boldsymbol{u}}{dt}\right)_{i,j,k} = -\frac{1}{\rho_{i,j,k}} \left(\frac{\partial p}{\partial x}\right)_{i,j,k} + \boldsymbol{g} \tag{2.132}$$

where, $\boldsymbol{g} = (0, 0, -g)$ is gravity acceleration vector.

Then, the translation motion of the center of mass of the rigid body l order at the next time step can be calculated by Eq.(2.133),

$$\overline{\boldsymbol{u}_l}^{n+1} = \overline{\boldsymbol{u}_l}^{n} + \frac{d\overline{\boldsymbol{u}_l}}{dt}\Delta t \tag{2.133}$$

2.6.2 Rotational Motion Analysis of a Rigid Body

In this model, the rotational motion of a rigid body is calculated by a quaternion vector. Herein, after the quaternion calculation is summarized, the rotational motion calculation is presented.

(1) Quaternion

Quaternion concept was introduced by William Rowan Hamilton in 1843 as a four-dimensional extension to complex number. It has been proven that quaternions can analyze three dimensional rotation accurately, as depicted as in Fig.**2.8**. Baraff (1997) presented a quaternion formed by a four dimensional vector $\boldsymbol{q}$, as shown in Eq.(2.134),

$$\boldsymbol{q} = \left(s, q_x, q_y, q_z\right) \tag{2.134}$$

The components of vector $\boldsymbol{q}$ is expressed by a rotational vector $\boldsymbol{v}$ and a rotational angle θ around $\boldsymbol{v}$, as shown in Eq.(2.135),

$$\boldsymbol{q} = \left(\cos\left(\frac{\theta}{2}\right), v_x \sin\left(\frac{\theta}{2}\right), v_y \sin\left(\frac{\theta}{2}\right), v_z \sin\left(\frac{\theta}{2}\right)\right) \tag{2.135}$$

It is noted that in Eq.(2.135), the quaternion is unit vector.

Then, the quaternion rotation matrix $\boldsymbol{R}$ is expressed as follows,

$$\boldsymbol{R} = \begin{bmatrix} 1 - 2q_y^2 - 2q_z^2 & 2q_xq_y - 2sq_z & 2q_xq_z + 2sq_y \\ 2q_xq_y + 2sq_z & 1 - 2q_x^2 - 2q_z^2 & 2q_yq_z - 2sq_x \\ 2q_xq_z - 2sq_y & 2q_yq_z + 2sq_x & 1 - 2q_x^2 - 2q_y^2 \end{bmatrix} \tag{2.136}$$

In the model, the quaternion rotation matrix is used to calculated the three dimensional rotation of rigid body.

(2) Rotational Motion Calculation

The rotation motion of a rigid body around its rotational axis is defined as in Eq.(2.137). Then, using the solid phase density, we obtain Eq.(2.138),

$$I = \int r^2 dm \tag{2.137}$$

$$I_l = \int\int\int_S \left[(x - \overline{x}_l)^2 + (y - \overline{y}_l)^2 + (z - \overline{z}_l)^2\right] \phi_{1l}\left(x, y, z\right) \rho_{sl} ds \tag{2.138}$$

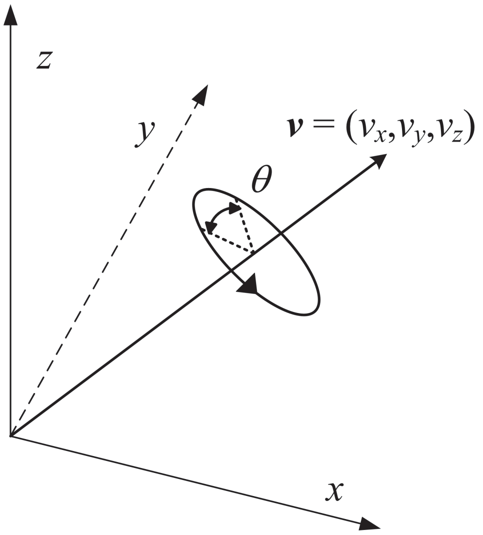

Figure **2.8** The concept of quaternion analysis

The descretization form of Eq.(2.138) is shown in Eq.(2.139),

$$I_l = \sum_{i,j,k} \left[(x - \overline{x}_l)^2 + (y - \overline{y}_l)^2 + (z - \overline{z}_l)^2 \right] (\phi_{1l})_{i,j,k} \rho_{sl} \Delta x_i \Delta y_j \Delta z_k \tag{2.139}$$

On the other hand, the total moments of force Γ_l on the rigid body around the axis x, y, z are expressed as Eq.(2.140)～Eq.(2.142), in which the contribution from all cells within subject based on the solid phase density ϕ_{1l} has been summarized.

$$\Gamma_l^{xtotal} = \iiint_S \Gamma_l^x(x, y, z) ds = \sum_{i,j,k} (\Gamma_l^x)_{i,j,k} (\phi_{1l})_{i,j,k} \tag{2.140}$$

$$\Gamma_l^{ytotal} = \iiint_S \Gamma_l^y(x, y, z) ds = \sum_{i,j,k} (\Gamma_l^y)_{i,j,k} (\phi_{1l})_{i,j,k} \tag{2.141}$$

$$\Gamma_l^{ztotal} = \iiint_S \Gamma_l^z(x, y, z) ds = \sum_{i,j,k} (\Gamma_l^z)_{i,j,k} (\phi_{1l})_{i,j,k} \tag{2.142}$$

where, the moment force at cell (i, j, k) is calculated by Eqs.(2.143)～(2.145),

$$(\Gamma_l^x)_{i,j,k} = (y_j - \overline{y_l}) F_{i,j,k}^z - (z_k - \overline{z_l}) F_{i,j,k}^y \tag{2.143}$$

$$(\Gamma_l^y)_{i,j,k} = (z_k - \overline{z_l}) F_{i,j,k}^x - (x_i - \overline{x_l}) F_{i,j,k}^z \tag{2.144}$$

$$(\Gamma_l^z)_{i,j,k} = (x_i - \overline{x_l}) F_{i,j,k}^y - (y_j - \overline{y_l}) F_{i,j,k}^x \tag{2.145}$$

Herein, F is determined from Eqs.(2.146)～(2.148) with the assumption of neglecting the viscosity effects on the cells,

$$F^x_{i,j,k} = -\left(\frac{\partial p}{\partial x}\right)_{i,j,k} \Delta x_i \Delta y_j \Delta z_k \tag{2.146}$$

$$F^y_{i,j,k} = -\left(\frac{\partial p}{\partial y}\right)_{i,j,k} \Delta x_i \Delta y_j \Delta z_k \tag{2.147}$$

$$F^z_{i,j,k} = \left[-\left(\frac{\partial p}{\partial z}\right)_{i,j,k} - \rho_{i,j,k} g\right] \Delta x_i \Delta y_j \Delta z_k \tag{2.148}$$

Once the moment of force $\mathbf{\Gamma}_l$ is known, the rotational speed can be calculated by Eq.(2.149). The update for the angular speed is then obtained in Eq.(2.150),

$$\frac{d\overline{\boldsymbol{\omega}_l}}{dt} = \frac{1}{I_l}\mathbf{\Gamma}_{\boldsymbol{l}} \tag{2.149}$$

$$\overline{\boldsymbol{\omega}_l}^{n+1} = \overline{\boldsymbol{\omega}_l}^{n} + \frac{d\overline{\boldsymbol{\omega}_l}}{dt}\Delta t \tag{2.150}$$

Then, the rotational axis vector $\overline{\boldsymbol{v}}_l$ and rotation θ_l are determined as a function of the angular speed vector $\overline{\boldsymbol{\omega}}_l$,

$$\overline{\boldsymbol{v}}_l = \frac{1}{\left|\overline{\boldsymbol{\omega}_l}\right|}\left(\overline{\omega}_{xl}, \overline{\omega}_{yl}, \overline{\omega}_{zl}\right) \tag{2.151}$$

$$\overline{\theta}_l = \left|\overline{\boldsymbol{\omega}_l}\right| \Delta t \tag{2.152}$$

Using the just obtained values for Eq.(2.135), Eq.(2.136), the quaternion rotation matrix $\boldsymbol{R}$ is achieved. Then, the coordinate of the center of mass after rotation $\boldsymbol{x}'_l$ is calculated,

$$\boldsymbol{x}'_l = \boldsymbol{R}_l \cdot (\boldsymbol{x}_l - \overline{\boldsymbol{x}_l}) \tag{2.153}$$

Finally, the velocity at all the cells within the rigid body $(\boldsymbol{u}_l)^{n+1}_{i,j,k}$ is updated, as shown in Eq.(2.155), by considering the additional velocity $\boldsymbol{u}^{n+1}_{sl}$ resulted from rotational motion denoted in Eq.(2.154).

$$\boldsymbol{u}^{n+1}_{sl} = \left(\boldsymbol{x}'_l - \overline{\boldsymbol{x}}_l\right)/\Delta t \tag{2.154}$$

$$(\boldsymbol{u}_l)^{n+1}_{i,j,k} = \boldsymbol{u}^{n+1}_l + \boldsymbol{u}^{n+1}_{sl} \tag{2.155}$$

2.7 The Determination of Density, Local Sound Speed and Viscosity

The density of gas phase and liquid phase are calculated by formula experiment equations proposed by Atomic Energy Society of Japan (1993), as shown in Eq.(2.156) and Eq.(2.157).

$$\rho_g = \frac{P}{RT} \tag{2.156}$$

$$\rho_w = 1000 - 2.0 \times 10^{-5} e_w - 1.5 \times 10^{-10} e_w + 0.657 \times 10^{-6} \cdot P \tag{2.157}$$

where, R is the gas constant (R=287.0m^2/s^{2}K), The absolute temperature T and e_w are calculated as follows,

$$T[K] = t[^\circ C] + 273.15 \tag{2.158}$$

$$e_w = 4.174 \times 10^5 + 4434(T - 373) \tag{2.159}$$

In the simulations, the densities of gas phase and liquid phase are calculated with the Celsius temperature t equal to 25°C.

Besides, the local sound speed C_{ls} is calculated with the assumption of the barotropic fluid,

$$C_{ls}^2 = \left(\frac{\partial p}{\partial \rho}\right)_s = \gamma \left(\frac{P}{\rho}\right)_s = \gamma \left(\frac{\partial p}{\partial \rho}\right)_T \tag{2.160}$$

where, γ is the ratio of specific heats, $\gamma = 7/5$ for diatomic gas.

Make a use of the density in Eq.(2.156) and substitute it in Eq.(2.160), the local sound speed in gas phase C_{ls_3} is obtained as follows,

$$C_{ls_3} = \sqrt{\gamma RT} \tag{2.161}$$

The local sound speed in liquid phase C_{ls_2} is calculated by Eq. (2.157) and Eq.(2.160). In this model, the local sound speed in solid phase C_{ls_1} is assumed equal to 5 times of the local sound speed in liquid phase.

On the other hand, the viscosities of gas phase μ_3, liquid phase μ_2 and solid phase μ_1 are respectively equal to 1.8×10^{-5}kg/m/s, 1.0×10^{-3}kg/m/s. The viscosity of solid phase μ_1 is selected equal to 1000 times of the viscosity of liquid phase, by the assumption of a high viscous fluid.

2.8 Interface Tracking Scheme

Computation of moving interface is very importance in numerical simulation of multiphase flow dynamic, but very challenging because the interface that lies between different fluid and moves with the flow field materials as calculations progress. Over recent dedicates, various kind of methods have been proposed to obtain a compact and correctly interface such as the front tracking methods, the level set methods and VOF methods. The front tracking methods (Unverdi and Tryggvason, 1992; Glimm et al.,1998) use Lagrangian interfaces to track the interface on Euler frame. In the level set method (Sussman et el., 1994; Sethian,1999), the signed distance function is used to capture the interface, whereas VOF methods (Hirt and Nichols, 1981; Young, 1982) employ an density (indication) function to define the volume fraction of a certain fluid for each volume. Both the level set methods and the VOF method are straightforward to implement, however, the level set method can not preserve volume of the fluid. The VOF methods, on the other hand, can guarantee well the fluid volume but lacks in the sharpness of the interface. In this study, the tangent transformed CIP method proposed by Yabe and Xiao (1993) is used to track the interface with high accuracy in multi dimensions. The method is combination of the CIP advection solver and a tangent function from the interface. The validity of this method as a sharpness preserving method was discussed in by Yabe (2001).

The tangent transformed CIP method (Yabe, 2001) is explained bellow. Consider K kinds of impermeable materials occupying closed areas $\{\Omega_k(t), k = 1, 2, ..., K\}$ in computational domain $D \in \mathbf{R}^3(x, y, z)$, we identify these material with colour functions or density functions $\{\phi_k(x, y, z, t), k = 1, 2, ..., K\}$ by the following definition:

$$\phi_k(x, y, z, t) = \begin{cases} 1, & (x, y, z) \in \Omega_k(t) \\ 0 & \text{otherwise} \end{cases} \tag{2.162}$$

Suppose these materials with the local velocity u, the colour functions evolve then according to the following advection equation:

$$\frac{\partial \phi_k}{\partial t} + \mathbf{u} \cdot \nabla \phi_k = 0, \quad k = 1, 2, ..., K \tag{2.163}$$

Because solving the above equation by finite difference schemes in an Eulerian representation will result in numerical diffusion and therefore tend to smear the initial sharpness of the interface. In this method, instead of the original variable ϕ_k, it transformation $F(\phi_k)$, is calculated. By specifying $F(\phi_k)$ is a function of ϕ_k only, we obtain an equation similar to equation Eq.(2.163) for the new function $F(\phi_k)$, as follows,

$$\frac{\partial F(\phi_k)}{\partial t} + \mathbf{u} \cdot \nabla F(\phi_k) = 0 \tag{2.164}$$

Therefore, all the algorithm proposed for ϕ_k (CIP algorithm) can be used for $F(\phi_k)$. The simplicity of this kind of technique is very attractive in practical implementation. A transformation by a tangent function is proposed, that is,

$$F(\phi_k) = \tan\left[(1-\varepsilon)\pi(\phi_k - 1/2)\right] \tag{2.165}$$

$$\phi_k = \tan^{-1} F(\phi_k) / \left[(1-\varepsilon)\pi\right] + 1/2 \tag{2.166}$$

where ε is a small positive constant. Introduction of this parameter enable us to avoid the divergence of $F(\phi_k)$ [$F(\phi_k)$ get around $-\infty$ for $\phi_k = 0$ and ∞ for $\phi_k = 1$) and control steepness of the transition layer.

The advantages of this scheme may be explained below. Although $\phi_k = 0$ rapidly changes from 0 to 1 at the interface, $F(\phi_k)$ shows regular behavior. Event if $F(\phi_k)$ is slightly diffusive, ϕ_k is always limited to the range between 0 and 1 due to the characteristic of the tangent function. Additionally, the value of $F(\phi_k)$ evaluated near at $\phi_k = 0$ and 1 smoothly varies, the tangent function transformation can locally improve the spatial resolution near the steep gradients. Therefore, sharp continuity can be easily described. Moreover, without involving any interface construction procedure, this method is therefore very economical in computational cost.

2.9 Wave Source Generation

In the development of the numerical wave tank, the generation of wave source function is very important part because an exact target wave will be achieved by a proper generation treatment. In this study, the finite difference method for non-reflective wave generator proposed by Kawasaki (1998) is employed to realize an idealized numerical wave tank. Herein, wave source generation in the proposed NWT is presented. An review about non-reflective wave generator can be found in Ohyama and Nadaoka (1991).

By considering the wave generation source, the conservation equation of mass is explained by volume integration form as follows,

$$\int\int\int_{\Delta V}\left(\frac{\partial\rho}{\partial t} + \frac{\partial(\boldsymbol{u}\rho)}{\partial\boldsymbol{x}}\right)dxdydz = \int\int\int_{\Delta V}\rho q(y,z,t)\,dxdydz \tag{2.167}$$

where, $x = x_s$ is the grid size at the source position, ΔV is the cell volume.

Taking a difference for Eq.(2.167), Eq.(2.168) is obtained. Then, Eq.(2.169) is obtained from Eq.(2.168) by a simple reduction.

$$\left(\frac{\partial\rho}{\partial t} + \frac{\partial(\boldsymbol{u}\rho)}{\partial\boldsymbol{x}}\right)\Delta x_s \Delta y_j \Delta z_k = \rho q(y,z,t)\,\Delta y_j \Delta z_k \tag{2.168}$$

$$\frac{\partial\rho}{\partial t} + \frac{\partial(\boldsymbol{u}\rho)}{\partial\boldsymbol{x}} = \frac{\rho q(y,z,t)}{\Delta x_s} \tag{2.169}$$

where, the source wave generation source q is determined as in Eq.(2.6).

The wave source strength $q^*(y, z, t)$ is defined as Ohyama and Nadaoka (1991). $q^*(y, z, t)$ is also gradually increased in order to have a smooth transition from still water ahead of the wave train to a fully wave train, as mentioned by Brorsen and Larsen (1987),

$$q^* = \begin{cases} \{1 - exp\left(-2t/T_i\right)\} \cdot 2U_0\left(\eta_0 + h\right) / \left(\eta_s + h\right) & : t/T_i \leq 3 \\ 2U_0\left(\eta_0 + h\right) / \left(\eta_s + h\right) & : t/T_i \geq 3 \end{cases} \tag{2.170}$$

where, t is the time from the start of wave generation, T_i is the incident wave period, h is the water surface elevation at the source line. U_0 and η_0 are the time variation of horizontal velocity and water surface elevation. The term ”2” of U_0 in the right hand side of the Eq.(2.170) represents for wave propagation toward both sides of the wave generation source.

2.10 Boundary Conditions

2.10.1 Top and Bottom Boundary Condition

The proposed NWT in this study is based on a multiphase flow model, which considers air phase in the computational domain. Therefore, not only open and bottom boundary but the boundary condition for top boundary is taken into account. In this study, an impermeable condition for normal velocities and slip condition for tangential velocities are utilized to treat top and bottom boundary.

2.10.2 Energy Dissipation Zones

In a numerical wave tank, it is known that the transmitted and reflected waves, as well as the disturbances radiated by the body can reach edges of the computational domain within the calculation time. This problem will result in the inaccuracy of the calculation results. Whereas, the sizes of a computational domain should be finite to get a reasonable calculation cost. In order to prevent the above-mention problems and to calculate a computational domain over a long time, an energy dissipation treatment proposed by Cruz et al. (1993) is utilized for the numerical wave tank model by adding dissipation zones in the domain and employing dissipation coefficients for three direction $x, y, z,$ as shown in Eq.(2.171). The energy dissipation effects of these zones are then considered through dissipation zone terms, which present in the Navier-Stokes equation Eq.(2.2). Moreover, in order to improve the effect of wave damping in the energy dissipation zones, the grid sizes in these zones are widened toward to the outmost open boundaries with a geometrical progression, suggested in Hinatsu (1992, as shown in Fig.**2.9**.

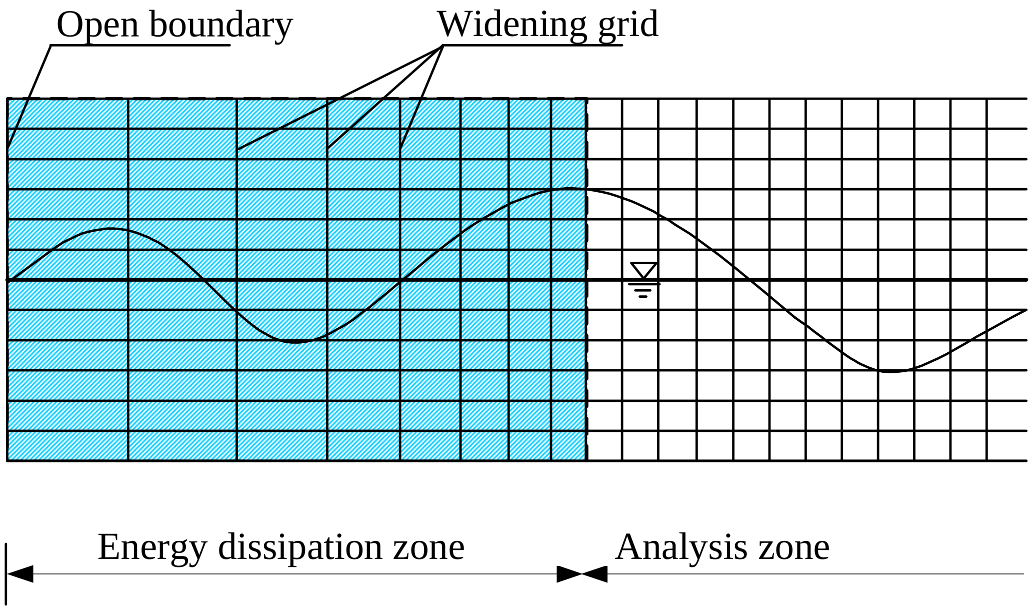

Figure **2.9** Widening of grid system in the added energy dissipation zone

[Dissipation zone term in x direction: $-D_x u$]

$$D_x = \theta_x \sqrt{\frac{g}{h}} (N+1) \left(\frac{x - x_0}{l} \right)^N \tag{2.171}$$

[Dissipation zone term in y direction：$-D_y v$]

$$D_y = \theta_y \sqrt{\frac{g}{h}} (N+1) \left(\frac{x - x_0}{l} \right)^N \tag{2.172}$$

[Dissipation zone term in z direction：$-D_z w$]

$$D_z = \theta_z \sqrt{\frac{g}{h}} (N+1) \left(\frac{x - x_0}{l} \right)^N \tag{2.173}$$

where, h is water depth; l and x_0 are the length of the dissipation zone and the starting coordinate of dissipation zone, respectively; N is the order of dissipation function; θ_x, θ_y and θ_z are dimesionless coefficient.

By various testing, $N = 2$, and $\theta_x = \theta_y = \theta_z = 0.3$ are found appropriate for energy dissipation, therefore these values are used for simulations in this study.

2.11 Verification of the Numerical Wave Tank

A numerical wave tank model based on the multiphase flow model with solid-gas-liquid interaction was proposed in previous sections of this chapter. In order to verify the validity of the

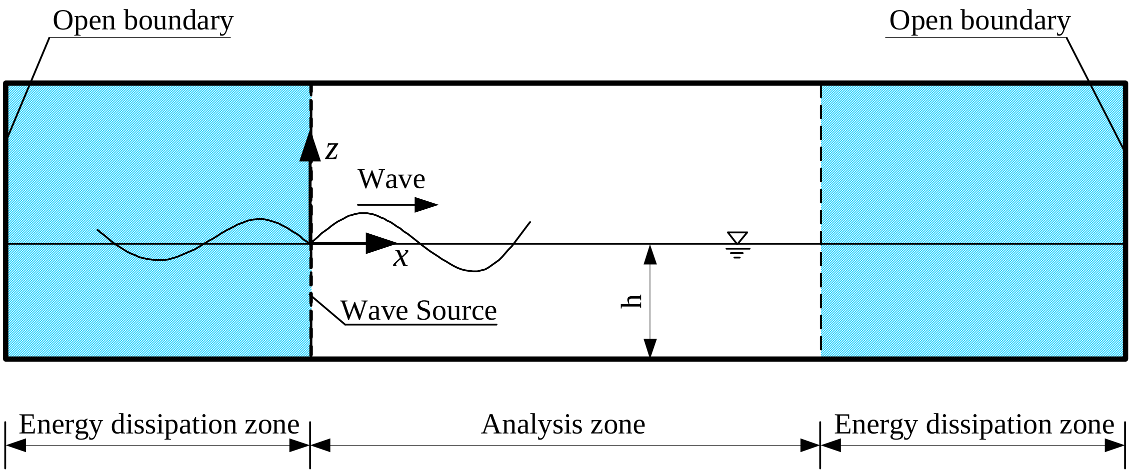

Figure **2.10** Defition sketch of the computational domain

proposed numerical wave tank, this section first examines wave propagation and effect of energy dissipation zones in the numerical wave tank. The validity and utility of the numerical wave tank in reproduce nonlinear interaction between wave and a fixed structure is then investigated through application for analyzing wave propagation over a submerged dike and simulating wave breaking process on different uniform slopes.

2.11.1 Wave Propagation and Effect of Energy Dissipation Zones

(1) Computational Conditions

Figure **2.10** shows a definition sketch of the computational domain. The computation domain includes two energy dissipation zones on the left and the right sides of the domain. The origin of x coincides with the wave generation source, and the positive direction -x is taken toward the right hand side of the computational domain. In the present simulation, the location of the wave generation source was set at the left side of the analysis zone. Mesh sizes in the direction of x, $\Delta x_i/L_i$ and mesh sizes in the direction of z, $\Delta z_k/h$ are 1/100 and 1/40 (L_i: the wave length; h is the water depth), respectively. The time interval at every time step was set at $\Delta t/1000$ so that the Courant condition is always satisfied.

(2) Wave Propagation

The time variation of the normalized water surface profiles $\eta(t)$ at x/L_i = 1.0, 2.0, 3.0, 4.0 are shown in Fig.**2.11** for the wave steepness H_i/L_i = 0.3 and the relative water depth h/L_i = 0.45. As shown in Fig.**2.11**, the calculated normalized water surface profile get the stable and regular stage from the twelveth wave after starting wave generation. These results, therefore, also

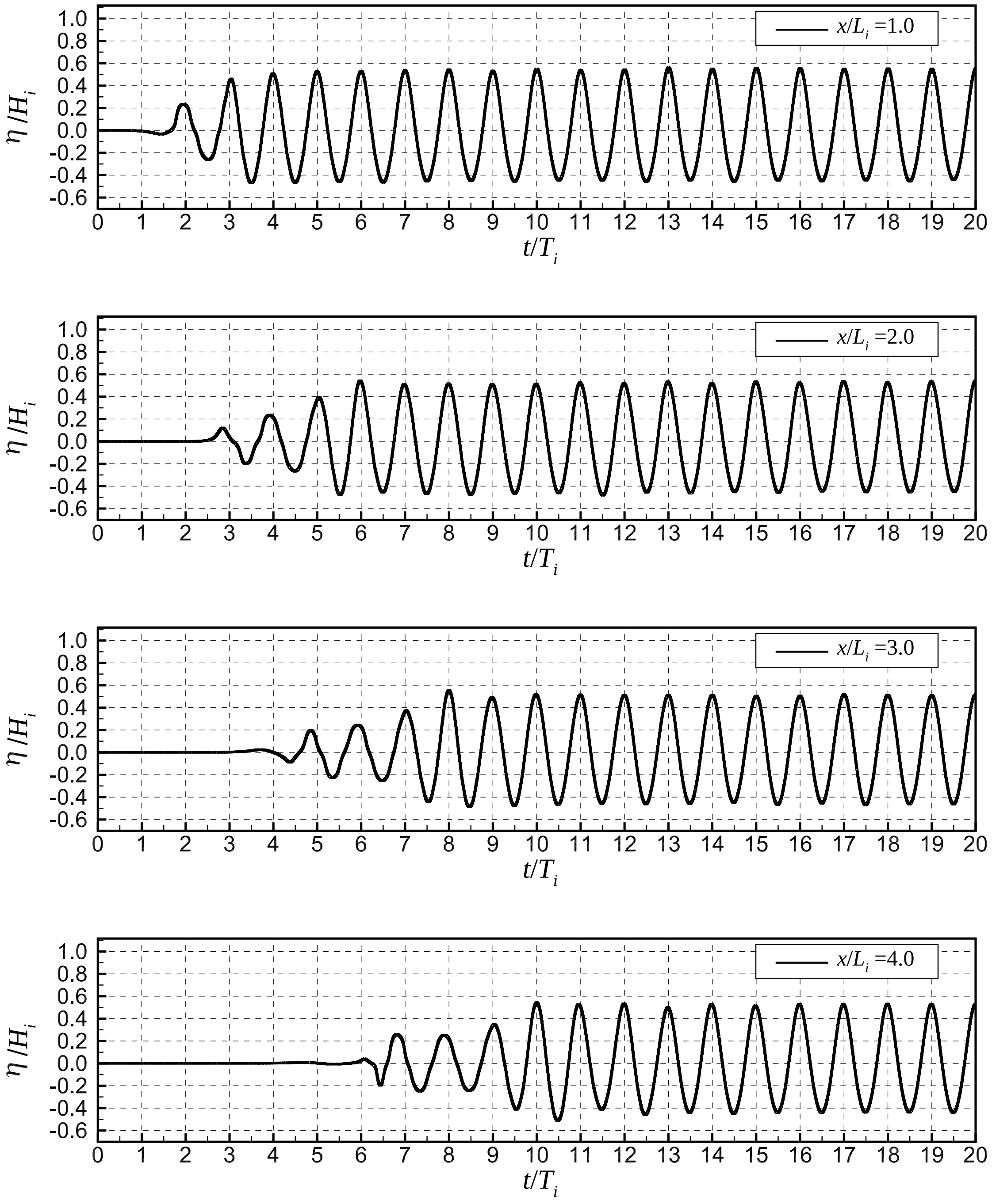

Figure **2.11** Time variation of water surface profile ($H_i/L_i = 0.03$ and $h/L_i = 0.45$)

confirm proposed non-reflection wave generation method, as shown in Eq.(2.170).

Figure **2.12** shows a comparison between the calculated normalized spatial profiles $\eta(x)$ and theoretical one for the computational domain $2.0 < x/L_i < 5.0$. A good comparison between the calculated results and the theoretical one revealed in Fig.**2.12**, indicates that the tangent CIP

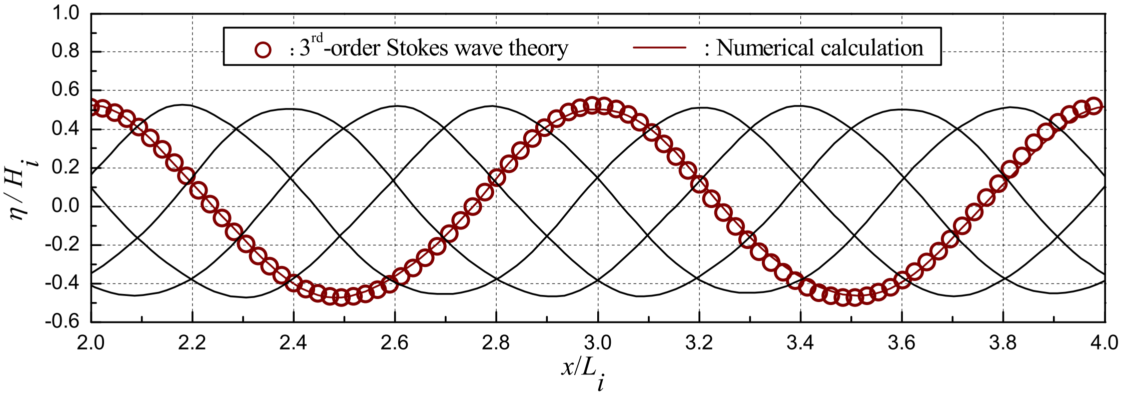

Figure **2.12** Spatial distribution of water surface profile (H_i/L_i = 0.03 and h/L_i = 0.45)

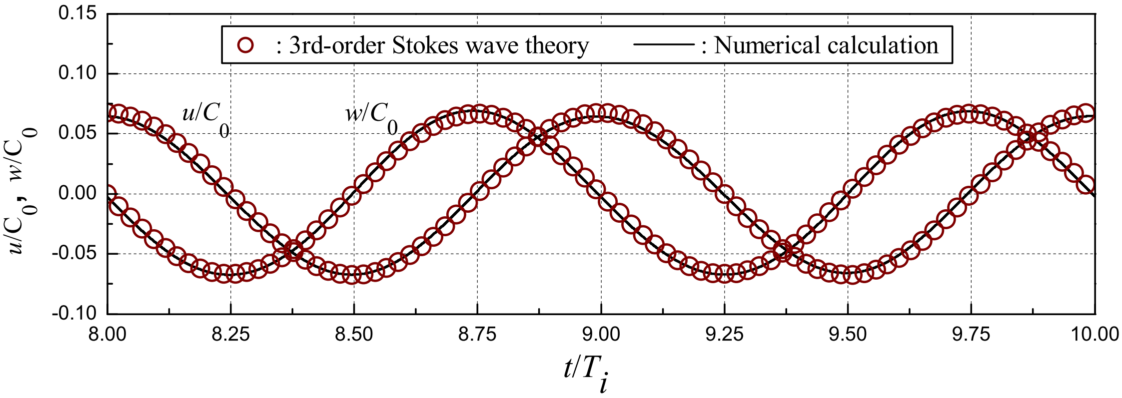

Figure **2.13** Normalized horizontal and vertical velocities (x/L_i = 2, H_i/L_i = 0.03 and h/L_i = 0.45)

scheme utilized in the NWT was successful in tracking water surface.

Figure **2.13** depicts the time variation of theoretical results and the calculated ones in terms of dimensionless wave propagation velocities, where u, w are the horizontal velocity in x and z direction, respectively, and C_0 is wave celerity. It is found from the figure that the calculated results well agree with the theoretical results. The validity of the proposed NWT model in wave propagation, is therefore confirmed.

(3) Effects of Energy Dissipation Zones

Herein, the effects of energy dissipation zones will be verified by examining the water surface profiles at the energy dissipation zones added at both sides of the computational domain.

Figure **2.14** shows the calculated normalized spatial profile of water surface $\eta(x)$ for the whole of the computational domain. It is revealed from Fig.**2.14** that a constant envelope curve of water surface is formed in the analysis domain ($0.0 \leqq x/L_i \leqq 4.0$). In the added energy dissi-

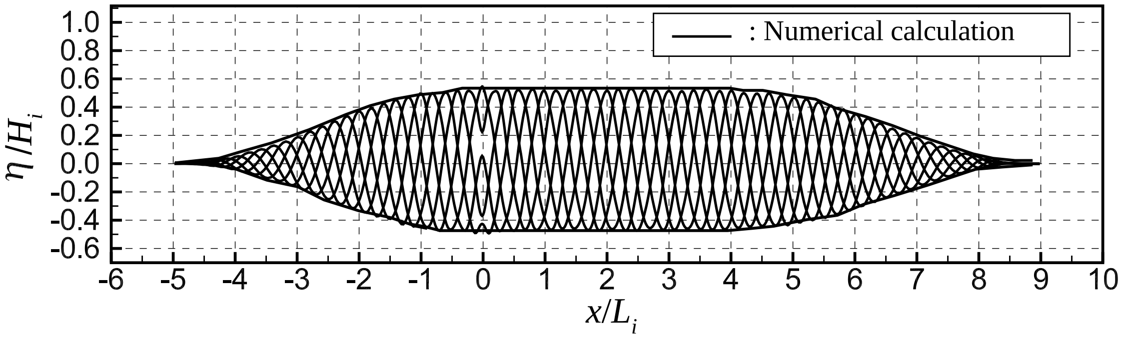

Figure **2.14** Spatial distribution of water surface profile (H_i/L_i = 0.03 and h/L_i = 0.45)

pation zones ($x/L_i < 0.0$ and $x/Li > 4.0$), however, the spatial envelope curve of water surface is gradually attenuated in the added energy dissipation zones, and vanishes near two outmost open boundaries. The successful energy dissipation effect of the proposed dissipation treatment, therefore, are confirmed.

2.11.2 Wave Propagation over a Submerged Dike

(1) Introduction

The submerged structures have been widely applied in coastal engineering field in order to reduce wave action on their landward side as well as promote beach accretion. It is known that the propagation of water wave over a submerged structure plays an important role in keeping its stability and its effect. Therefore, various experimental and numerical studies have been proposed to understand the characteristics of wave propagation over submerged structures.

The propagation of water wave over a submerged dike includes two main physical phenomena. The first is the generation of higher harmonics and the second is the separation of flow and the vortex generation on the onshore side and on the lee side (Huang and Dong, 1999). In terms of experimental studies, the former phenomena has been investigated such as in Dattatri et al. (1978) and Beji and Battjes (1993), while the latter phenomena has been reported by Ting and Kim (1994). On the other hand, the generation of higher harmonic has been numerically predicted on the basis of nonlinear equations for shallow-water wave theories using the Boussinesq equation by Peregrine (1967), Madsen et al. (1991). It was found from these studies that the numerical results of wave height were in good agreement with experimental ones. Most of the numerical above-mentioned studies, however, neglected the viscosity effect, which was found very important to determine flow separation effects over a submerged structure unambiguously without solving the viscous flow equation in the near field (Ting and Kim, 1994).

In this section, the numerical model is used to investigate the interaction between wave and a submerged dike with a trapezoidal cross section shape. The validity of the model is examined through the comparison between numerical results and experimental ones. The generation of higher harmonics, the velocity field and pressure distribution acting on the dikes are furthermore discussed.

(2) Computational Conditions

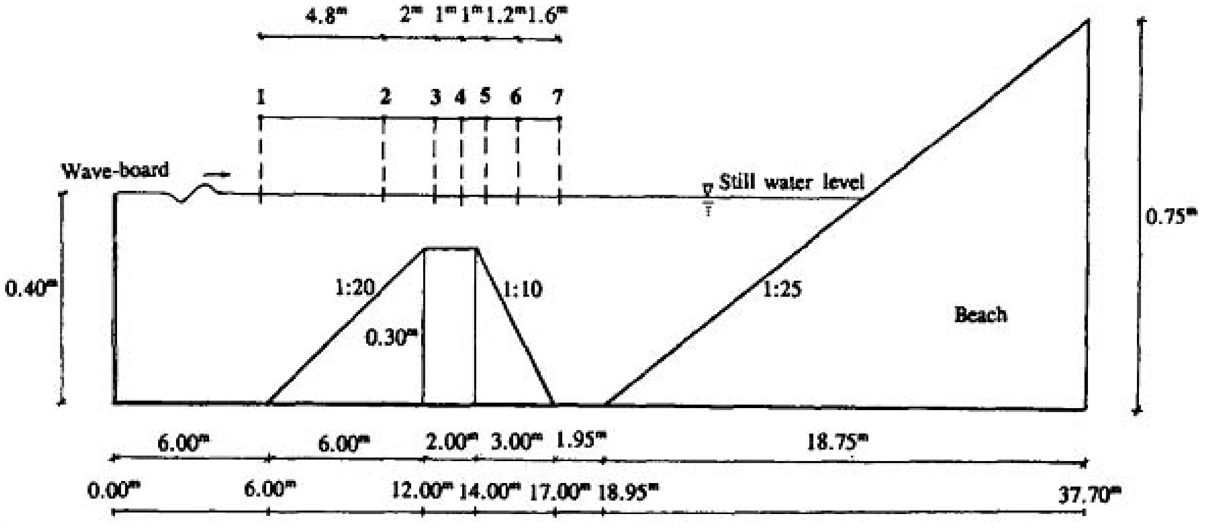

Figure **2.15** Configuration Test (Source: Battjes, 1994)

Figure **2.15** shows the configuration test in the laboratory experiments of Beji and Battjes (1993, 1994), which is used for simulations. The water depth was set constant at 0.40m. The incident wave height *H* and period *T* were 2.0 cm and 2.0 s, respectively. A piston-type wave-maker was installed at one end of the flume. A submerged trapezoidal dike was constructed with an upslope of 1:20 and a downslope of 1:10. The horizontal width of the cross section at the crest level was 2.0m. The height of the horizontal plane section was 0.30 m. At the end of the flume opposite to the wave generator, a beach with a 1:25 slope was presented to dissipate the wave reflection. Water surface elevation was measure at seven stations. The gauge at station 1 served as a reference gauge for the incident wave. Three gauges at station 3, 4, 5 were set around the range over the top of the dike, whereas three remain gauges at station 2, 6, 7 were set at two sides of the dike.

In the numerical calculation, almost dimensions of the laboratory experiment such as distance were kept except the location of wave source was set nearer the dike to decrease the numerical cost. The original coordinate in *x* direction was set at the location of the wave source. Two energy dissipation zone were set from *x*=-11.00m to *x*=0.0m and from *x*=18.40m to *x*=29.50m to prevent the reflection from the left side of the computational domain for all simulations. The submerged dike was immersed in the computational domain by treating as a solid body with a set of the velocity at the gravity center equal to zero in whole calculation time. A sketch of the computational domain is shown in Fig.**2.16**.

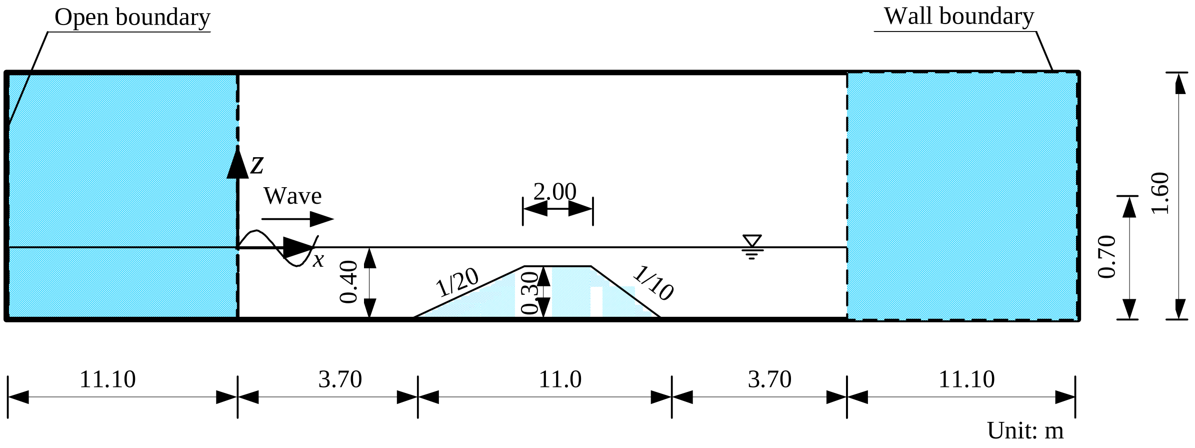

Figure **2.16** Computational domain

(3) Verification of the Numerical Results

Fig.**2.17** shows the temporal variation of water surface elevation at six station gauges from Station 1 to Station 6. It is clearly seen that the numerical results are good agreement with the measured ones. Especially, it is observed from Fig.**2.17** (c)~(f) that the numerical model well reproduces the deformation of wave on the top and the leeside of the submerged dike, where the generation of high harmonic wave of the wave is shown. As a result, it is found that the numerical model is capable of simulating the decomposition of the wave. Moreover, by utilizing a treatment of the submerged dike as a fixed solid body, which was immersed in the computational domain, it can be said that the numerical model can reproduce the nonlinear interaction between wave and fixed structure. Interestingly, a good agreement between the numerical results and measured one was achieved without setting any special treatments for the boundaries of the submerged dike. The validity as well as advantage of the proposed model are, therefore confirmed.

(4) Generation of Higher Harmonics

Figure **2.18** shows the spatial distribution of water surface elevation along the wave channel at different stages. It is shown from the figure that when wave propagate over a submerged

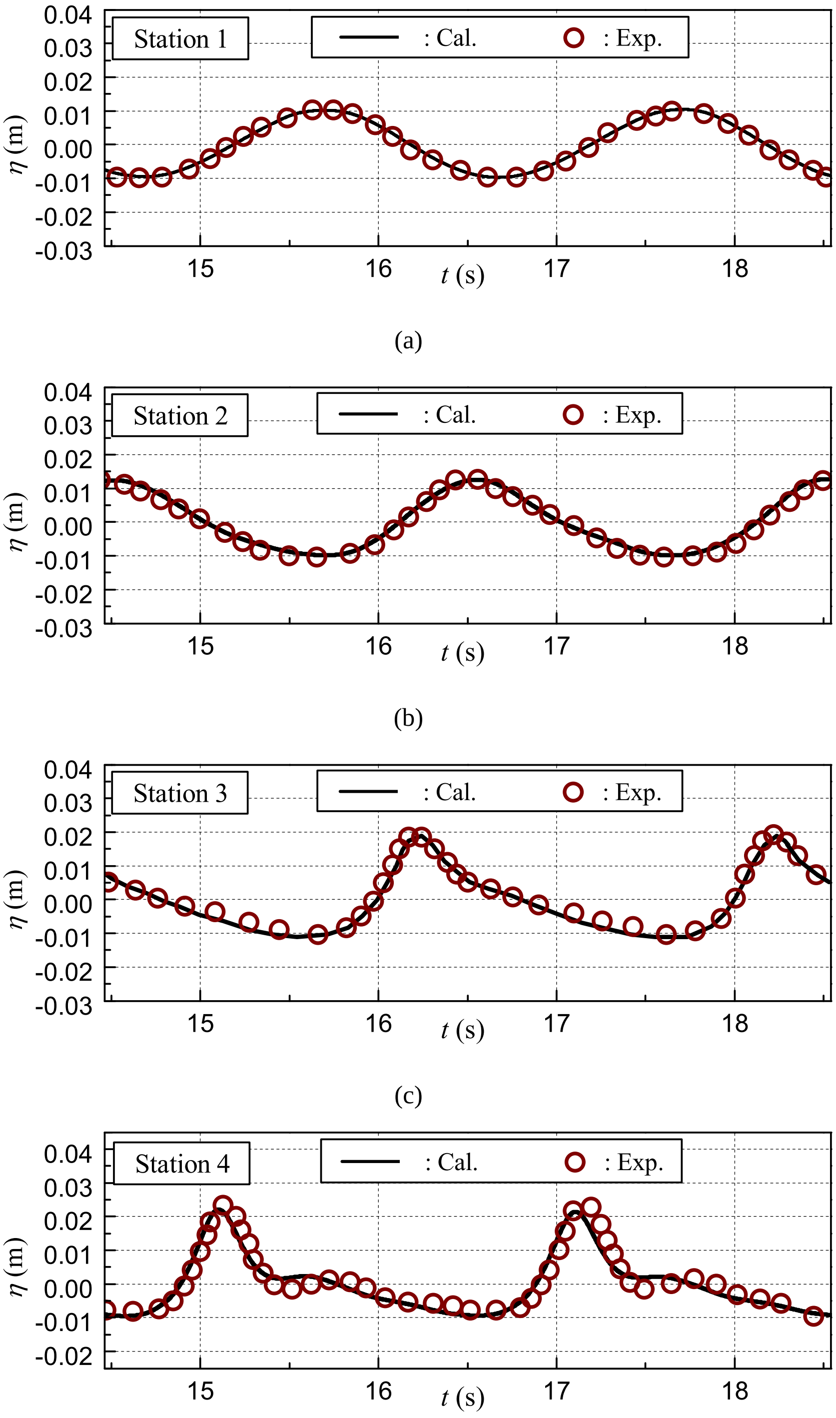

(a)

(b)

(c)

(d)

Figure **2.17** Water surface elevation at several stations (H=0.02m,T=2.0s)

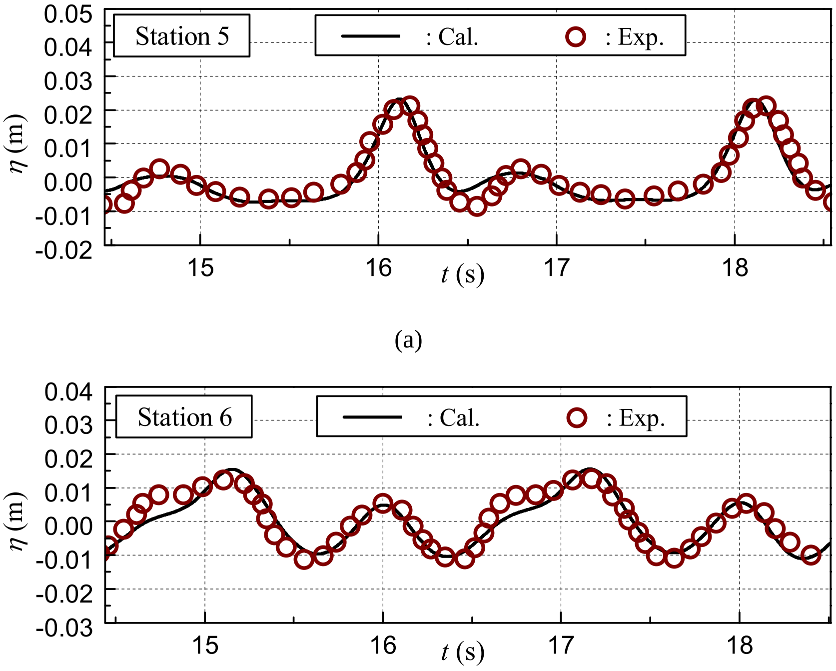

(a)

(b)

Figure **2.17** Water surface elevation at several stations (H=0.02m,T=2.0s) (*continued*)

dike, the wave crest become steeper and a development of the tails is observed. Furthermore, it is found that the water surface elevation undergoes a rapid variation in space as time progress. It can be said that complex interaction between the incident wave and the reflected waves resulting from the interaction between the incident wave and the submerged dike generates the components of these harmonics.

(5) Velocity Field around a Submerged Dike

Figure **2.19** shows snapshots of the velocity field and free surface elevation around the submerged dike at different times. At first, a distribution of velocity field is shown at t=6.00s. It is found from the figure that velocity distribution has not been impacted by the interaction between wave and the dike. When wave propagates over the dike, it is seen from the figures of t= 13.90s~16.10s that the velocity distribution varies rapidly within two ranges determined by around 1 wave length (L=3.69m) far from the both sides of the crest plan of the dike. The large velocities are observed at the free surface and at the crest plan of the dike, where higher harmonics are generated. Considering that these velocities might cause the erosion of materials at the top of the dike, it can be said that the relationship between the generation of higher harmonics and the spatial distribution of large velocities is important to be investigated in practical

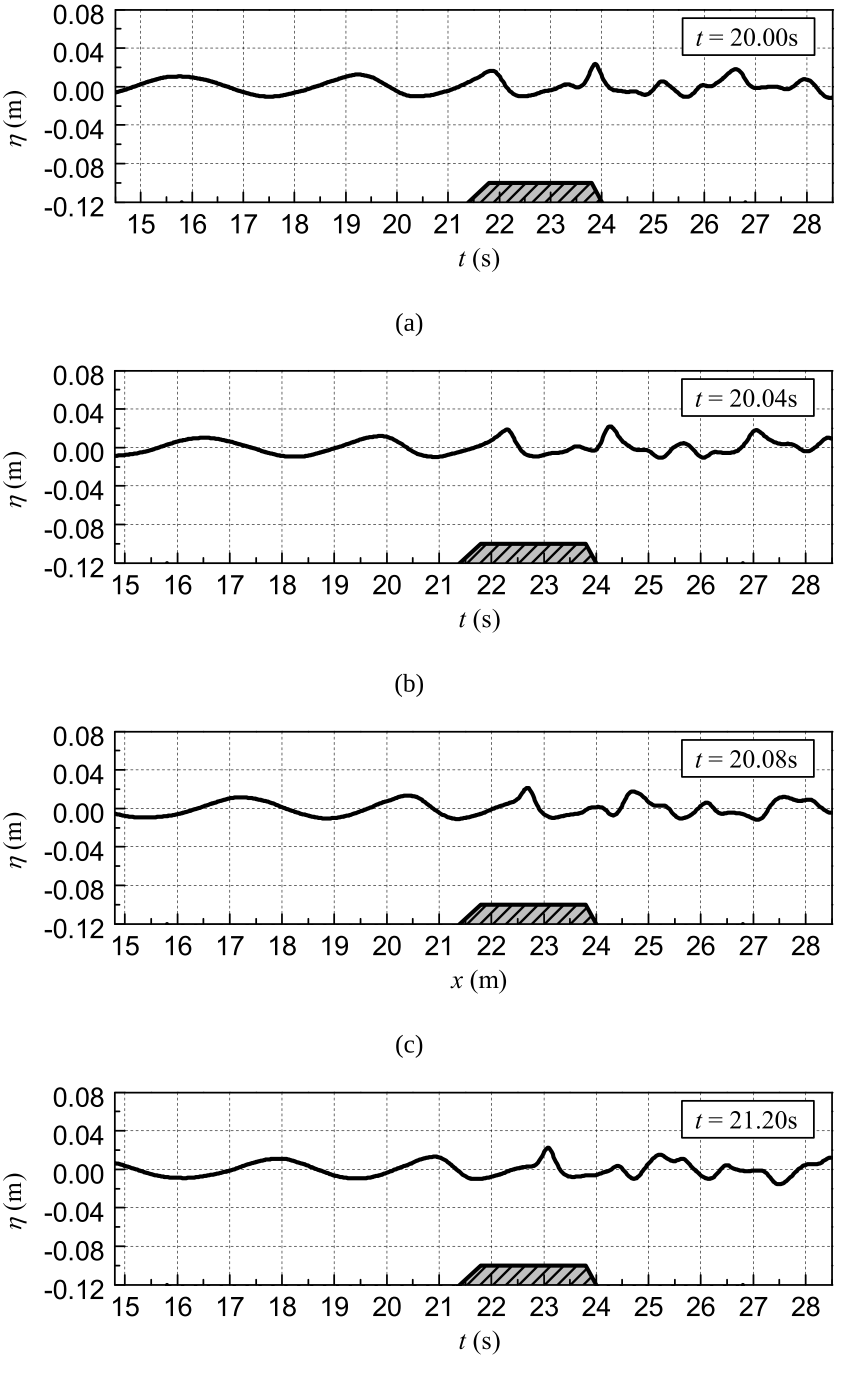

(a)

(b)

(c)

(d)

Figure **2.18** Spatial distribution of water surface elevation along the wave channel(H=0.02m,T=2.0s)

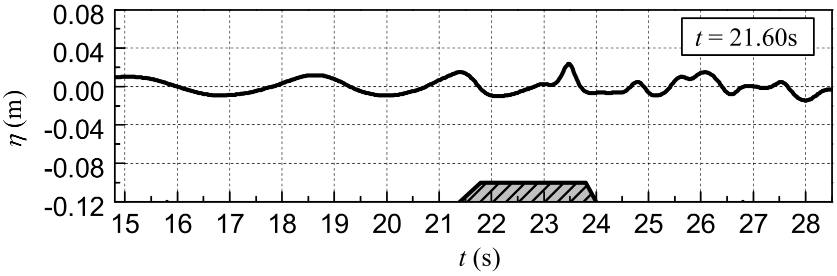

(a)

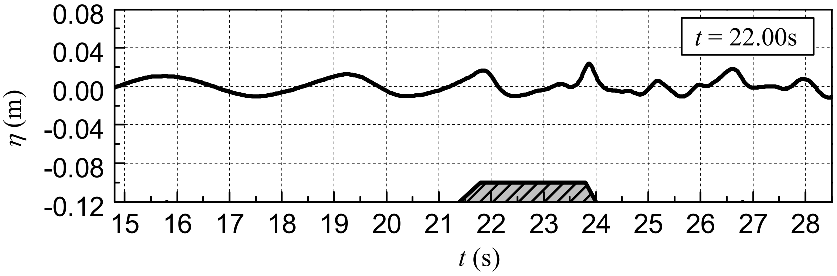

(b)

Figure **2.18** Spatial distribution of water surface elevation along the wave channel (H=0.02m,T=2.0s) (*continued*)

application.

(6) Pressure Acting on the Top of the Submerged Dike

Figure **2.20** shows distribution of the pressure acting on the top of the submerged dike. At starting time of the calculation t=0.00s, the distribution of the hydrostatic pressure is observed in all positions around the dike. When wave propagates over the dike, the dynamic pressure distribution takes place, as shown in the figure from t=13.90s~15.70s. On the other hand, refer to the legend table about the pressure value, it is found from all figures that the dynamic pressure acting on the second layer at both sides (weather side and lee side) of the dike, which is defined from the level of 0.29m downward, is larger than that acting on the first layer at both side of the dike, which is defined from the level of 0.29m to the crest level. Moreover, it is revealed from the Fig.**2.20** at t=15.70s that the pressure acting on the top layer at the weather side is significantly different from that at the lee side with a value accounting for 170N/m^2. This difference might be a cause of a sliding failure of layers of submerged dikes, which has been observed in practice.

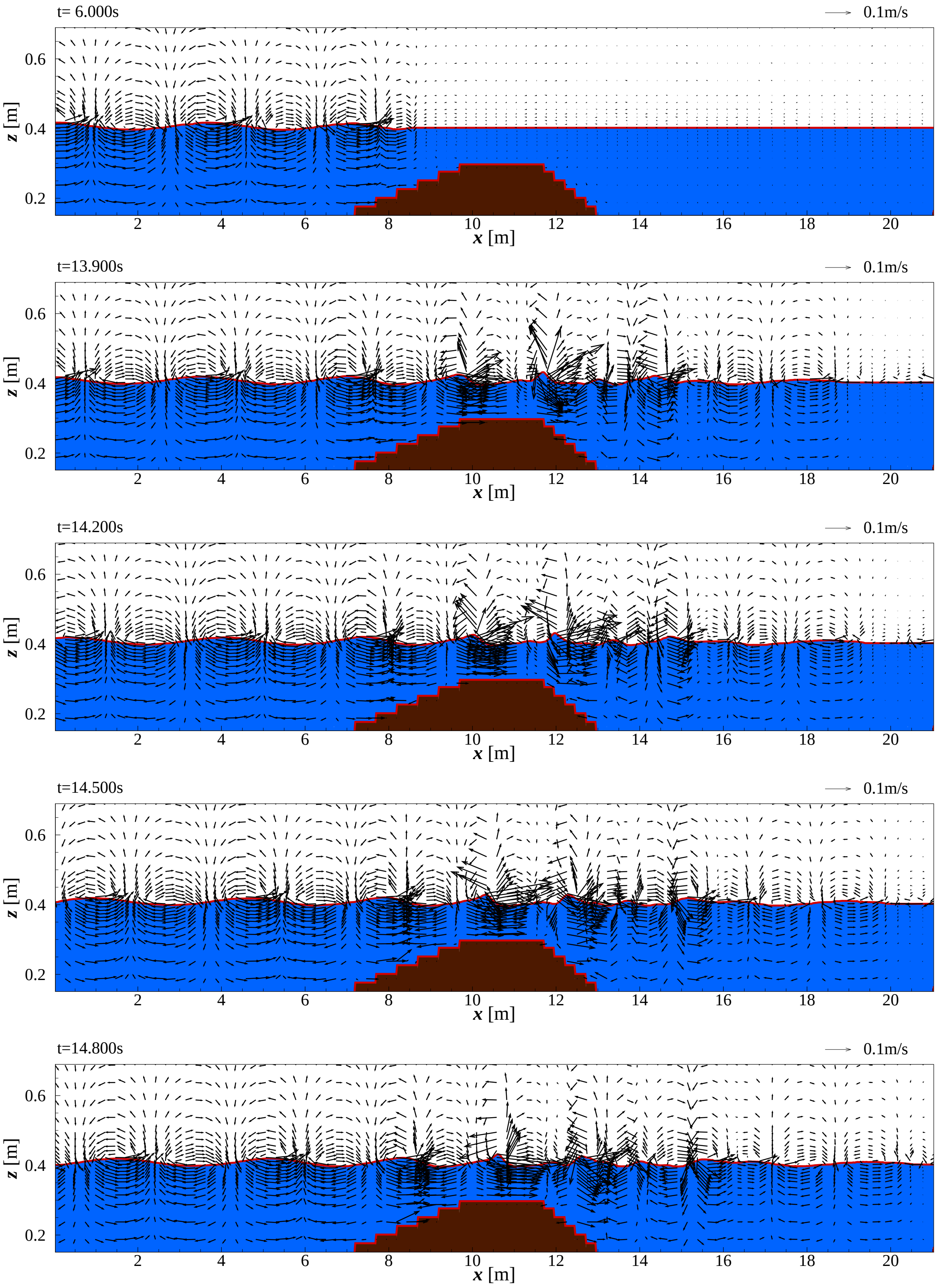

Figure **2.19** Water surface elevation and velocity field (H=0.02m,T=2.0s)

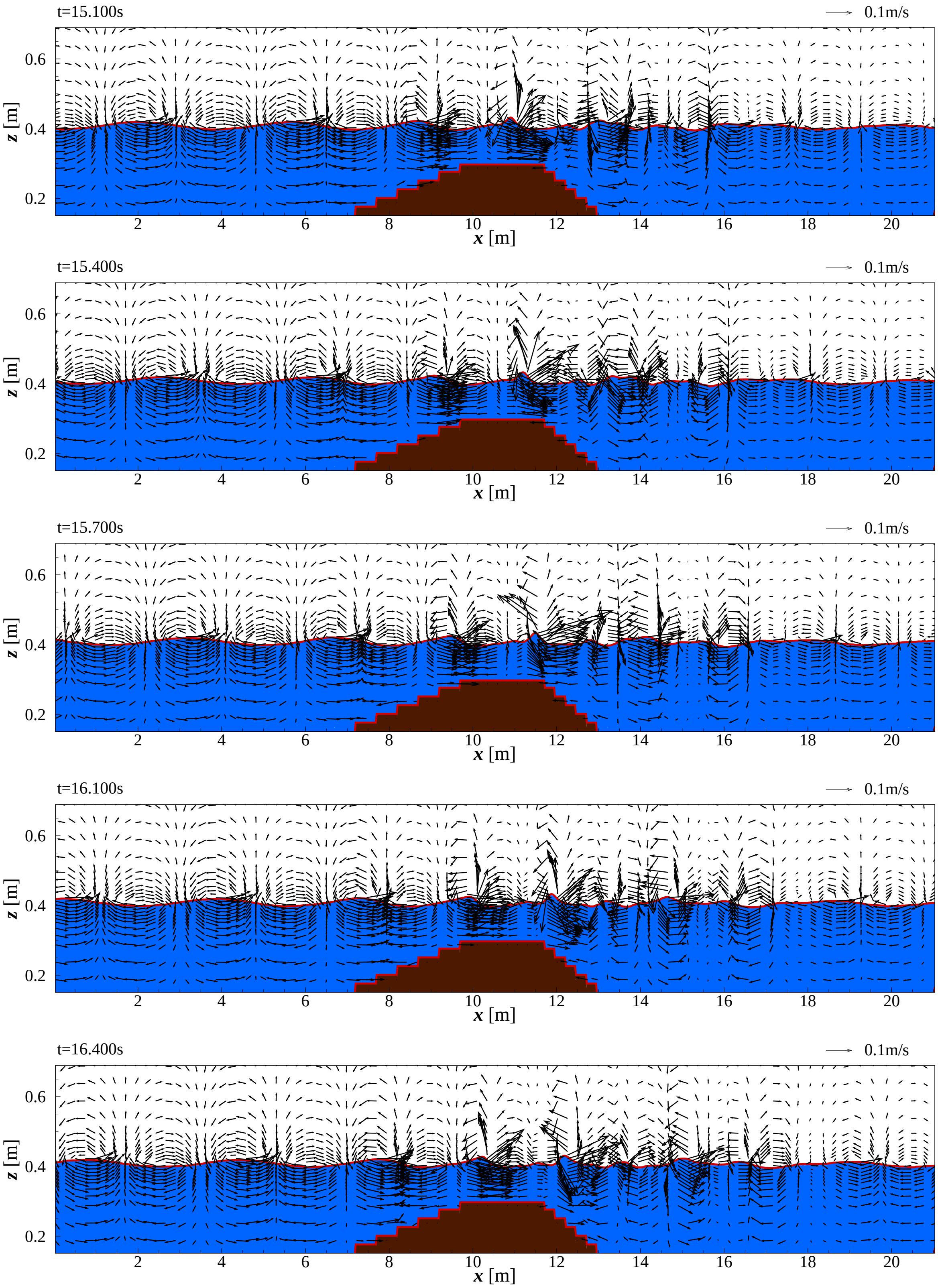

Figure **2.19** Water surface elevation and velocity field (H=0.02m,T=2.0s) (*continued*)

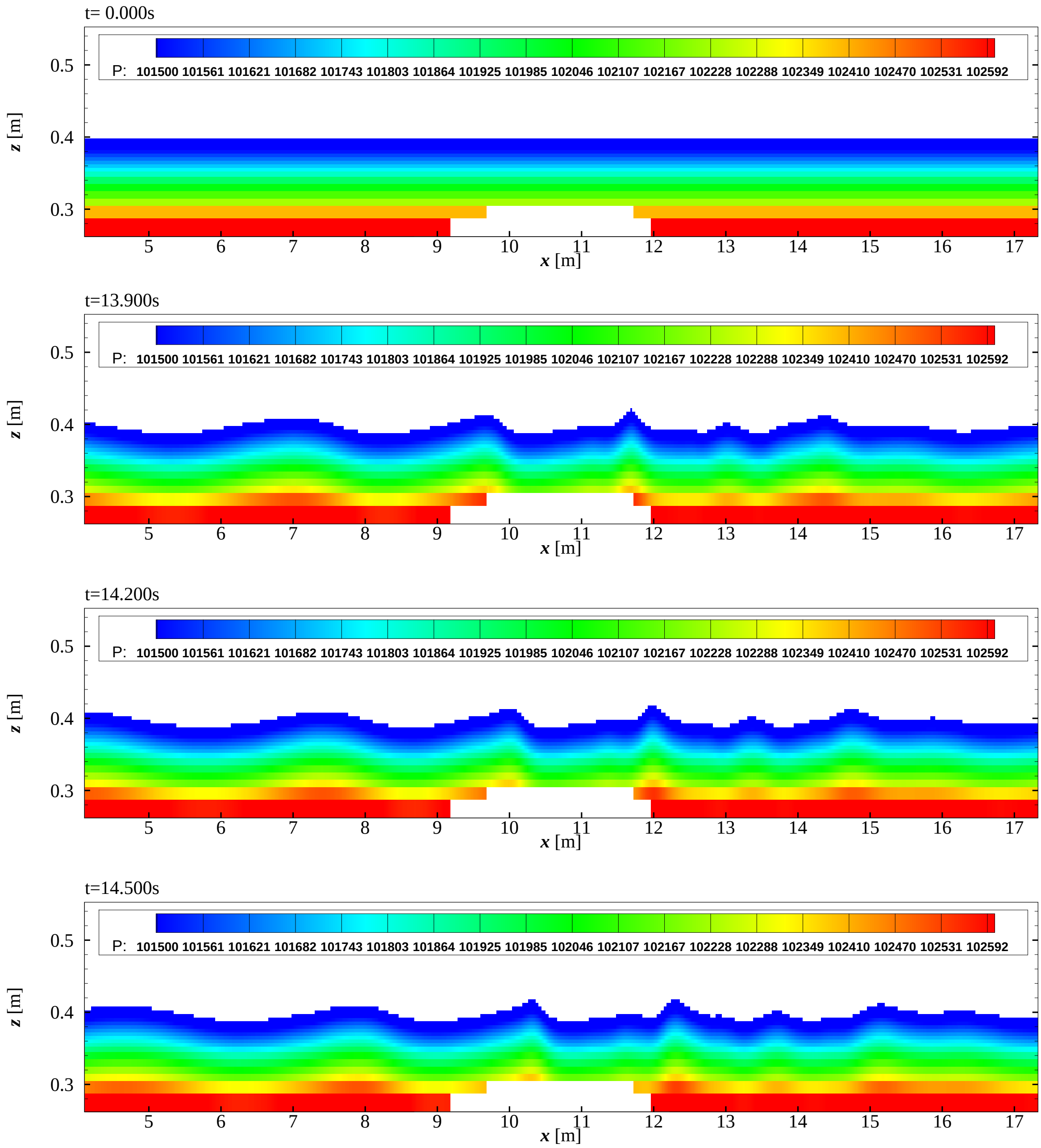

Figure **2.20** Pressure distribution around the top of the submerged dike(H=0.02m,T=2.0s)

2.11.3 Wave Breaking Process on the Uniform Slope

(1) Introduction

When a wave train propagates from deep water into shallow region, its height increases (wave shoaling) and its wave length decreases (Dean and Dalrymple, 1991). As a result, the wave

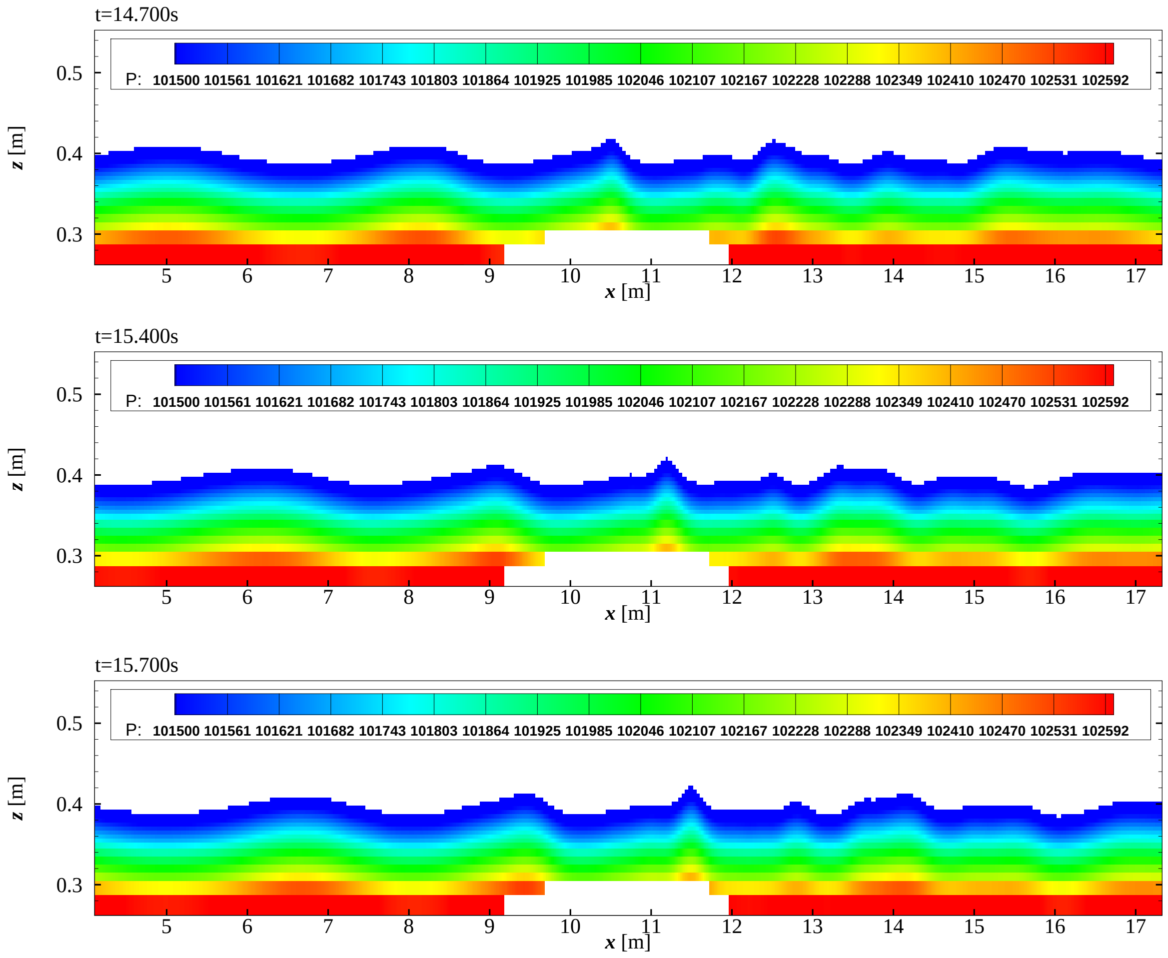

Figure **2.20** Pressure distribution around the top of the submerged dike(H=0.02m,T=2.0s) (*continued*)

profile becomes steep and may break at a certain depth. The wave breaking not only produces a large force, but also induces the nearshore current circulation affecting the shoreline changes (Tsai, 2005). They are, therefore the most interesting phenomena of the wave transformation in the nearshore region.

Variety of theoretical and experimental studies related to the characteristics of wave shoaling and breaking in terms of wave height transformation, the breaking wave condition, undertow, turbulence and so on, has been presented for past decades, such as those of Le Mehaute and Webb (1964), Shuto (1974), Goda (1975), Svenden (1987), Ting and Kirby (1994). On the other hand, numerical simulations have been proposed for understanding natural hydrodynamic process in the coastal engineering field. Compared with two former approaches, numerical simulations can easily achieve many detailed hydrodynamic information without high cost. Recently with the rapid developments in the computer technology and computational fluid dynamic methods, several numerical simulations based on solving directly the Navier-Stokes equations have been proposed for investigating many hydrodynamic processes of flow field including wave breaking, such as in Lin and Liu (1998), Zhao et al. (2000). The above-mentioned studies have achieved numerical results in good agrement with experimental ones, however, some discrepancies were found (see Hieu and Tanimoto, 2004). Note that numerical models mentioned above are based on single-phase flow models, in which only liquid phase (water) is considered and the effects of air movement are neglected. This neglect might be a source of errors. The proposed model is expected to overcome these limitations by considering interaction between water and air through the interaction between liquid and gas phase.

In this section, the ability of the model in reproducing wave breaking phenomena is examined through simulating various types of wave breaking on the uniform slope, which are known as ”spilling, plunging, collapsing and surging”. The numerical results are then analyzed and qualitatively compared with theoretical and experimental results presented by Galvin (1968) and Battjes (1974).

(2) Breaker Types

Irribaren and Nogales (1949) proposed a physical parameter named “ the surf similarity parameter ” for determining whether or not wave breaking occurs. The surf similarity parameter is denoted as in Eq.(2.174)

$$\varepsilon = \frac{\tan\beta}{\sqrt{H/L_0}} \tag{2.174}$$

where, β represents the beach slope, H is wave height at the toe of the slope, L_0 is deep water wave length.

Battjes (1974) noted that the breaking wave characteristics, which include breaker type, breaking index γ, the number of wave in surf zone N^*, and reflection coefficient r, can be correlated to the surf similarity parameter, as shown in Table **3.1**. Furthermore, a description of principle breaker types proposed by Galvin (1998) is shown in Fig.**2.21**.

(3) Computational Conditions

For simplicity, the wave condition was kept, whereas the slope was varied to obtain different surf similarity parameters, which are considered to have the correlation with breaking wave characteristics, according to Bettjes (1974). The water depth, the wave height and wave period for all simulations were kept constant at 0.4m, 0.15m and 2.0s, respectively. Surf similarity parameters were then selected based on threshold values shown in Table **3.1**. Once surf similarity were selected, slopes were calculated by using Eq.(2.174). For a mild slope (Case 3.1), the surf

Table **2.1** Breaking wave characteristics and the surf similarity parameter (Source: Battjes,1974)

ε	0.1		0.5		1.0	2.0		3.0	4.0	5.0
Type	spilling				plunging			collapsing surging		no breaking
γ	0.8		1.0		1.1	1.2				
N^*	6-7	2-3		1-2	0-1		0-1			
r	10^{-3}	10^{-2}			0.1	0.4		0.8		

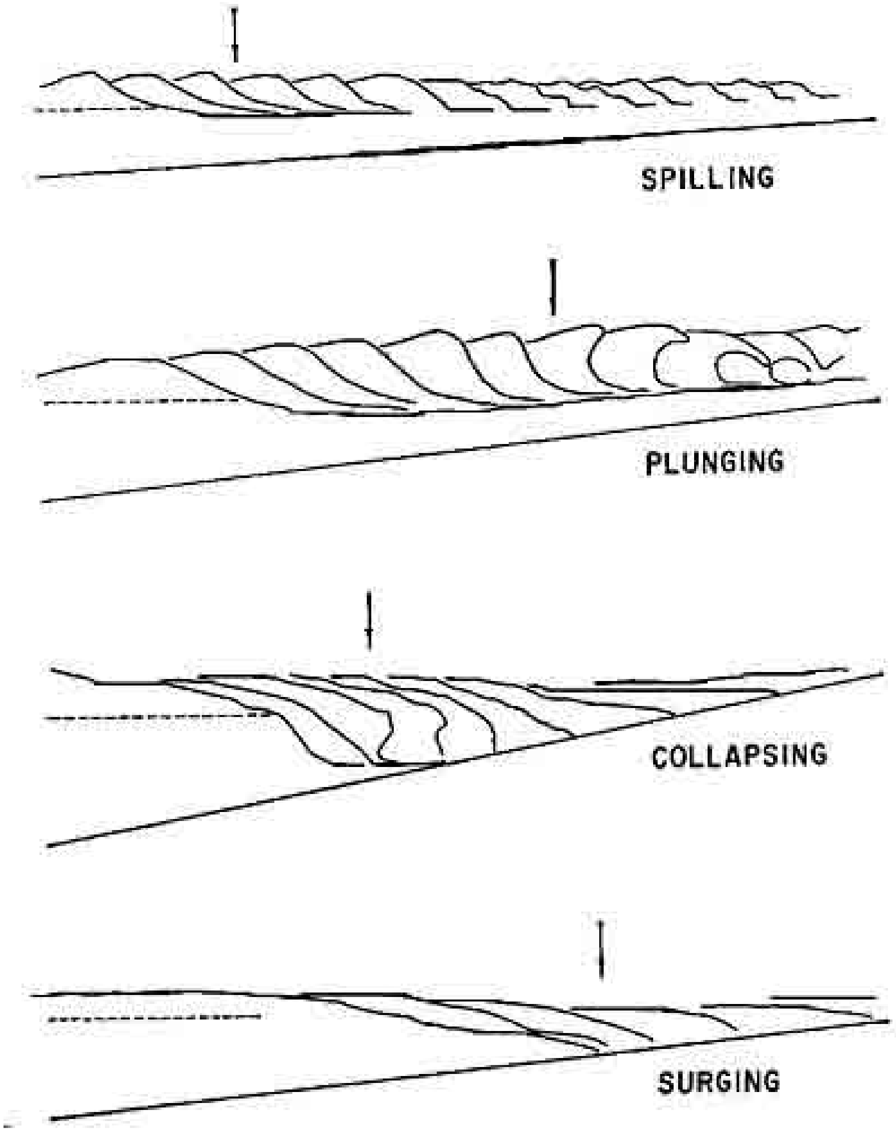

Figure **2.21** Principle breaker types (Source: Galvin, 1998)

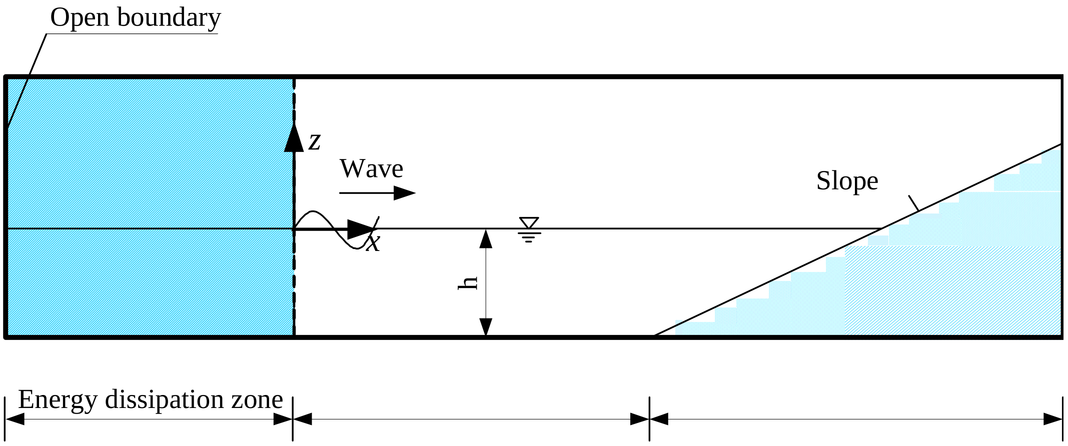

Figure **2.22** Computational domain for breaking simulations

similarity parameter was set 0.32, respective computed slope was 1/20. For a moderate slope (Case 3.2) and a steep slope (Case 3.3), the surf similarity parameters are respectively 0.64 and 2.40, respectively computed slopes are 1/10 and 1/2.5.

Figure **2.22** shows the sketch of the computational domain, in which wave source was located at *x*=0.0m, and a slope with a uniform gradient was set up on the right side of the computational domain. An energy dissipation zone was set from *x*=-10.0m to *x*=0.0m to prevent the reflection from the left side of the computational domain for all simulations.

(4) Wave Breaking on a Mild Slope (Case 3.1)

Figure **2.23** shows the development of wave breaking on a beach with slope 1/20. It is seen that the wave generated by the wave source propagates onshore. Then, in the figures from *t*=9.60s~10.90s, the wave crest become steepen but remain unbroken on the top. In order to see the characteristics of wave breaking, the development of wave breaking and velocity field are further examined in Fig.**2.24**. At *t*=11.0s, wave profile reaches a very steep slope at the crest. Then, from *t*=11.40s~11.90s, it is found that the crest broken and flows down the front face of the wave resulting in spilling down front surface of the water. Consider that the surf similarity of this condition was set 0.32, expecting the occurrence of spilling breaker (refer to Table **3.1**), the numerical model is found capable of reproducing spilling. Moreover, the relation between wave breaking process to the interaction between air and water phase is confirmed through the variability of velocity field in time and space around the breaking position.

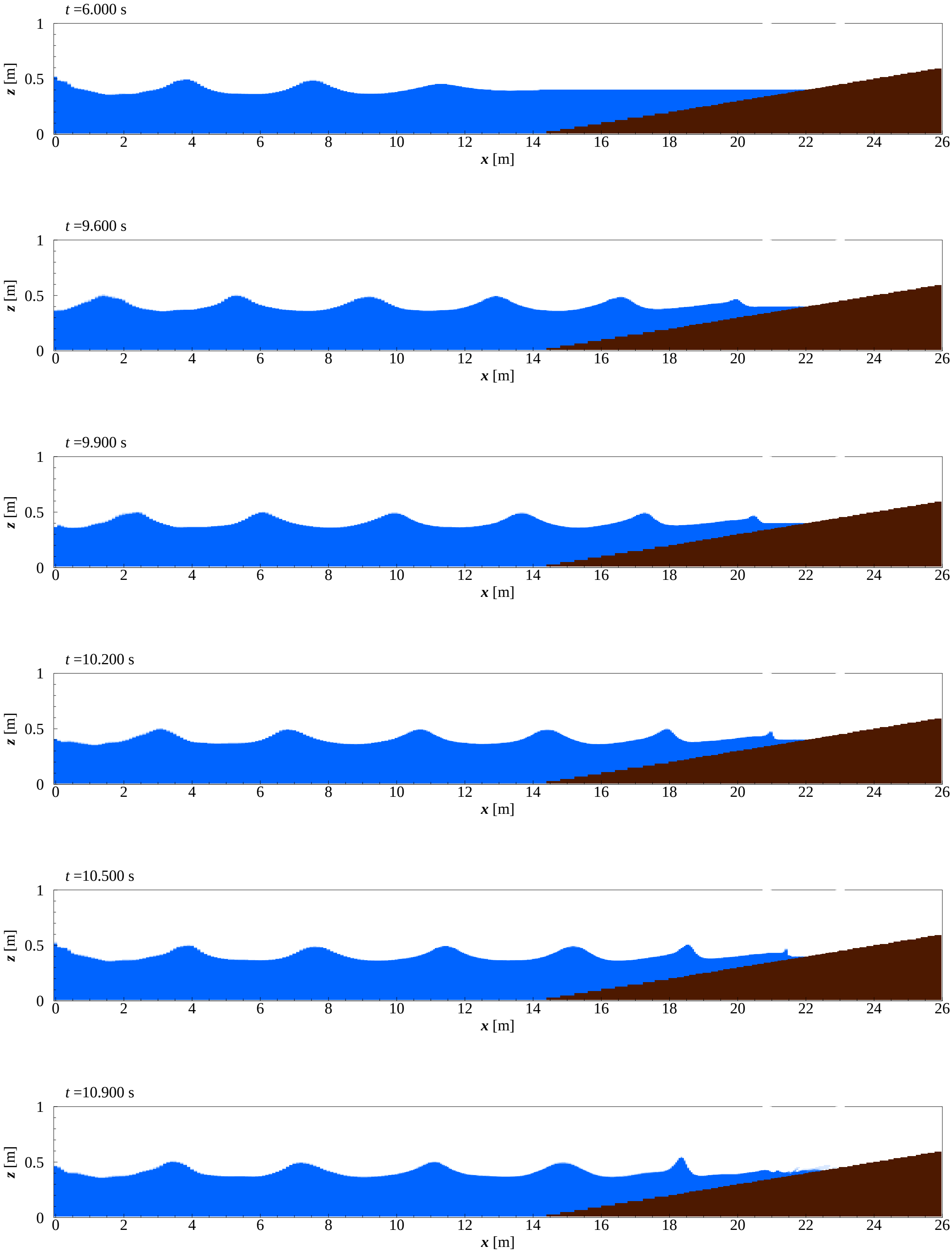

Figure **2.23** Wave breaking on a mild slope (Case 3.1, slope 1/20)

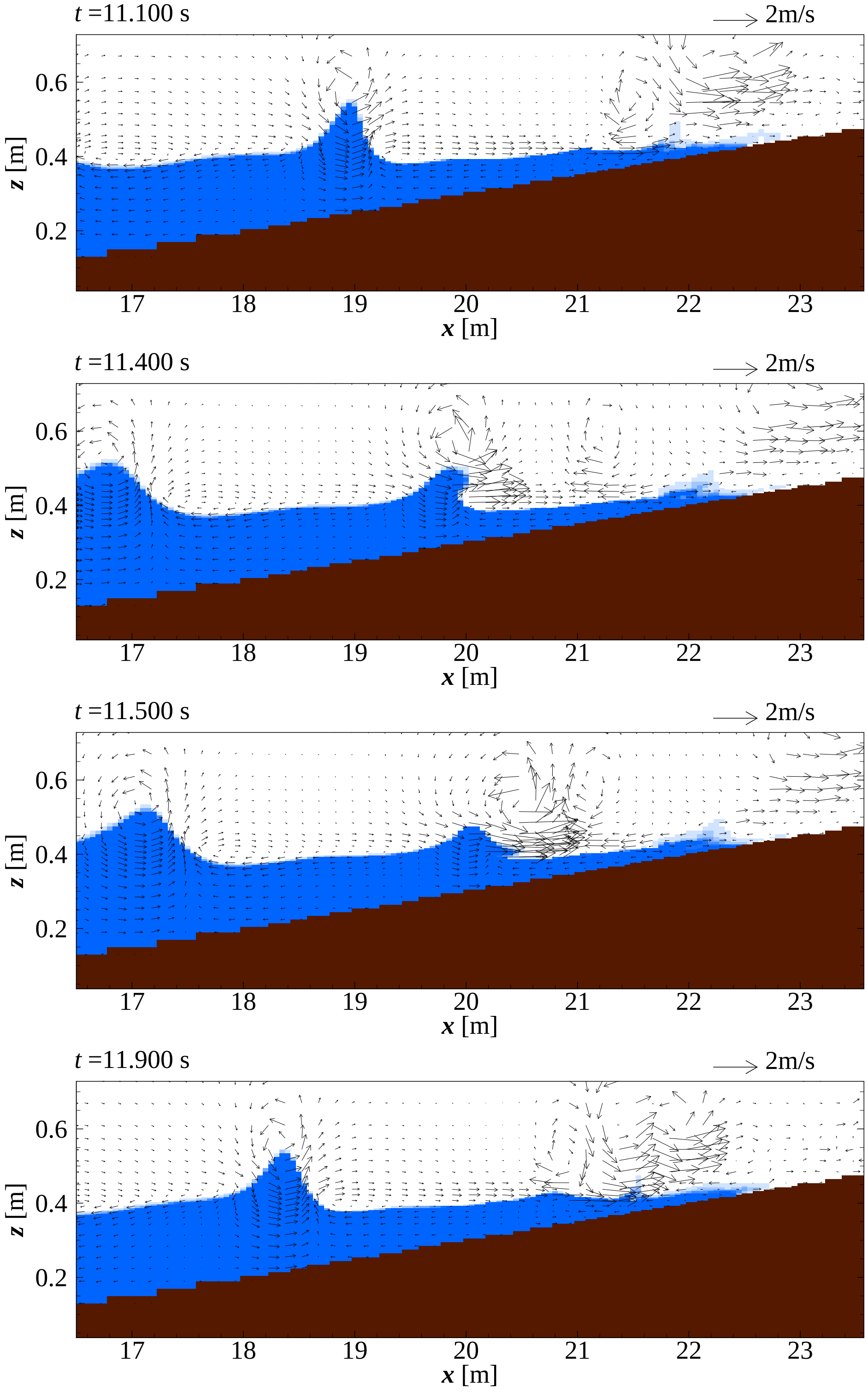

Figure **2.24** Characteristics of wave breaking on a mild slope (Case 3.1, slope 1/20)

(5) Wave breaking on a Moderate Slope (Case 3.2)

Figure **2.25** shows the development of wave breaking on the slope 1/10 (Case 3.2). First, the wave generated by the wave source is found to propagate onshore. In the figures from *t*=7.80s∼8.10s, it is seen that the wave starts to run up the slope and its amplitude increases significantly due to the effect of wave shoaling. From *t*=8.25s∼8.55s, the wave crest continues to steepen and eventually leads to wave breaking. The characteristics of wave breaker is furthermore found in Fig.**2.26** from *t*=10.95s∼11.90s. After experiencing a steepen stage from *t*=10.95s∼11.00s, the wave crest is first observed to curl over front face and impinge onto part of the wave trough, as shown from *t*=11.25s∼11.40s. Compared with breaker type classifications on laboratory experiments proposed by Galvin (1968), which are depicted in the Fig.**2.21**, the development of breaker type “ plunging ” is confirmed. Note that the surf similarity parameter of this cases is equal to 0.645, meaning a prediction of the occurrence of plunging as seen in Table **3.1** , it can be said that the numerical model is capable of reproducing plunging.

(6) Wave Breaking on a Steep Slope (Case 3.3)

Figure **2.27** shows the development of wave propagation on a very steep beach with slope 1/2.5 (Case 3.3). As shown from *t*=0.00s∼6.00s, wave propagates onshore. Then, from *t*=8.10s∼8.55s, it is seen that the wave transformation occurs over a distance of less than wave length *L*=3.69m. The surf zone is seen almost nonexistent. Furthermore, as shown in the figures from *t*=8.85s∼9.45s, the wave crest is found with minor breaking, resulting running up on the slope. Turn back to the classification of Galvin (1968), it is said that surging is occurs. On the other hand, Figure **2.28** shows the development of wave breaking for the slope 1/2.5 after the occurrence of surging. From *t*=9.75s∼10.20s, the wave crest remains flat while the lower part of the front face steepens. Breaker is then found over lower half of the wave. In the next stage, it is revealed that the wave slides up beach with very little production without the development of the bore as for plunging breaker type. Consequently, it is revealed that a mixture of plunging and surging occurs, meaning that wave breaker type is collapsing/surging. With a note of the surf similarity parameter equal to 2.40, predicting a occurrence of collapsing/surging, as shown in Table **3.1**, this revelation confirms the validity of the model in reproducing collapsing and surging.

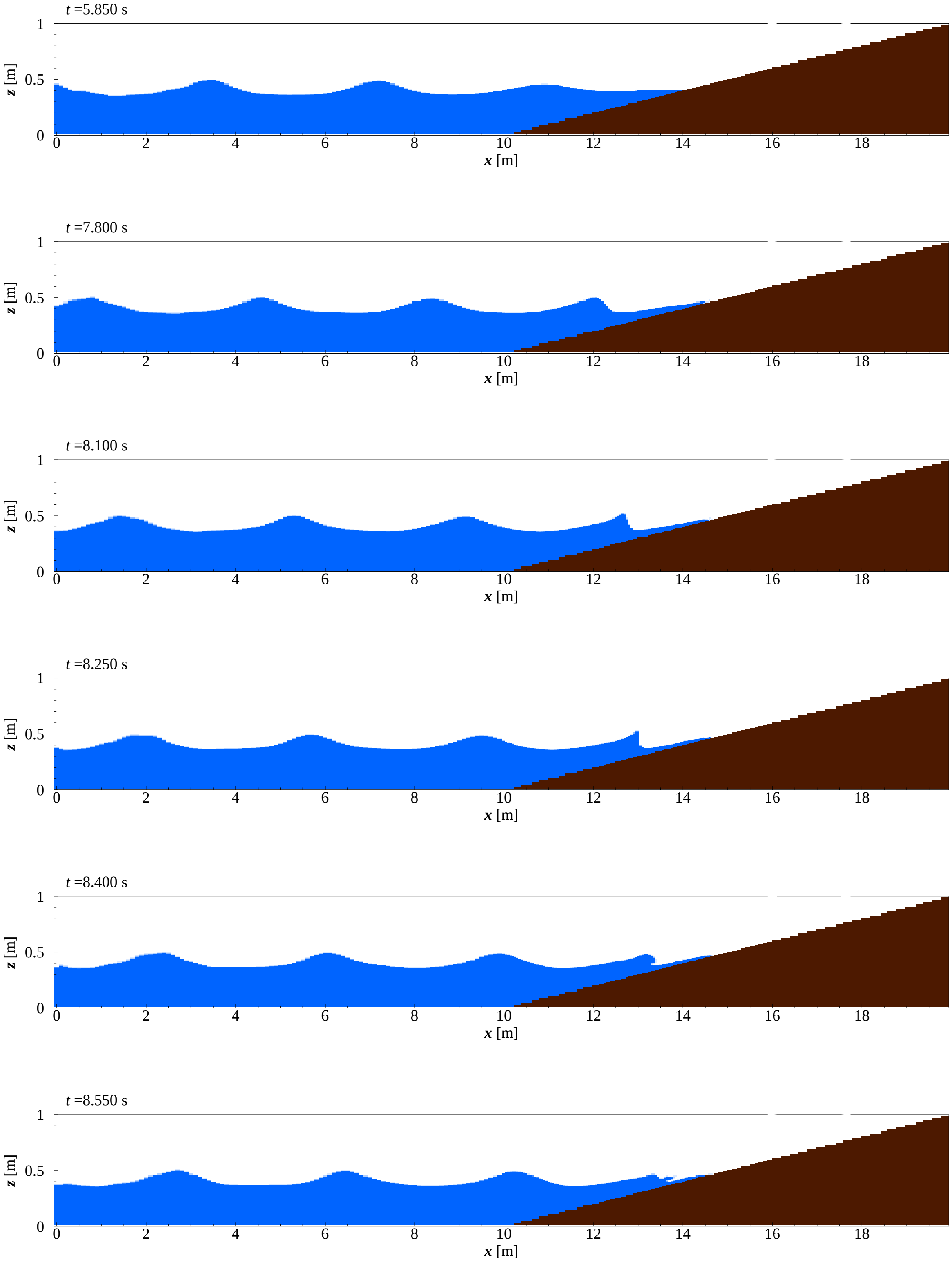

Figure **2.25** Development of wave breaking on a moderate slope (Case 3.2, slope 1/10)

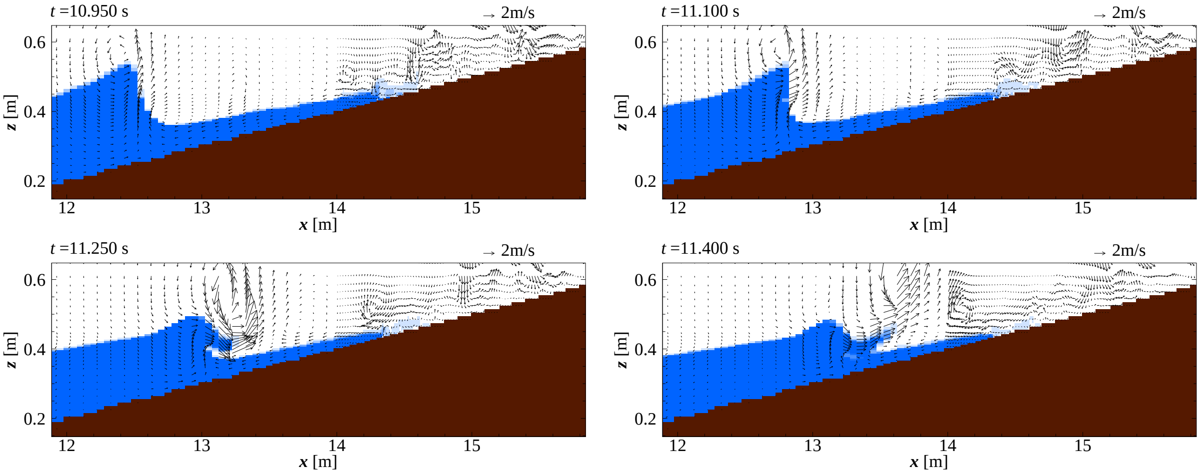

Figure **2.26** Characteristic of wave breaking (Case 3.2, slope 1/10)

2.12 Remarks

This chapter proposed a NWT model based on multiphase flow model with solid-gas-liquid interaction and detailed its methodology. Some figures of the proposed NWT are summarized as follows,

- The flow is represented by one set of governing equations, and therefore no special treatment need for the boundaries among three phases.

- The governing equations are divided into an advection step and non-advection step by making a use of a time splitting technique. In the advection step, CIP methods are used to calculate the hyperbolic equations for all variables. On the other hand, equations at the non-advection step are solved with an extended SMAC method, which can simulate both compressible and incompressible fluid. Moreover, a LES-based DTM turbulence model, and a CIP-CSL2 method for the conservation of mass are incorporated to enhance the computational accuracy.

- A non-reflective wave generator was installed in the analysis domain and energy dissipation zones are employed to realize the NWT.

In order to verify the validity of the proposed numerical wave tank, wave propagation and effect of energy dissipation zones in the numerical wave tank were first examined. The validity and utility of the numerical wave tank were then investigated through applications to analyzing wave propagation over a submerged dike and simulating wave breaking process on different uniform slopes. For the former application, the numerical results were firstly compared with the laboratory experiments conducted by Beji and Battjes (1993, 1994). The generation of higher harmonic, the velocity field around the dike and the pressure acting on the dike were furthermore

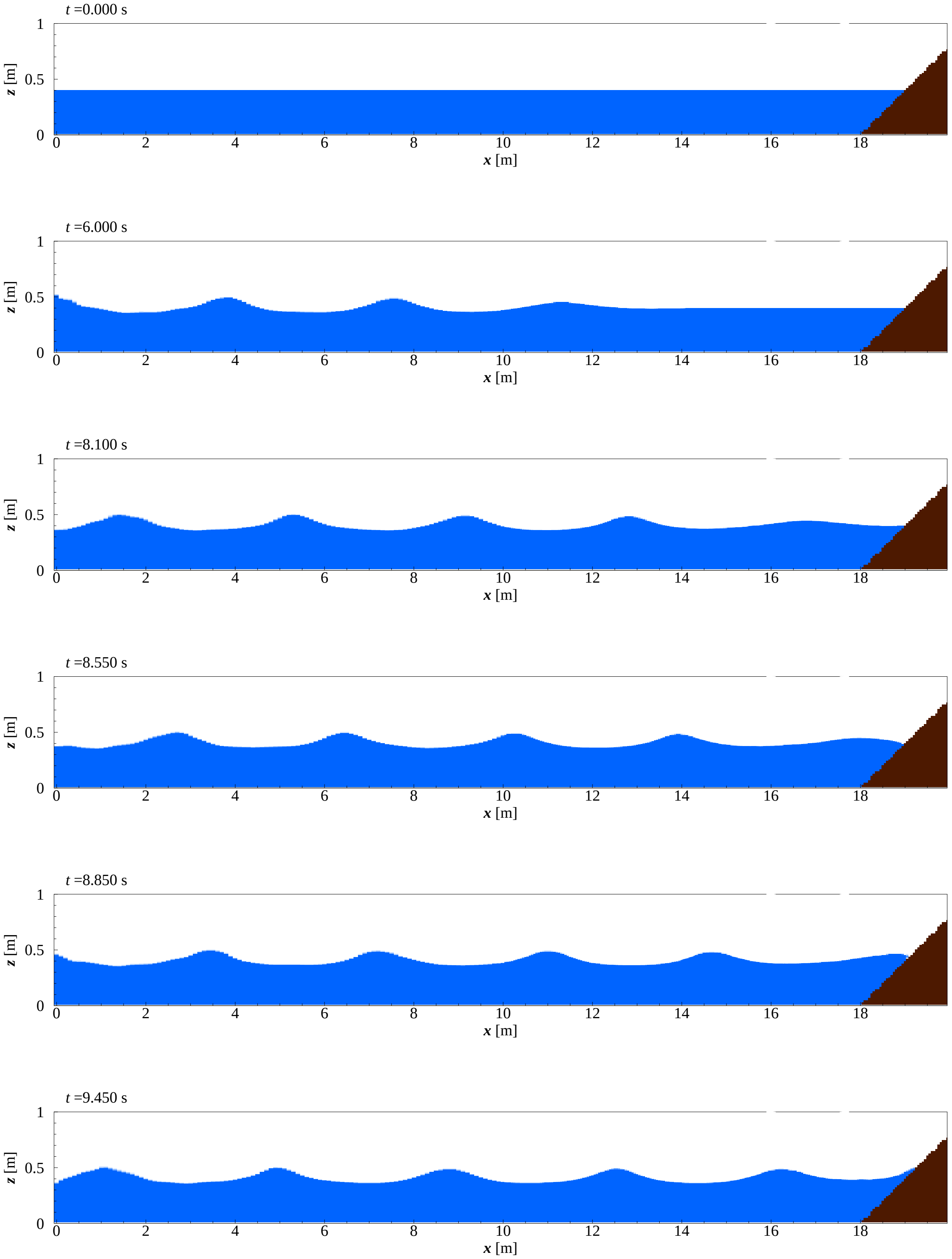

Figure **2.27** Development of wave breaking on the steep slope (Case 3.3, slope 1/2.5)

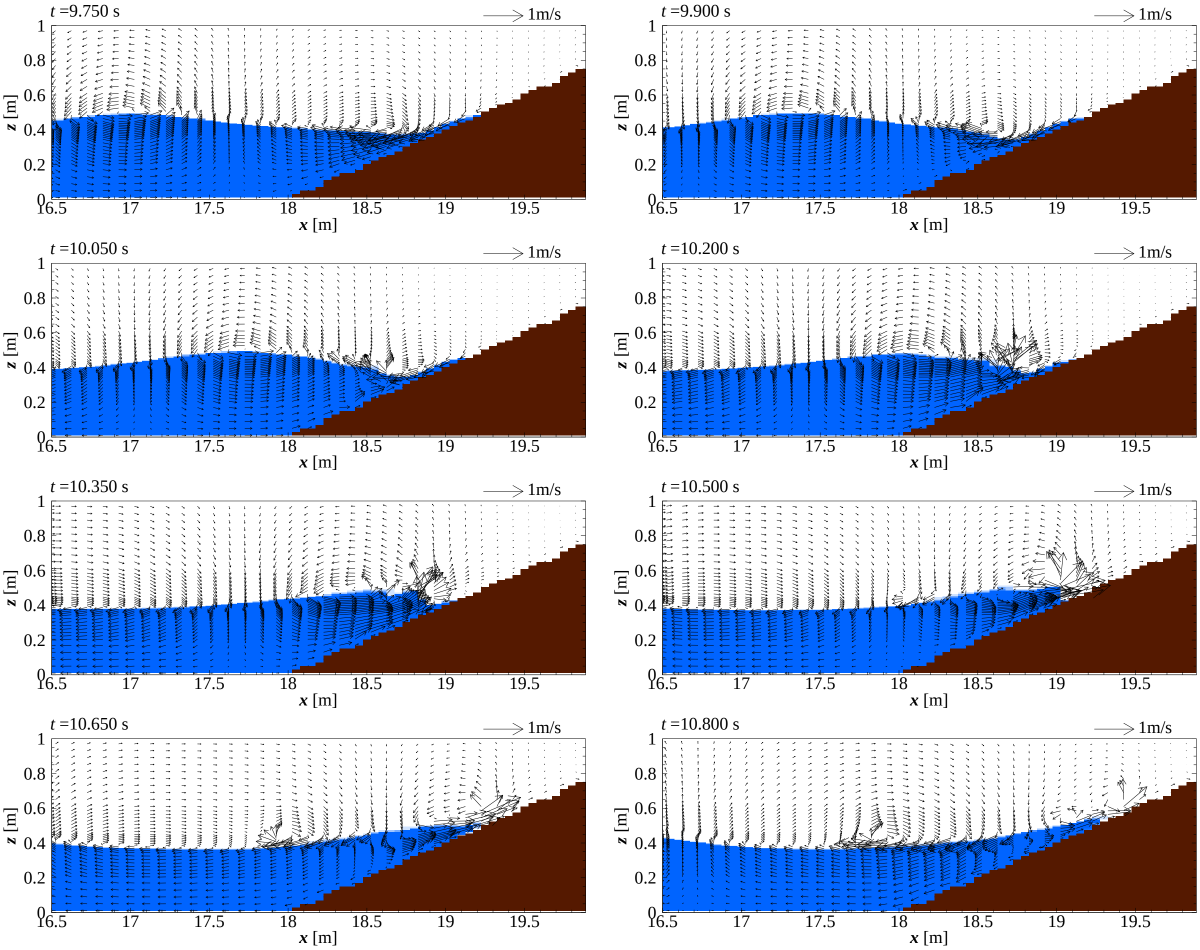

Figure **2.28** Characteristics of wave breaking the steep slope 1/2.5 (Case 3.3, slope 1/2.5)

investigated. It was suggested that the relationship between the generation of higher harmonic and the distribution of the velocity field on the water surface and on the top of the submerged dike should be considered in practical design because the large velocities found on the top of the dike and water surface might cause the erosion of the material on the top of a submerged dike. In terms of pressure acting on the dike, the difference between the pressure acting on the top layer at the weather side and that at the lee side was also suggested to be considered because this difference might result in the sliding failure mode of the dike. For the latter application, the theoretical correlation between the surf similarity parameter and wave breaker proposed by Battjes (1974), was introduced. The numerical model was then used to simulate wave breaking on different uniform slopes. After that, these characteristics were qualitatively compared with the experimental classification about wave breaking on the slope presented by Galvin (1998). Main conclusions about the validity and utility of the numerical wave tank are presented as follows,

- Good agreements between calculated and theoretical results in terms of water surface profiles and water particle velocities verified the validity of non-reflective wave generation method as well as the interface capturing scheme tangent CIP. On the other hand, the examination of spatial distribution of water surface elevation showed the validity of energy dissipation zone treatments.

- In terms of simulating the wave deformation over a submerged dike, good agreement between numerical results and experimental ones confirmed that the numerical wave tank is well capable of reproducing the decomposition of wave. The advantage of a numerical model using Navier-Stokes equation was also shown by obtaining and examining the data of velocity field as well as pressure acting on the dike.

- The simulation results of breaker types for different uniform slopes were found in qualitatively good agreement with theoretical and experimental studies. Note that the simulation of wave breaking phenomena is always considered as a difficult task because of the occurrence of the complex interaction between air and water phase at the interface, the utility of the model in reproducing complex interaction between air and gas phase, is therefore revealed.

In simulations of wave propagation over a submerged dike and wave breaking process on different uniform slopes, slopes and the submerged dike were treated in the computation zones as fixed solid bodies. As a result, it can be said that the numerical model is found capable of reproducing the nonlinear interaction between wave and a fixed structure. The advantages of the proposed model are the consideration of air-water phase interaction and the simple treatment for the boundaries between solid phase and other phases.

CHAPTER 3
NONLINEAR INTERACTION BETWEEN WAVE AND A MOVABLE STRUCTURE

3.1 General

A majority of the world's population lives within coastal zones. These zones are therefore of critical importance to the world's civilians and affect our economic activities. To protect the coastal zones from a threat of storm surge, wave overtopping and so on, a variety of coastal structures such as vertical seawalls, wave absorbing breakwaters and submerged breakwaters have so far been constructed and installed in coastal sea areas. These present structures have considerably contributed to the development of coastal areas, but the global climate change would require the additional improvements of their functions in the near future. Bindoff et al. (2007) reported that global warming has been increasing the sea level, which is predicted reaching 22cm to 44cm above 1990 levels by the mid-2090s. On the other hand, global climate change is recognized as a cause of the increasing severity of storm events. As a result, coastal areas are currently at severe risks from coastal disasters of storm surge, wave overtopping and flooding. Many lives and properties of civilians living at coastal zones have been lost by these disasters, daily life activities sometimes have been damaged as well as interrupted under these disasters, as shown in Fig.**3.1**.

In order to protect the coastal zones from a threat of wave overtopping, various solutions have been discussed in recent years. Sawaragi et al. (1988) examined the effects of artificial reefs on wave overtopping reduction rate. Their results showed that when the height of the reef in the front of a sea dike was given, a proper width of the reef was required to reduce wave overtopping rate. Cornett et al. (1999) investigated systematically the influence of parapets on wave overtopping of vertical-walled structures. They concluded that an overhanging geometry was very effective at reducing wave overtopping rate, but its effectiveness was highly variable, depending on the prevailing water level and wave condition. Kortenhaus et al. (2001) reported

Figure **3.1** Wave overtopping under the 2010 CONSON typhoon at the DOSON coastal town, Vietnam (Source:TTXVN/Vietnam+)

the experimental tests in which wave overtopping and wave loading on a vertical seawall with and without parapet were measured. It was revealed from their study that the effectiveness of the parapet on the reduction of wave overtopping was found only under conditions where the relative crest freeboard R_c/H_s was larger than 1.5 (H_s : significant wave height). Geeraerts et al. (2006) introduced an innovative dike profile named“ Stilling Wave Basin (SWB) ”for the aim of reducing wave overtopping. Wave overtopping reduction factors of 0.44 and 0.48 were derived for the cases of breaking waves and non-breaking waves, respectively. The above-mentioned studies have shown the effectiveness of various structures for reducing wave overtopping rate. However, their approaches should be questioned because the capacities for preventing wave overtopping of the proposed structures depend on the given parameters such as the crests of sea dikes and/or the crest freeboards of parapets, which might not adaptively protect coastal zones from wave overtopping disasters considering sea level rise, high variability of which has been noted in many studies (Fletcher, 2009) .

Recently, Kawasaki et al. (2011) proposed an adaptive countermeasure to protect and mitigate wave overtopping disaster induced by storm surge or high wave, in which a floating panel is installed to the front of an existing upright seawall. Great effectiveness of the floating panel as a countermeasure against wave overtopping by following water surface elevation in front of the seawall was verified by conducting laboratory experiment. The application of this countermeasure at the coastal sites are therefore very promising, however, in order to fully obtain

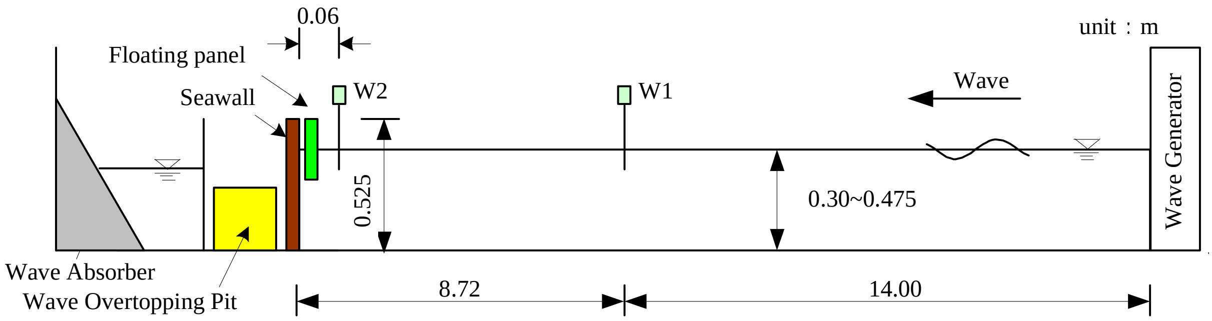

Figure **3.2** Configurations of experimental setup

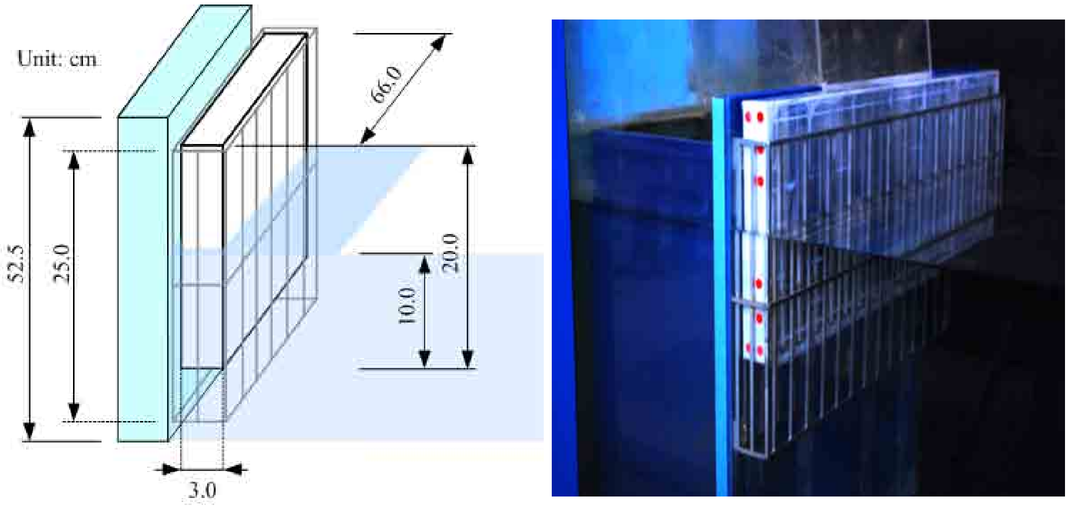

(a) Configuration of seawall, floating panel and frame (b) Three dimension view

Figure **3.3** Schematic of seawall, floating panel and steel frame

data for the technical design stage, not only experimental but numerical investigations should be preformed. Related to investigations on wave overtopping reduction countermeasure using a floating panel of Kawasaki and co-workers, Funahashi (2011) experimentally and analytically discussed the wave overtopping reduction effect of a floating panel with different cross sections under both regular and irregular wave, whereas nonlinear interaction of wave and a floating panel with rectangle cross section under regular wave action is experimentally and numerically studied in chapter 3 of this study. First, the laboratory experiment is analyzed to point out the wave overtopping reduction mechanism of the proposed countermeasure. The proposed numerical model is then utilized to investigate the nonlinear interaction and dynamic behavior of floating panel under regular wave action. The chapter ends with some conclusions.

3.2 Laboratory Experiment

3.2.1 Experiment Setup and Procedures

(1) Experiment Model Description

Hydraulic model experiments were conducted in a two-dimensional wave flume at Coastal and Ocean Engineering Laboratory, Department of Civil Engineering, Nagoya University, as shown in Fig.**3.2**. The scale ratio between model and prototype was set to 1/20. The wave flume (30m long, 0.9m high and 0.7m wide) has a piston-type wave generator at one side, whereas a wave absorber is located at the other side. A floating panel (0.2m high, 0.03m thick, 0.66m wide, and 2.03kg heavy) with a 0.1m draft was installed to the front of an upright seawall with a 0.525m high, which was located at 22.72m far from the wave generator. The horizontal

(a) Installation of HAS-D3 camera (b) Installation of a gutter and a pit

Figure **3.4** Installation camera and overtopped water catchment system

Two capacitance-type wave gauges were installed to measure the time variation of water surface level, as shown in Fig.**3.2**. The first wave gauge W1 was set at 14m far from the wave generator, whereas the second wave gauge W2 was installed just in front of the seawall. In order to examine variations in instantaneous floating panel motion in front of the seawall, an image analysis technique was leveraged in the laboratory experiment. Firstly, some designated points on the one side of the panel were marked by plastic stickers, as indicated in Fig.**3.3**(b). Then, a digital high-speed camera HAS-D3, which was located beside the wave flume, as seen in Fig.**3.4**(a), was used to capture the instantaneous motions of these points as well as the water mass behavior around the seawall. An overtopped water catchment system with a gutter and a pit was also installed behind the seawall to measure wave overtopping quantities, as shown in Fig.**3.4**(b).

(2) Experimental Conditions and Measurements

Laboratory experiments were conducted under regular wave conditions with wave heights of 4cm, 7cm, 10cm, 15cm and 20cm, and wave period of 0.75s, 0.85s, 1.00s, 1.34s, 1.79s and 2.24s. The still water depths for each wave condition were varied with the values of 30cm, 35cm, 37.5cm, 42.5cm and 47.5cm, respectively. The wave conditions and still water depth for each experimental condition were briefly given in Table **4.1**. The initial positions of the floating panel in some experimental conditions were shown in Fig.**3.5**.

The variation of the floating panel motion, the water surface elevation and wave overtopping phenomena around the panel were captured with the digital high-speed camera. The images were then analyzed to obtain numerical data of floating panel motion by employing an image processing program named DIPP-Motion Pro (Ditect Co., Ltd.). On the other hand, wave overtopping quantity for each wave condition was estimated by weighing water mass inside the pit. Herein, in order to investigate the wave overtopping reduction effect of a floating panel, the wave overtopping reduction rate is defined as Eq.(3.1).

$$R = \frac{q_v - q_f}{q_v} \times 100[\%] \tag{3.1}$$

where, q_v is wave overtopping rate for an upright seawall, q_f is wave overtopping rate for an upright seawall with a floating panel. As shown in Eq.(3.1), a large value of R indicates a great effect of a floating panel for wave overtopping reduction.

3.2.2 Experiment Results and Discussions

(1) Effects of Floating Panel for the Reduction of Wave Overtopping

In order to study the reduction effect of a floating panel for wave overtopping under regular wave action, wave overtopping characteristics of an upright seawall and an upright seawall with a floating panel were qualitatively compared through the video images taken in the laboratory experiments. Furthermore, quantitative examinations of wave overtopping rates for both the cases were conducted.

Figures **3.6**(a) and **3.6**(b) show the wave overtopping situations around the seawall without and with a floating panel for the experimental condition of h=42.5cm, H=10cm and T=2.24s. As depicted in Fig. **3.6**(a), a rise of water surface is observed from the first photo to the second

Table **4.1** Experimental conditions for regular wave

N_0	Height of upright seawall h_c [cm]	Water depth h [cm]	Wave height H [cm]	Wave period T [s]
1	52.5	30.00	15	2.24
2	52.5	30.00	10	1.79
3	52.5	30.00	10	1.34
4	52.5	35.00	10	0.85
5	52.5	35.00	10	1.00
6	52.5	35.00	10	1.34
7	52.5	35.00	10	1.79
8	52.5	35.00	15	1.34
9	52.5	35.00	15	1.79
10	52.5	35.00	15	2.24
11	52.5	35.00	20	2.24
12	52.5	37.50	10	0.85
13	52.5	37.50	10	1.00
14	52.5	37.50	10	1.34
15	52.5	37.50	10	1.79
16	52.5	37.50	15	1.34
17	52.5	37.50	15	1.79
18	52.5	37.50	20	2.24
19	52.5	42.50	4	0.75
20	52.5	42.50	4	1.00
21	52.5	42.50	4	2.24
22	52.5	42.50	10	0.85
23	52.5	42.50	10	1.00
24	52.5	42.50	10	1.34
25	52.5	42.50	10	1.79
26	52.5	42.50	10	2.24
27	52.5	47.50	7	1.34
28	52.5	47.50	7	1.79
29	52.5	47.50	10	0.85
30	52.5	47.50	10	1.00
31	52.5	47.50	10	1.34
32	52.5	47.50	10	1.79

(a) h = 35cm

(b) h = 37.5cm

(c) h = 42.5cm

Figure **3.5** Initial positions of floating panel

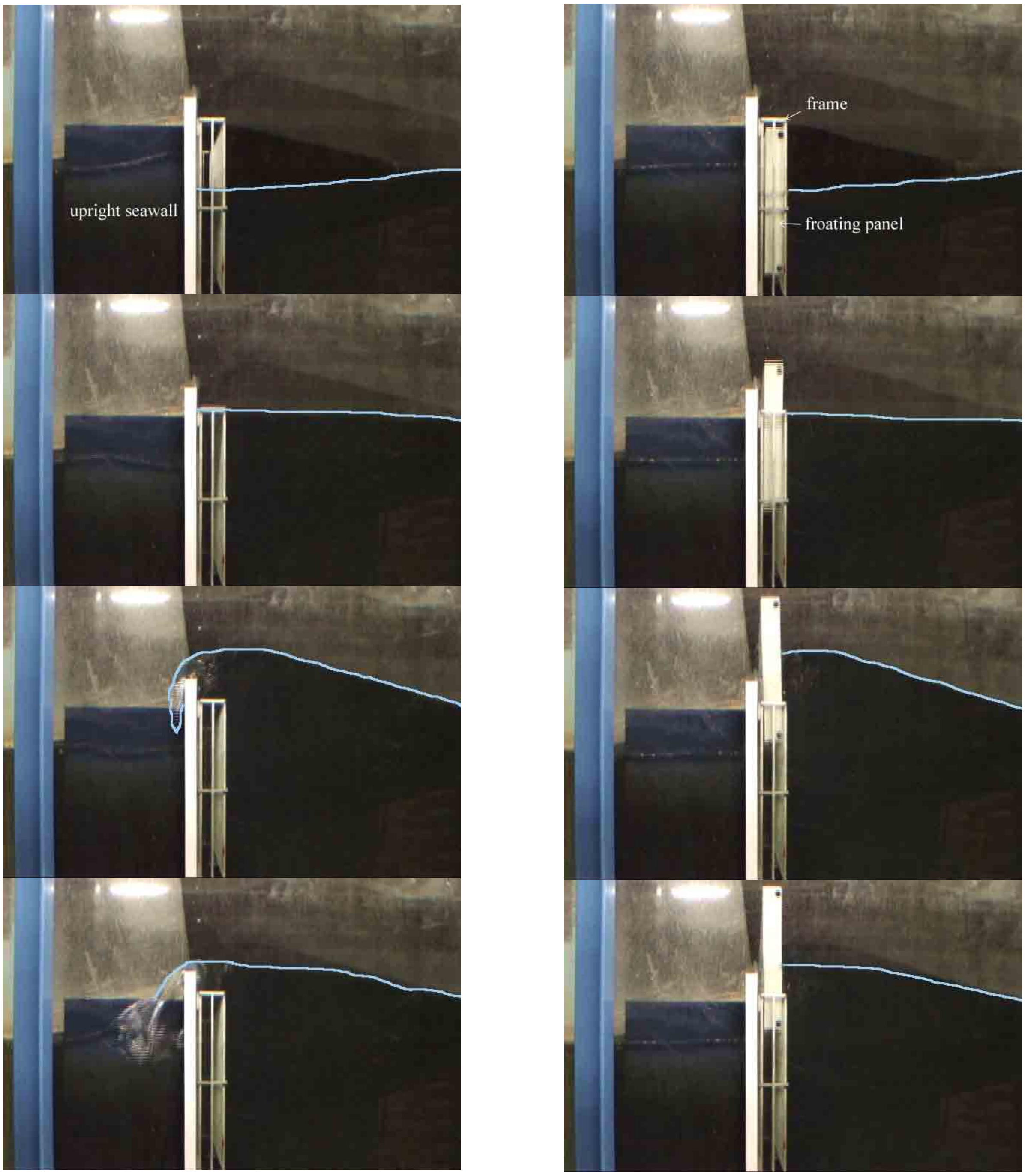

(a) Without floating panel

(b) With floating panel

Figure **3.6** Wave overtopping performances on upright seawall without and with floating panel

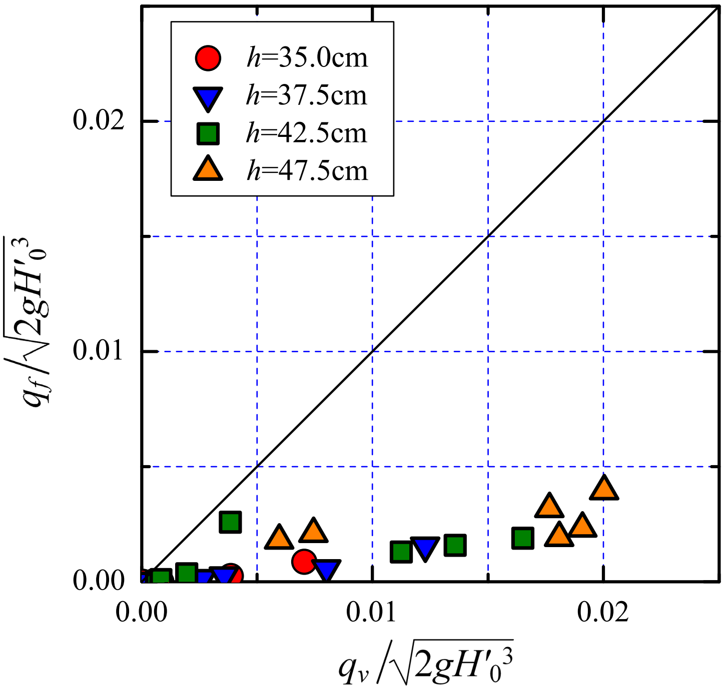

Figure **3.7** Comparison of dimensionless wave overtopping rate of upright seawall and upright seawall with floating panel

one. It is, then, found from the third and fourth photos that the wave crest in front of the seawall is much higher than the crown height of the seawall, resulting in the occurrence of wave overtopping and a strong splash behind the seawall. On the other hand, as shown in Fig. **3.6**(b) for the case of the seawall with the floating panel, the floating panel is found to follow water surface elevation and prevent wave overtopping. The comparison between Figs.**3.6**(a) and (b), as a result, reveals a great reduction effect of the floating panel on wave overtopping.

Fig.**3.7** depicts the relation between dimensionless wave overtopping rate $q/\sqrt{2gH_0'^3}$ of the upright seawall and that of the upright seawall with the floating panel, where q, g and H_0' are respectively wave overtopping rate, gravity acceleration and equivalent deepwater wave height. It is found from the figure that within range of both small and large wave overtopping scale, an average wave overtopping reduction rate R accounts for approximately 89% for water depths of h=35.0cm, 37.5cm and 42.5cm, and about 84% for water depth of h=47.5cm. A great reduction of wave overtopping rate of the upright seawall with the floating panel is therefore confirmed for not only small wave overtopping but also large wave overtopping.

(a) Water mass overtops floating panel, Type 1

(b) Water mass flows through the gap between upright seawall and floating panel, Type 2

Figure **3.8** Wave overtopping characteristic

(2) Characteristics of Wave Overtopping

For an upright seawall with a floating panel, two kinds of wave overtopping types (Type 1 and Type 2) were observed in the laboratory experiments, as shown in Figs.**3.8**(a) and (b). The respective wave overtopping features of Type 1 and Type 2 are as follows; Type 1 is that water mass overtops the crowns of the floating panel and the seawall, as shown in Fig.**3.8**(a). Type 2 indicates that water flows into the behind of the seawall through the gap between the upright seawall and the floating panel. For Type 2, wave overtopping rate could be additionally reduced by setting certain measures filling the gap. In terms of Type 1, wave overtopping occurs because the floating panel is not able to follow the water surface elevation in front of the seawall. Therefore, a relationship between the dynamic behaviors of a floating panel and water surface elevation is of importance to be further examined.

(3) Dynamic Behavior of Floating Panel under Wave Action

It was revealed from the laboratory experiment that basic characteristics of dynamic behavior of floating panel were influenced by the relation of wave period to natural period of floating panel in vertical direction. Therefore, only wave condition of H=10cm was shown here for discussion. Full data can be found in Funahashi (2011).

Figures **3.9** ~ **3.12** show the time variation of floating panel motion and water surface elevation for the condition of water depth h=42.5cm and wave height H=10cm at different wave periods, in which (a) is the snapshots of floating panel motion captured by the high-speed camera, and (b) depicts the relation between floating panel motion and water surface elevation. For wave periods of T=1.79s and T=1.34s (Figs.**3.9** and **3.10**), wave overtopping does not occur

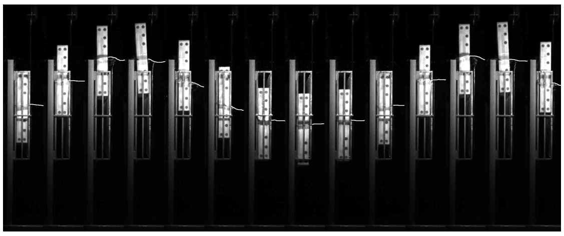

(a) Continuous photographs around floating panel (0.2s per frame)

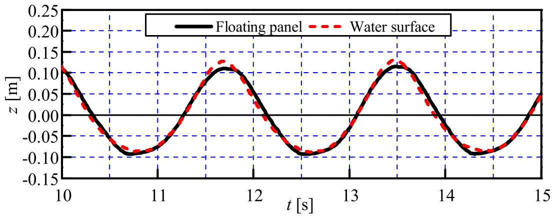

(b) Temporal variation of floating panel motion and water surface elevation

Figure **3.9** Floating panel motion and water surface elevation (H = 10cm, T = 1.79s)

(a) Continuous photographs around floating panel (0.2s per frame)

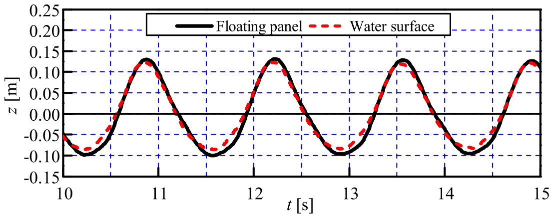

(b) Temporal variation of floating panel motion and water surface elevation

Figure **3.10** Floating panel motion and water surface elevation (H = 10cm, T = 1.34s)

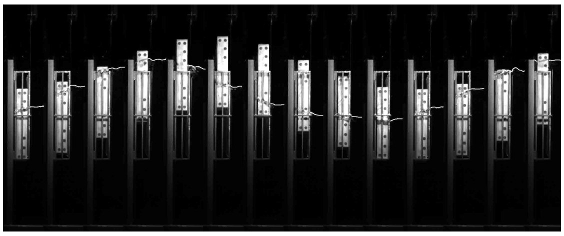

(a) Continuous photographs around floating panel (0.2s per frame)

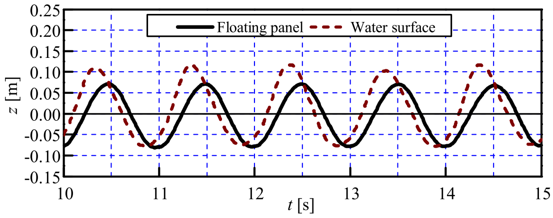

(b) Temporal variation of floating panel motion and water surface elevation

Figure **3.11** Floating panel motion and water surface elevation (H = 10cm, T = 1.00s)

(a) Continuous photographs around floating panel (0.2s per frame)

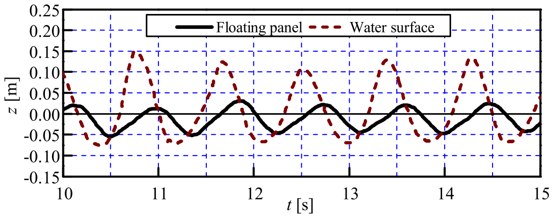

(b) Temporal variation of floating panel motion and water surface elevation

Figure **3.12** Floating panel motion and water surface elevation (H = 10cm, T = 0.85s)

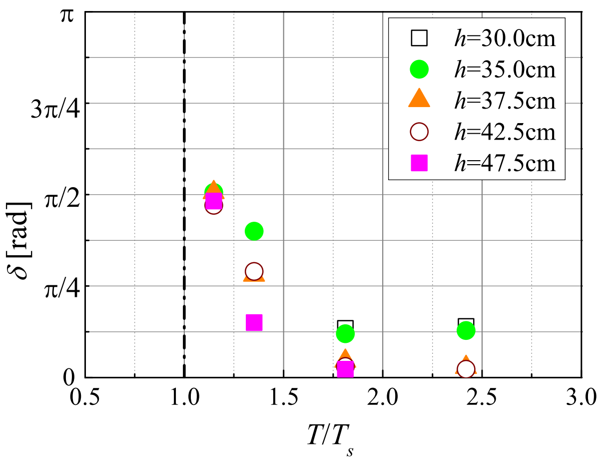

Figure **3.13** Relation between the phase lag and ratio of incident wave period and the natural period

since the floating panel follows in the same phase with water surface elevation. For wave periods of T=1.00s and T=0.85s (Figs.**3.11** and **3.12**), although the floating panel behaves in the similar way to the water surface elevation, a phase lag between them is clearly seen. Additionally, the amplitude of the floating panel motion becomes smaller than that of the water surface elevation. As a result, it is found that wave overtopping of Type 1 takes place, as shown in Fig.**3.12**(a), in the case of wave period of T=0.85s. It is also found from a comparison among Figs. **3.9** ~ **3.12** that a phase lag becomes larger as the wave period is getting smaller and smaller. Judging from the above-mentioned observations, the motion characteristics of the floating panel can be said to be strongly influenced by wave period. A collision between the floating panel and the steel frame, which was observed in the experiment, might be related to this relationship.

A relation of natural period of a floating panel to incident wave period is assumed as one of the causes of the phase lag. A phase lag δ[rad] is defined as the difference between the peak times t and t_s of water surface elevation and floating panel motion, as indicated in Eq.(3.2).

$$\delta = \frac{2\pi\,(t_s - t)}{T}[\text{rad}] \tag{3.2}$$

Fig.**3.13** shows the relationship between the phase lag δ and dimensionless wave period T/T_s, where T_s = 0.74s is the natural period of floating panel motion in a vertical direction. As shown in Fig. **3.13**, the phase lag increases when T/T_s is close to 1. In other words, if wave period is close to the natural period of a floating panel, the response of the floating panel motion in the vertical direction induces a large phase lag. Therefore, the natural period of floating panel should be a key parameter in designing the configurations for floating panel.

3.2.3 Remarks

The laboratory experiment is discussed in this section. Main conclusions and concerned problems in numerical studies are stated as follows;

A great effect of the floating panel on wave overtopping reduction under regular wave action was revealed. On the other hand, wave overtopping characteristics of the countermeasure were classified into two kinds of Type 1 and Type 2 in the laboratory experiment. Type 1 is that water mass overtops the crown height of the floating panel and the seawall. Type 2 represents that water flows into the behind of the seawall through the gap between the seawall and the floating panel. The relation of temporal variation of water surface elevation in front of the seawall to that of floating panel motion in the vertical direction as well as wave overtopping characteristics are, therefore, very important to be discussed in details.

On the other hand, the phase lag between floating panel motion in the vertical direction and water surface elevation in front of the seawall was found to increase as incident wave period was close to the natural period of a floating panel in the vertical direction. The collision between the floating panel and the steel frame seen in the laboratory experiment might be related this relation. The above-mentioned characteristics should be furthermore investigated numerically.

3.3 Numerical Study

In this section, first, equation of floating panel motion is developed, in which the impact of the steel frame on the motion of the floating panel is taken into account through a damping term, in order to realize the dynamic behavior of the floating panel under wave action. The proposed model are then used to investigate the nonlinear interaction of wave and floating panel. The numerical results are moreover verified through the comparison with the experimental ones in terms of dynamic behavior of floating panel under wave action, variation of water surface elevation and pressure acting on the bottom the floating panel.

3.3.1 Equation of Floating Panel Motion

In the laboratory experiment, it was seen that the motion of the floating panel under wave action sometimes induces a collision between the steel frame and floating panel. Due to the collision, the friction between the floating panel and the steel frame was observed when the floating panel moved in the vertical direction. This force is assumed to influence the dynamic behavior of the floating panel in the vertical direction. The motion equation of the floating panel is, therefore, proposed by adding a damping term to the equation of the motion in the vertical direction.

On the other hand, it was found from the laboratory experiment that the vertical motion of the floating panel was dominant compared with rotational motion and horizontal motion. Two latter motions are therefore neglected in this study.

Under the above-mentioned assumption, the motion equation of the floating panel in the vertical direction is denoted as follows,

$$M_l \frac{d\overline{w_l}^{n+1}}{dt} + c\overline{w_l}^{n+1} = F^* \tag{3.3}$$

where, M_l represents the total mass of the floating panel, which is denoted in Eq.(2.129); c represents a damping coefficient and is determined by trial and error; F^* represents the hydrodynamic force term at the present step, which is calculated by Eqs.(2.131) ; $\overline{w_l}^{n+1}$ and $d\overline{w_l}^{n+1}/dt$ respectively represent the velocity and the acceleration of the gravity center of the floating panel motion at the next time step. In order to solve the developed equation of motion Eq.(3.3), the Newmark-β method is utilized to determine the relation of the velocity at the next time step $\overline{w_l}^{n+1}$ to the velocity at the present time step $\overline{w_l}^{n}$ as follows,

$$\overline{w_l}^{n+1} = \overline{w_l}^{n} + \left(\frac{d\overline{w_l}^{n}}{dt} + \frac{d\overline{w_l}^{n+1}}{dt} \right) \frac{\Delta t}{2} \tag{3.4}$$

By substituting of $\overline{w_l}^{n+1}$ in Eq.(3.4) into Eq.(3.3), the acceleration at next time step is obtained in Eq.(3.5),

$$\frac{d\overline{w_l}^{n+1}}{dt} = \frac{-c\left(\overline{w_l}^{n} + \frac{d\overline{w_l}^{n}}{dt}\frac{\Delta t}{2}\right) + F^*}{M_l + c\frac{\Delta t}{2}} \tag{3.5}$$

Once the acceleration at next time step is determined, the velocity at next time step is calculated by using Eq.(3.4).

3.3.2 Computational Domain

A computational program based on multiphase flow model with solid-gas-liquid interaction, which is referred to as DOLPHIN-3D (Dynamic numerical model Of muLti-Phase flow with Hydrodynamic INteractions - 3-Dimension), was used to simulate the nonlinear interaction between wave and floating panel. Fig. **3.14** shows a definition sketch of the computational domain used in numerical simulations. The computation domain includes an energy dissipation zone on the left and a wave overtopping pit on the right. The origin of x coincides with the wave generation source, and the positive direction of x is taken toward the right hand side of

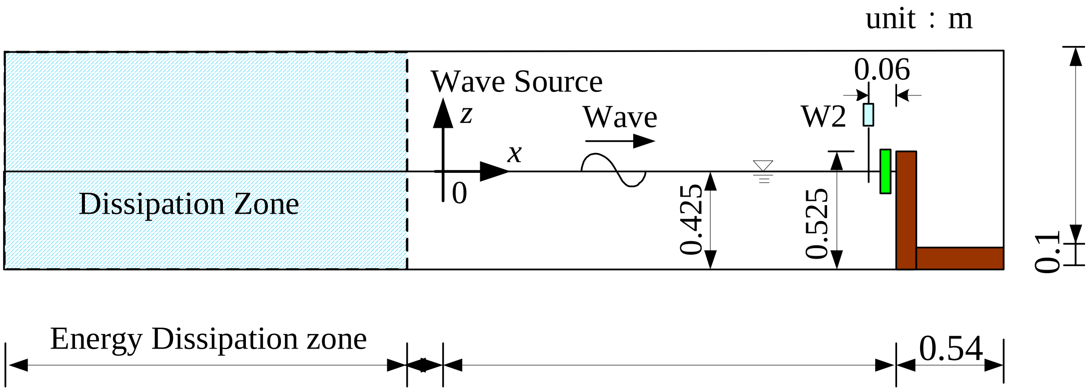

Figure **3.14** Computational Domain

the computational domain. The location of the wave generation source was set at near the left side of the analysis zone. A wave gauge is installed in front of the seawall in order to measure water surface elevation. Mesh size in the direction of x, $\Delta x_i/L$ and mesh size in the direction of z, $\Delta z_k/h$ are varied in a range of 1/200~1/100 and 1/40~1/25 (L_i: the wave length; h: the water depth), respectively. The mesh sizes in the possible motion space of the floating panel, are set equal to 0.005m in order to capture the surface of the floating panel with high accuracy. The time interval at every time step was set at $\Delta t/1000$ so that the Courant condition is always satisfied.

3.3.3 Variation of Floating Panel Motion and Water Surface Elevation

In order to investigate dynamic motion characteristic of floating panel under wave action, the relation of floating panel to water surface elevation in front of the panel is discussed in this section.

Fig.**3.15** shows the temporal variation of water surface elevation in front of the seawall and floating panel motion within a wave cycle for the condition of h=42.5cm, H=0.04m and T=2.24s. As shown in Fig.**3.15**, from t=14.00s ~ 14.60s, the floating panel goes up when the water surface rises. Furthermore, it is found that the floating panel starts moving upward from the initial position at t=14.00s and reaches near the peak location at the t=14.60s. From the figures of t=14.60s~15.80s, the floating panel moves downward when the water surface falls. Interestingly, both the floating panel and the water surface elevation reach near the lowest location at around t=15.80s. After that, from t=15.80s to 16.10s, the floating panel moves upward and reach near the initial position at t=16.10s. As a result, it is revealed that the floating panel takes a periodic motion within a wave cycles by following the water surface elevation in front of the panel, as seen in the laboratory experiment.

Fig.**3.16** shows the temporal variation of water surface elevation in front of the seawall and floating panel motion within a wave cycle for the same above condition except another wave period T=1.0s. In the Fig.**3.16**, it is also seen that the floating panel follows the water surface elevation in front of the seawall, but a difference in the phase of water surface elevation and floating panel motion is observed. From t=12.30s ~ 12.60s, floating panel goes up when water surface rises, and the water surface reaches near the peak level at t=12.60s. The floating panel motion, however, shows a delay in reaching the peak position compared with water surface elevation. Furthermore, a larger difference in the phase between water surface elevation and the floating panel motion is clearly seen in Fig.**3.17** for the same condition of water depth and wave height as the above conditions except wave period T=0.75s. Note that the wave periods for the two latter condition are T=1.00s and T=0.75s, which are very close to the natural period of floating panel T_S=0.74s, it is revealed that if wave period is close to the natural period of the floating panel, the floating panel motion in vertical direction experiences a large phase lag, as shown in the laboratory experiment. It is also confirmed that the proposed model is capable of reproducing the dynamic behavior of a floating panel under wave action.

3.3.4 Wave Overtopping Reduction Effects

Wave overtopping characteristics are very important for discussing wave overtopping reduction effect of the proposed countermeasure. This section, therefore, examines wave overtopping characteristic through images depicting wave overtopping situation around the seawall with and without floating panel, based on the numerical results.

Figures **3.18**(a) and (b) show the wave overtopping situation around the seawall without the floating panel and with the floating panel for the wave condition of h=42.5cm, H=0.10m and T=2.24s, respectively. In the figures from t=14.10s~14.30s of Fig.**3.18**(a), it is seen that water surface rises in the front of the panel. Then, from t=14.50s~14.70s, the wave crest in front of the seawall is observed higher than the crow height of the seawall, resulting in the occurrence of wave overtopping on the seawall.

On the other hand, as shown in Fig.**3.18**(b), although the occurrence of wave overtopping is also found from t=14.50s~14.70s, the wave overtopping characteristic is found different from wave ovetopping characteristics in the case of the seawall without floating panel because the water overflows into top of the seawall through the gap between the seawall and the floating panel. It might be explained that the floating panel follows the water surface elevation and

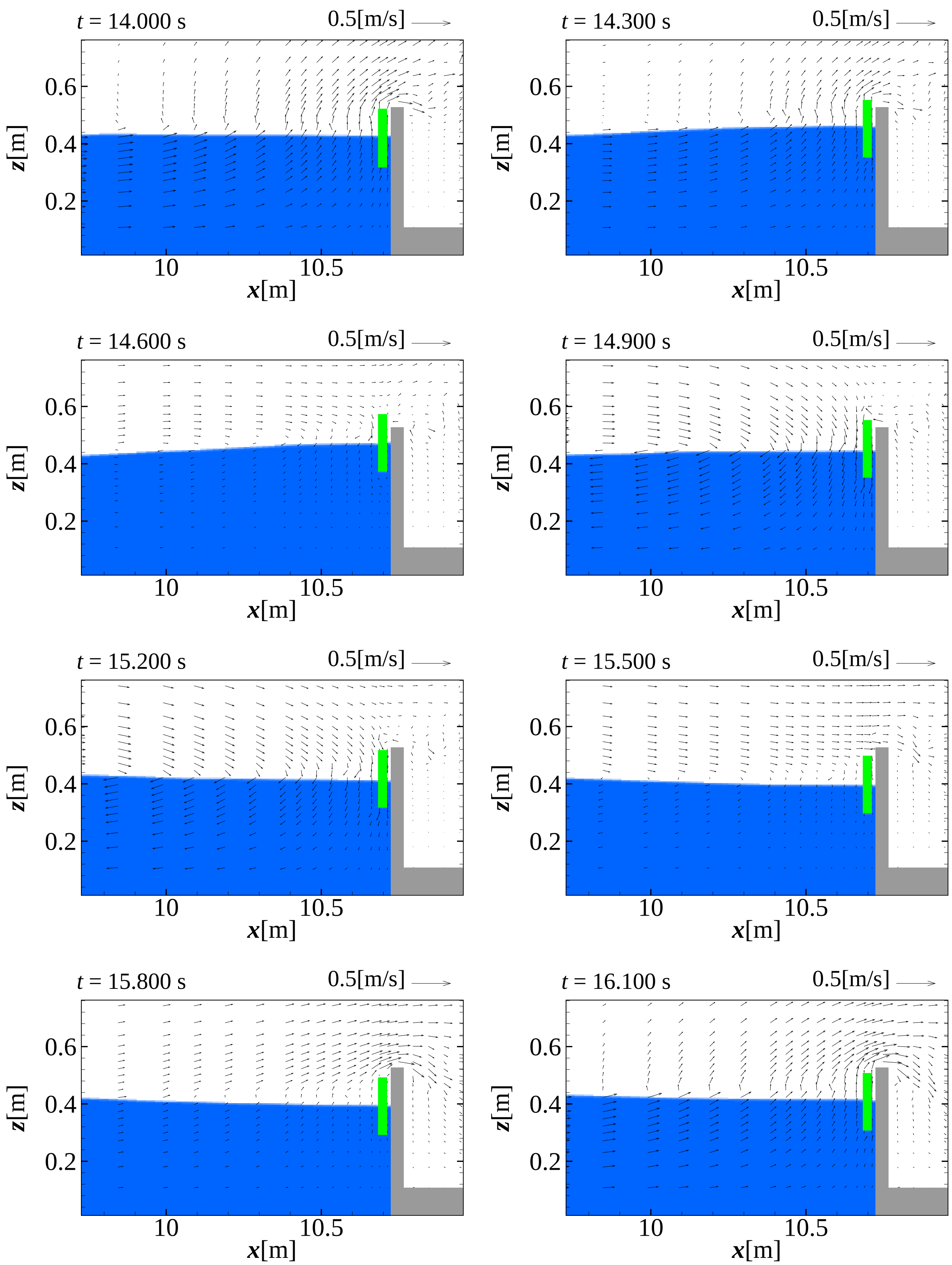

Figure **3.15** Variation of floating panel motion and water surface elevation (h=0.425m,H=0.04m,T=2.24s)

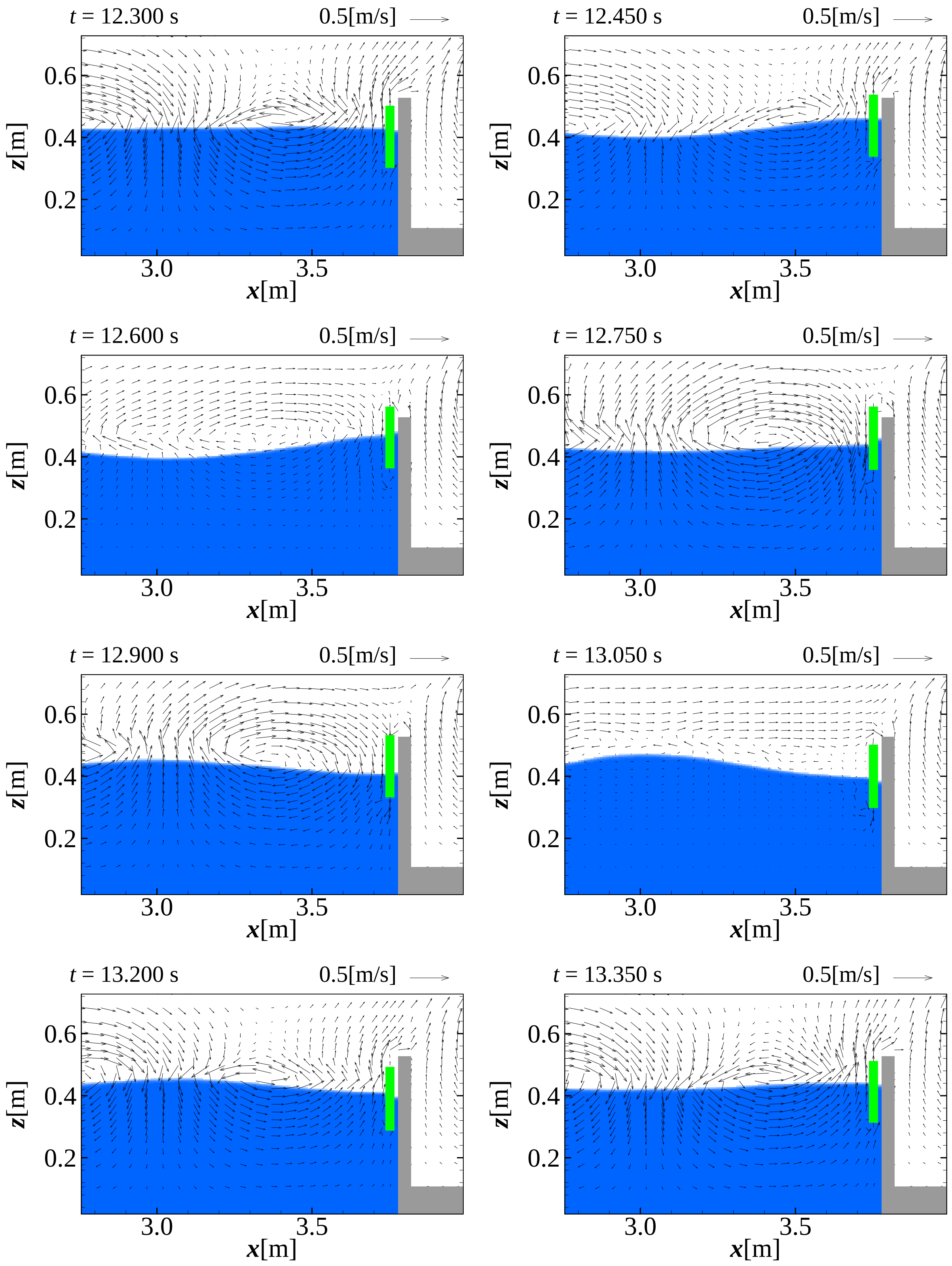

Figure **3.16** Variation of floating panel motion and water surface elevation (h=0.425m,H=0.04m,T=1.00s)

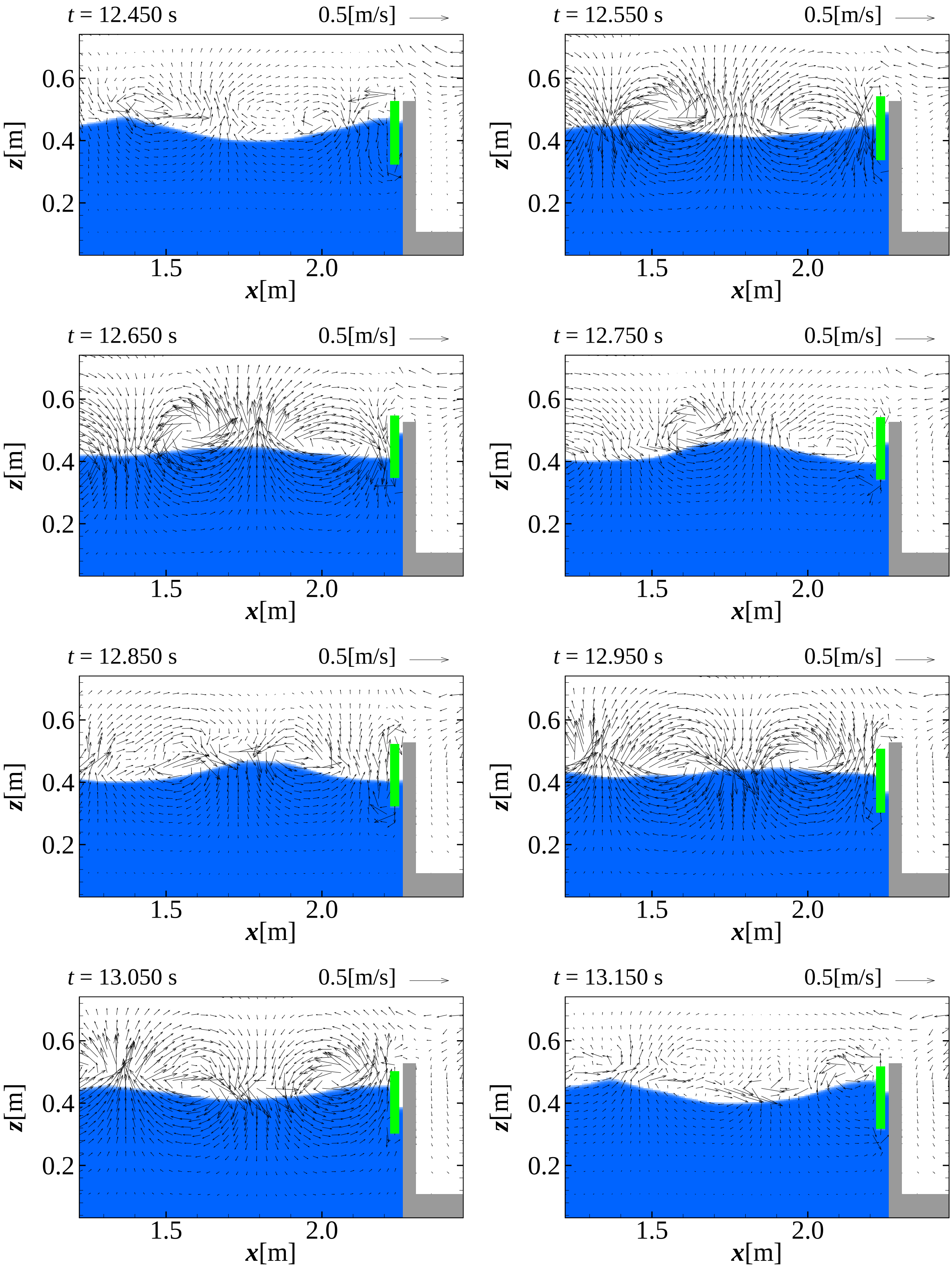

Figure **3.17** Variation of floating panel motion and water surface elevation (h=0.425m,H=0.04m,T=0.75s)

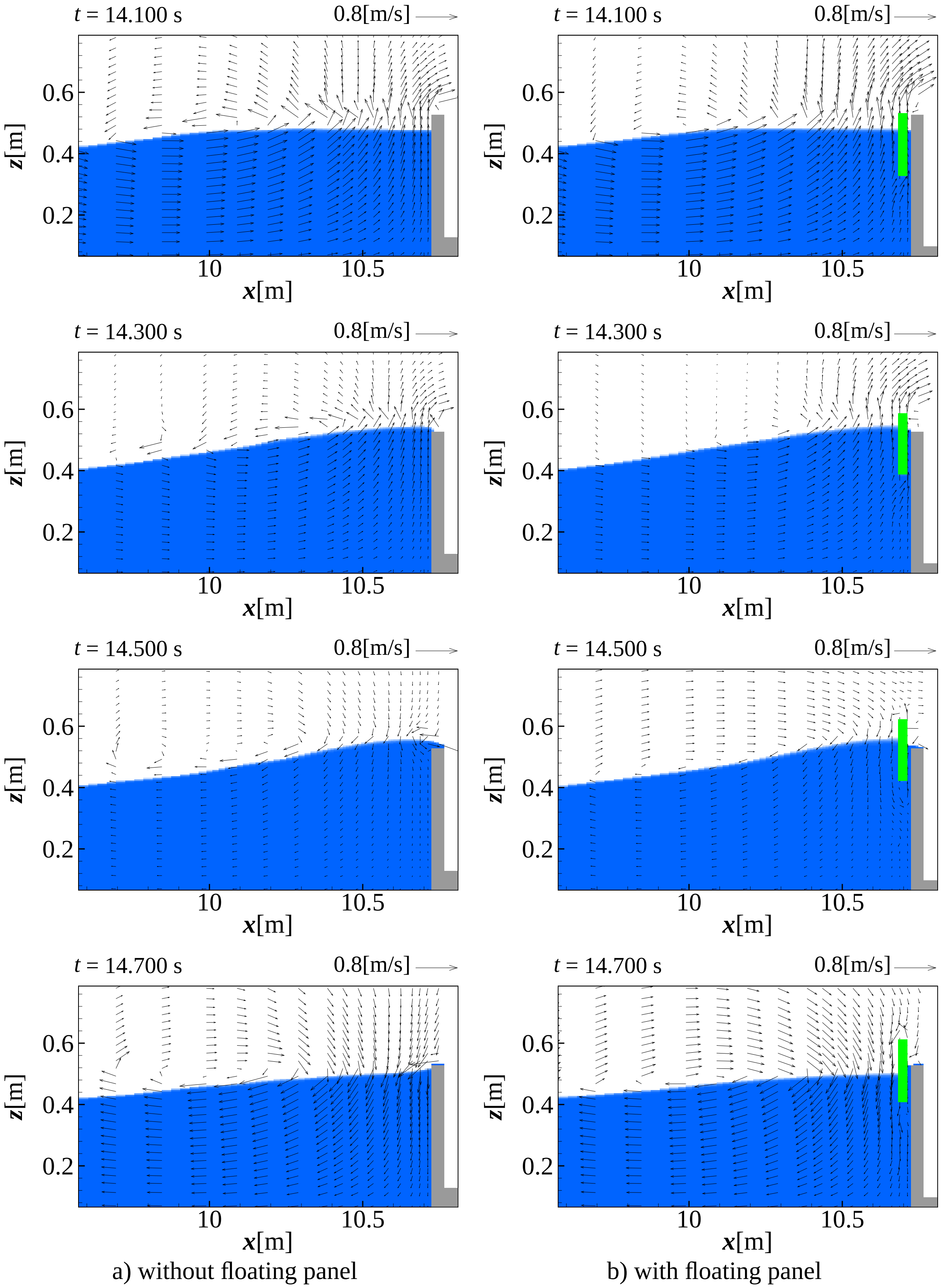

a) without floating panel b) with floating panel

Figure **3.18** Wave overtopping on the seawall without and with floating panel (h=0.425m,H=0.10m,T=2.24s)

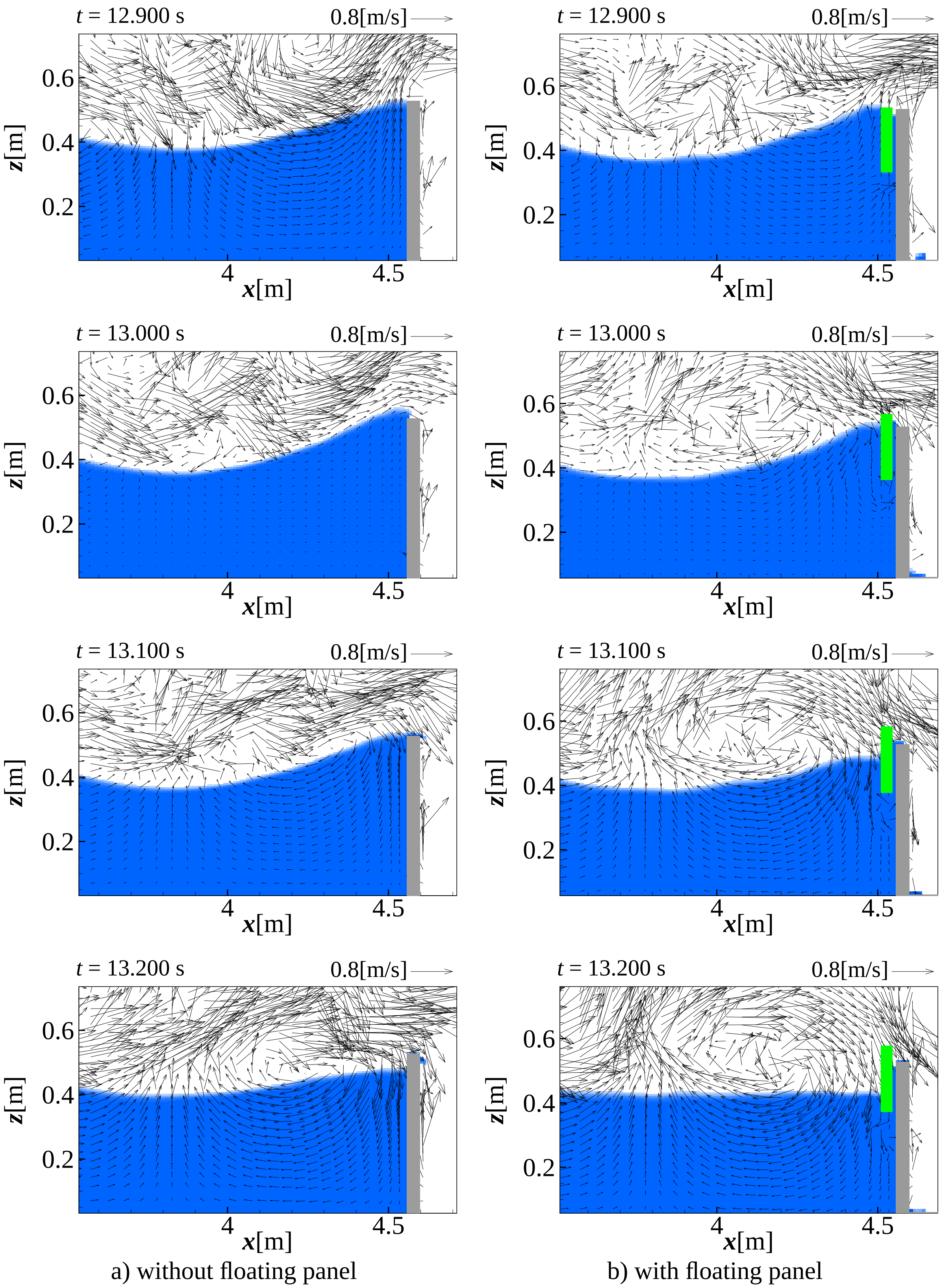

a) without floating panel b) with floating panel

Figure **3.19** Wave overtopping on the seawall without and with floating panel (h=0.425m,H=0.10m,T=1.00s) therefore prevents wave overtopping the crown height of the seawall as seen in Fig.**3.18**(a). The difference of wave overtopping characteristics around the seawall with and without floating panel are also seen in Figs. **3.19** (a) and (b). Therefore, it would be said that the floating panel has a reduction effect of wave overtopping under regular wave action by following the water surface elevation in front of the seawall. However, further measures filling the gap between the panel and the seawall should be set for the overflow from the gap.

3.3.5 Temporal Variation of Pressure Acting on the Side of the Floating Panel

It is known that the calculation of forces acting on a structure is very important in the designing stage. For a movable structure under wave actions such as floating panel, the complex-nonlinear interaction between wave and the structure results in many difficulties for this task. The pressure data acting on the floating panel obtained from the laboratory experiment, therefore, are very valuable. Unfortunately, only data of the pressure acting on the bottom of the panel was achieved in the laboratory experiment, the data of the pressure acting on the sides of the floating panel have not been available because the installation of the pressure gauges on the side of the floating panel is impossible due to possible damaged resulting from the collision impact between the steel frame and floating panel if these gauges are installed. The numerical analysis, hopefully, can overcome this problem by simple installation of pressure gauges in the numerical tests.

Fig.**3.20** shows the pressure distribution on the side of the floating panel under wave condition of water depth h=0.425m, wave height H=0.10m, and wave period T=2.24s. In the Fig.**3.20**, it is found that the pressure varies when the floating panel moves under wave action. A reduction of the draft of the floating panel causes the decrease of the pressure acting on the side of the floating panel, whereas the increase of the pressure results from the increase of the draft of the floating panel. The difference of pressure acting on the front side of the panel and that on the back side of floating panel is found very small within a wave cycle with a only largest difference of 172Pa at t=17.25s. Additionally, the numerical measurements of the pressures at lowest elevation on the sides of the floating panel at different stages revealed that the values of these pressures are approximate the hydrostatic pressures acting at the same positions of the floating panel. For example, at t=16.35s, the draft of the floating panel is 0.15m, meaning that the hydrostatic pressure at the bottom of floating panel is 1500Pa, the pressure at the lowest elevation in the front of the panel is found equal to 1490Pa. At t=17.85s, the floating panel experiences a draft of 0.12m, meaning that the hydrostatic pressure is 1200Pa, a value of 1180Pa is found for the pressure at the same position. Consequently, it is revealed that the distribution

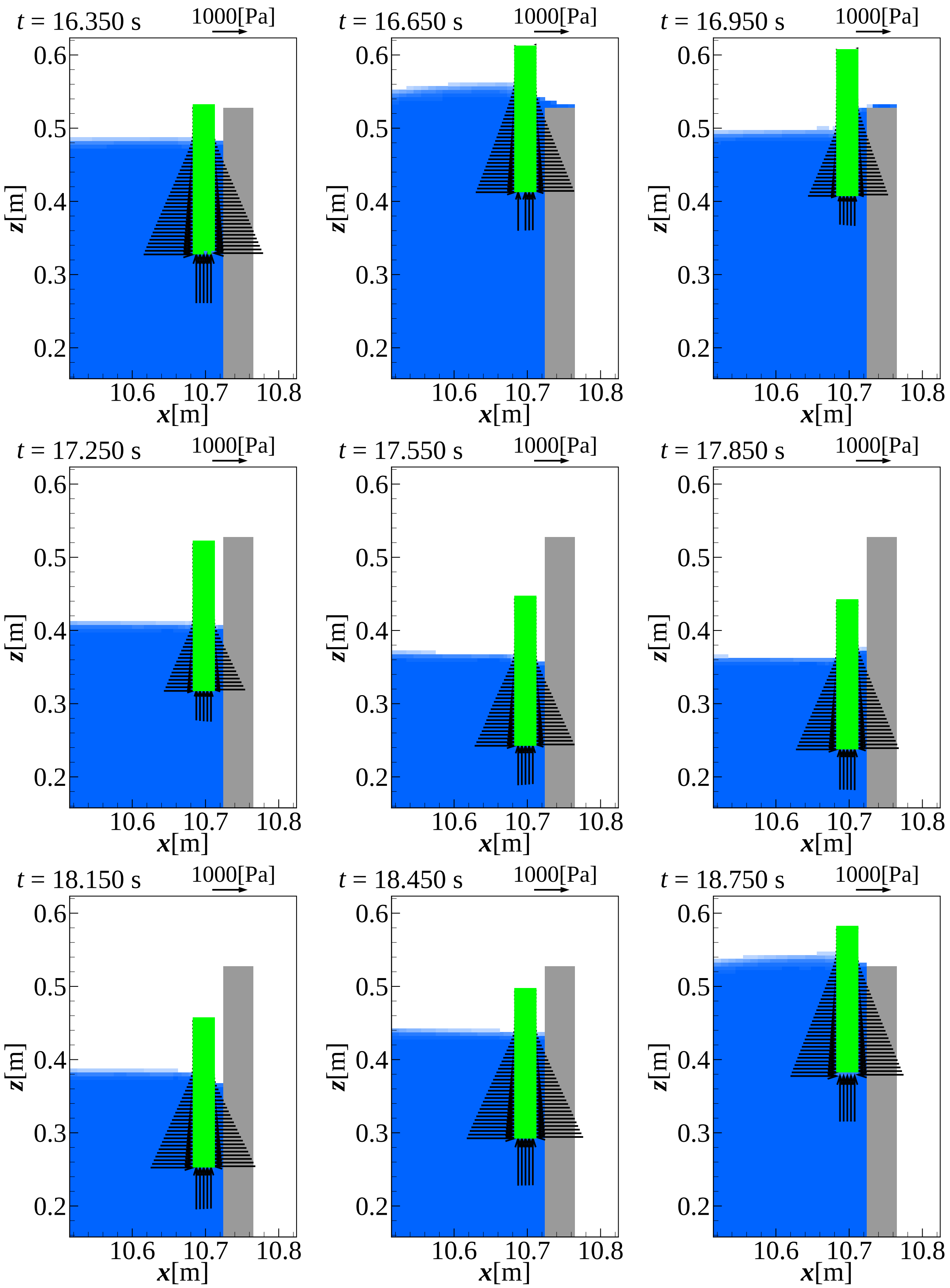

Figure **3.20** Temporal variation of pressure acting on the floating panel(h=0.425m,H=0.10m,T=2.24s)

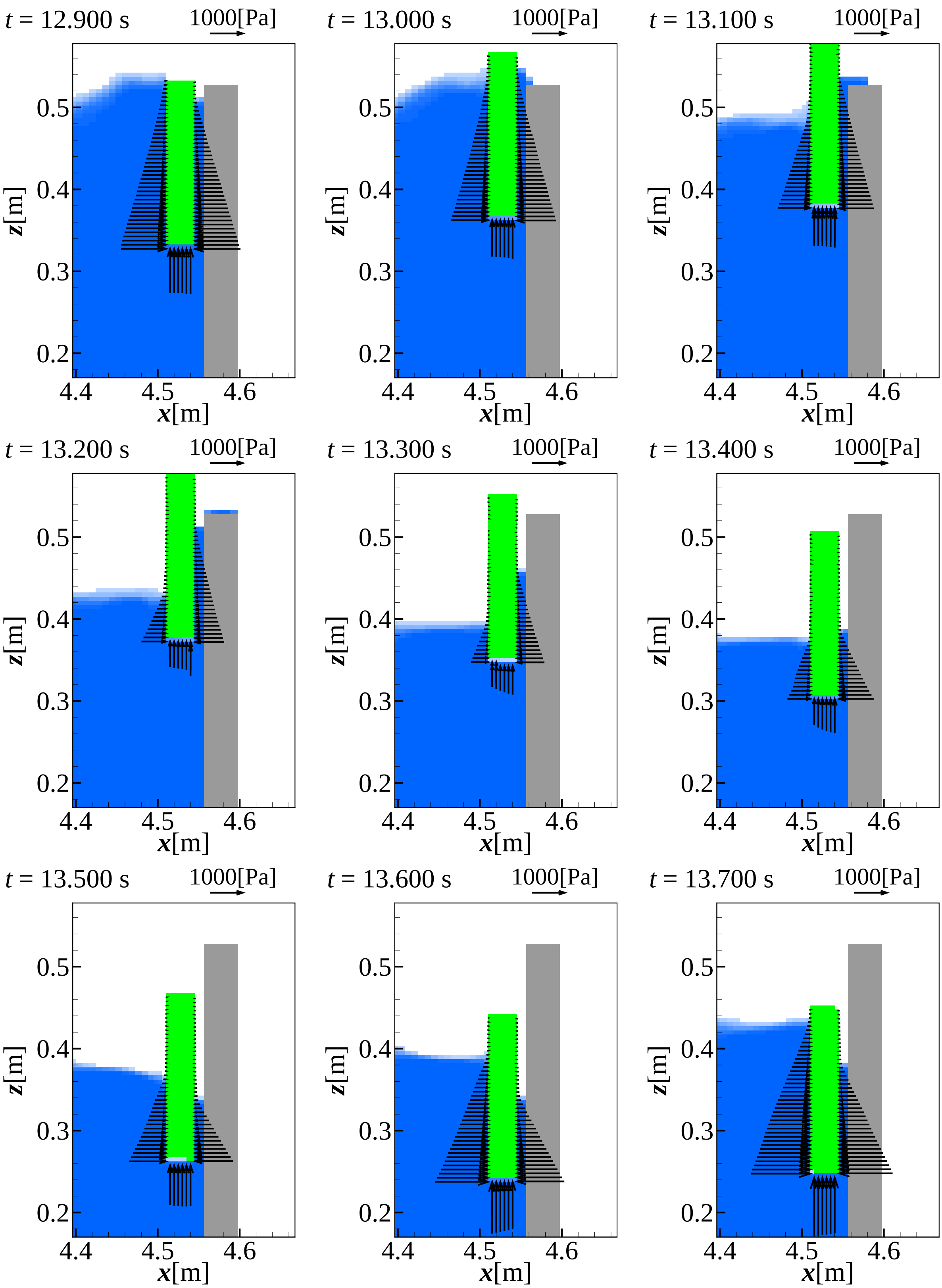

Figure **3.21** Temporal variation of pressure acting on the floating panel(h=0.425m,H=0.10m,T=1.00s) of the pressure acting on the sides of the floating panel is as the same as hydrostatic pressure distribution.

On the other hand, Fig.**3.21** shows the pressure the pressure distribution on the sides of the floating panel under wave conditions of water depth and wave height same as the above wave condition, except wave period T=1.00s. Although a variation of pressure with the draft of the floating panel is also shown in Fig.**3.21**, the distribution of the pressure acting on the sides of the floating panel is found not the same as the distribution of the hydrostatic pressure, as shown in Fig.**3.20**. Furthermore, the difference between the pressure acting on the front side and the back side of the floating panel is found quite large compared with the maximum hydrodynamic pressure acting on the bottom of the floating panel at almost stages within a wave cycle. For instance, at t=13.20s, this difference is 490Pa, taking about 60% of the maximum pressure, which is equal to 800Pa, whereas only 172Pa of the maximum difference is seen in Fig.**3.20**. Note that the wave period of T=1.00s for this condition is very close to the natural period of the floating panel in the vertical direction, meaning that the large difference of phase lag between the water surface elevation and the floating panel motion occurs. As a result, the water surface elevation at the front side of the panel can be very difference that at the back side of the floating panel. The above-mentioned difference of the pressure acting on the front side and the back side of the floating panel is, therefore explained.

It might be questioned that if the values of the pressure acting on the sides of the floating panel are always found smaller than maximum hydrostatic pressure acting on the bottom of the floating panel, whether or not the above-mentioned investigation of the pressure acting on the sides of floating panel is worth. For structural designers, however, the unique answer is that the above-mentioned revelation of the difference of the pressures acting on the sides of floating panel is very valuable because it is found from this revelation that the floating panel is subjected to not only equal compression resulting from the pressure acting on the both sides as in normal thoughts, but also bending caused by the difference between pressure acting on the front side of the floating panel and that on the back side, which are sometimes required a strengthen beyond the compression strength requirement. The validity and utility of the numerical investigation, therefore, are confirmed.

3.3.6 Verification of Numerical Results

(1) Temporal Variation of Water Surface Elevation in Font of the Seawall

In order to understand the interaction of water surface and the seawall, the temporal variation of water surface elevation in front of the seawall needs to be examined. Figures **3.22**(a)~**3.22**(c) show temporal variation of calculated water surface elevations in front of the seawall and measured ones for wave conditions of water depth h=0.425m, wave height H=0.04m, and wave periods of T=2.24s, 1.00s and 0.75s, respectively. It is revealed from Figs.**3.22**(a)~**3.22**(c) that incident waves are near fully reflected because the standing wave ratios H_{st}/H (H_{st}: standing wave height; H: incident wave height) are close to 2. For the wave condition with wave period T=2.24s, standing wave ratio is found to be approximately 1.876 for both calculated and measured results, whereas a value of 1.74 is obtained the wave condition with wave period T=1.00s. Good agreements between the calculated and measured results are further seen from these figures.

Figures **3.22**(d) and **3.22**(e) show temporal variation of calculated and measured water surface elevations in front of the seawall for wave conditions of h=0.425m, H=0.10m, and wave periods of T=2.24s and 1.00s, respectively. In Figs.**3.22**(d) and **3.22**(e), good agreements between the calculated and measured ones are also confirmed, except that the peak values of the calculated results slightly overestimate compared with the measured results at some stages. Consequently, the numerical model can said to be capable of reproducing the nonlinear interaction of waves and structures in the laboratory experiments.

(2) Dynamic Behavior of Floating Panel under Wave Actions

Numerical analyses of dynamic behavior of floating panel under wave action are presented in this section. First, the calculated results of floating panel motion based on the developed equation of motion are compared with measured ones in order to investigate the validity of the developed equation of floating panel motion. Furthermore, the relation of the ratio of wave period and the natural period to the amplitude of floating panel motion as well as phase lag between water surface elevation and floating panel motion are discussed.

Figures **3.23**(a)~**3.23**(c) show temporal variations of calculated floating panel motion results and measured ones for wave conditions of h=0.425m, H=0.04m, and wave periods of T=2.24s, 1.00s and 0.75s, respectively. In Figs.**3.23**(a)~**3.23**(c), it is shown that the calculated floating panel motion results are in good agreement with the measured ones. Good agreements between calculated floating panel motion results and measured ones are also found in Figs.**3.23**(d) and **3.23**(e), which depict temporal variations of calculated and measured floating panel motion results for wave conditions of h=0.425m, H=0.10m, and wave periods of T=2.24s and 1.00s, respectively. It is seen from Fig.**3.23**(d) that the calculated results slightly underestimate the peaks compared with the measured ones at some stages. Furthermore, in Figs.**3.23**(a)~**3.23**(e), it is revealed that for the same water depth and wave height, the amplitude of floating panel motion trends to decrease when wave period is close to the natural period of the floating panel.

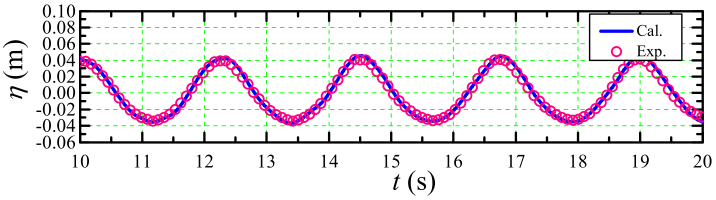

(a) h=0.425m,H=0.04m,T=2.24s

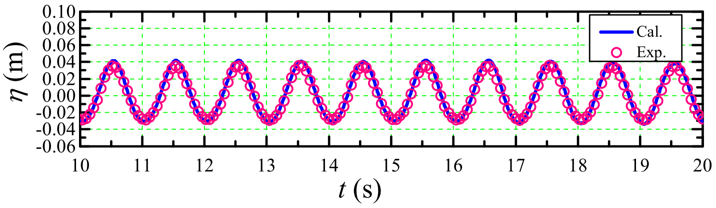

(b) h=0.425m,H=0.04m,T=1.00s

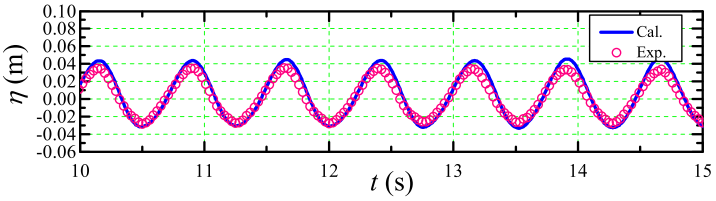

(c) h=0.425m,H=0.04m,T=0.75s

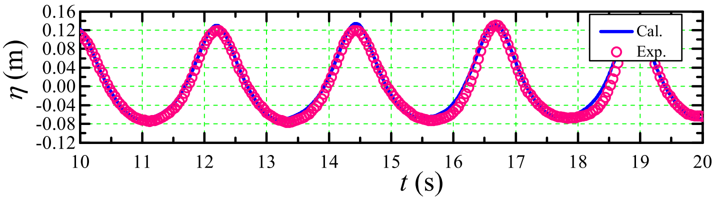

(d) h=0.425m,H=0.10m,T=2.24s

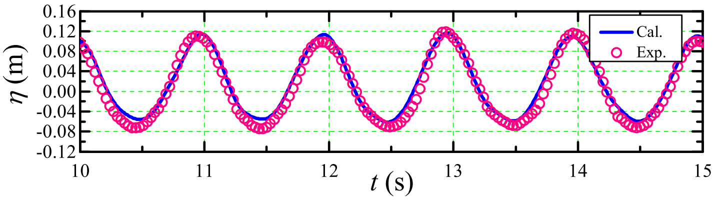

(e) h=0.425m,H=0.10m,T=1.00s

Figure **3.22** Temporal variation of water surface elevation

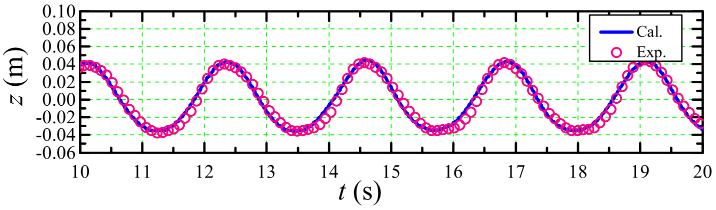

(a) h=0.425m,H=0.04m,T=2.24s

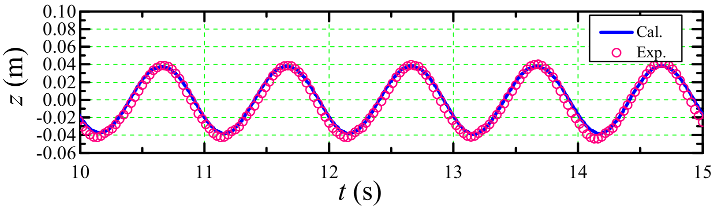

(b) h=0.425m,H=0.04m,T=1.00s

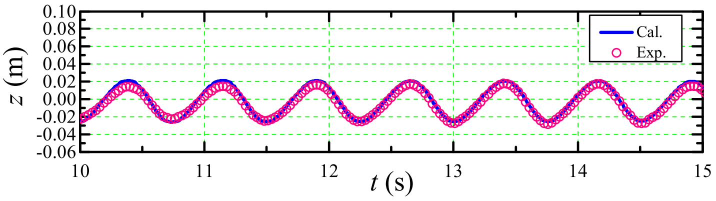

(c) h=0.425m,H=0.04m,T=0.75s

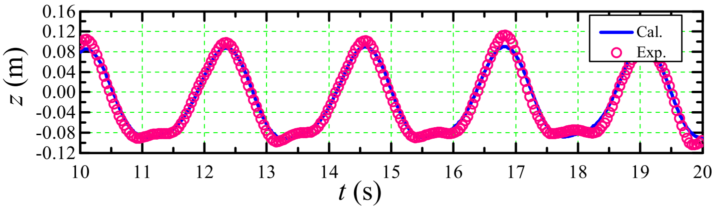

(d) h=0.425m,H=0.10m,T=2.24s

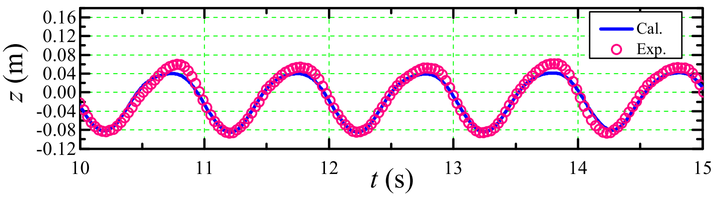

(e) h=0.425m,H=0.10m,T=1.00s

Figure **3.23** Temporal variation of floating panel motion

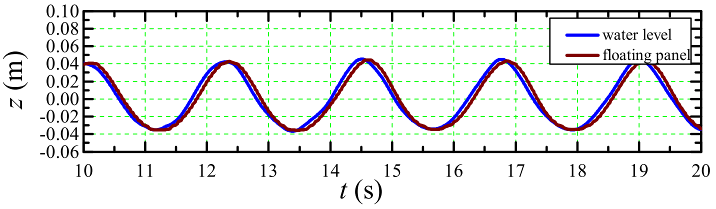

(a) h=0.425m,H=0.04m,T=2.24s

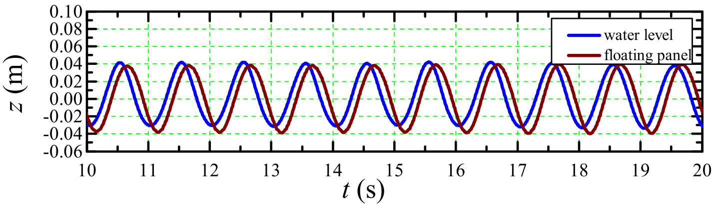

(b) h=0.425m,H=0.04m,T=1.00s

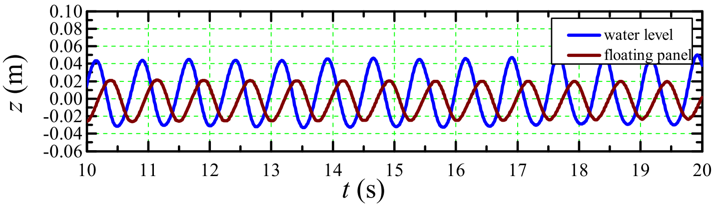

(c) h=0.425m,H=0.04m,T=0.75s

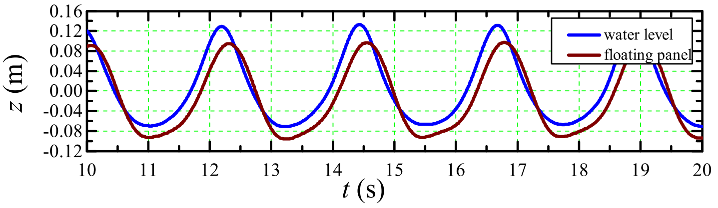

(d) h=0.425m,H=0.10m,T=2.24s

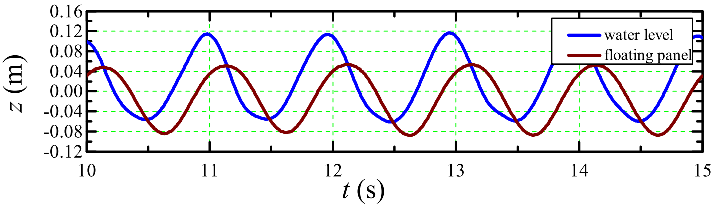

(e) h=0.425m,H=0.10m,T=1.00s

Figure **3.24** Variation of water surface elevation and floating panel motion

Taking an examination on the temporal variations of the water surface elevation and floating panel motion for all calculated wave conditions, as shown in Figs.**3.24**(a)~**3.24**(e), the above-mentioned decrease tendency is further confirmed.

Figures **3.25** and **3.26** show the calculated results of floating panel motion without considering damping term and considering damping term for wave conditions of h=0.425m,H=0.04m, and wave periods of T=2.24s,1.00s and 0.75s. The damping coefficients are set equal to 0.70 for the developed equation of motion. It is found from Figs.**3.25** and **3.26** that when wave period is close to natural period, the calculated results based on the developed equation of motion show a very good agreement with measured ones, whereas disagreements are found from the comparison of the calculated results without considering damping term and measure ones. Furthermore, it is revealed that the impact of friction force between the steel frame and the floating panel on the motion of floating panel is larger when wave period is close to the natural period of floating panel motion. As a result, the validation of the developed equation of motion is verified.

Figures **3.27** and **3.28** show the relation of the normalized period ratio of wave period and the natural period of floating panel motion to the normalized amplitude and phase lag (normalized amplitude: the ratio of the amplitude of floating panel motion A_s and the amplitude of the water surface elevation in front of the seawall A_{wf}), respectively. Good agreements between the calculated results with measured ones seen in both Figs. **3.27** and **3.28** confirm the validity of the proposed model. Furthermore, it is found from Fig.**3.27** that if the ratio of the natural period of floating panel motion and wave period T_s/T is small, the normalized amplitude is close to 1, meaning that the amplitude of floating panel motion is approximate the amplitude of the water surface elevation in front of the panel. When T_s/T is close to 1, the normalized amplitude is found reaching a peak, which is slightly larger than 1. After that, the normalized amplitude decrease gradually when T_s/T is larger than 1. On the other hand, it is seen from Fig.**3.28** that when the normalized period ratio increases, the phase lag increases rapidly. Consequently, the natural period of floating panel motion is found influencing on not only the amplitude of floating panel motion but also the phase lag, which are very significant factor for wave overtopping reduction performance.

(3) Pressure Acting on the Bottom of the Floating Panel

Figures **3.29**(a)~ **3.29**(e) shows the temporal variation of pressure acting on the bottom of the floating panel in terms of calculated and measured ones for wave conditions of wave height H=0.04m and 0.10m, respectively. Note that the hydrostatic pressure at the initial time, meaning that when the floating panel is as initial position, is not considered in these results. It is found from Figs.**3.29**(a)~**3.29**(c)that the calculated results are in good agreement with measured ones.

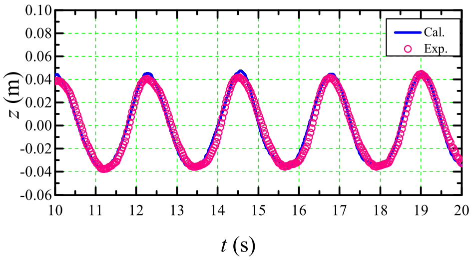

(a) T=2.24s

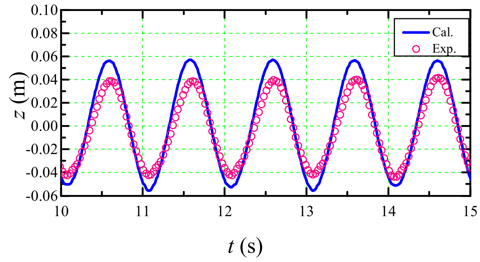

(b) T=1.00s

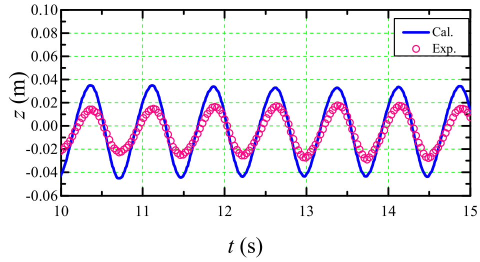

(c) T=0.75s

Figure **3.25** Variation of floating panel motion without considering damping term for different wave periods (h=0.425m,H=0.04m)

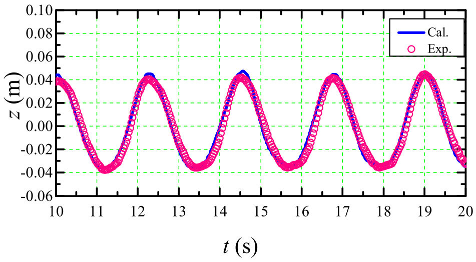

(a) T=2.24s

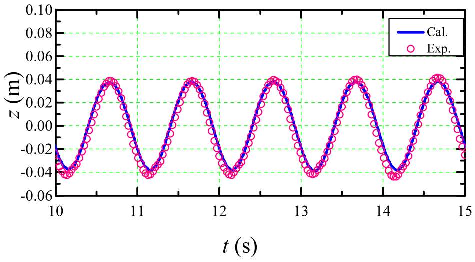

(b) T=1.00s

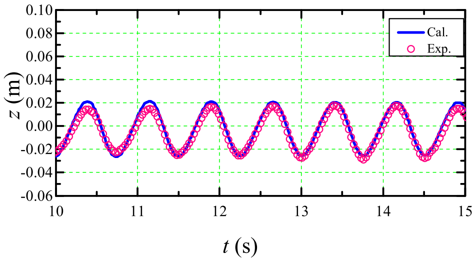

(c) T=0.75s

Figure **3.26** Variation of floating panel motion considering damping term for different wave periods (h=0.425m,H=0.04m)

In Figs.**3.29**(d) and **3.29**(e), however, disagreements between the calculated ones and measure ones are shown. It is explained that the occurrence of this difference in values accounting for 200Pa caused by the difference between the calculated water surface elevation results and measures results, as shown in Fig**3.22**

In order to investigate the temporal variation of pressure acting on the bottom of the floating panel and water surface elevation, as well as floating panel motion, all above-mentioned parameters are superimposed in the time axis, as shown in Figures **3.30**(a)~**3.30**(e). The phase lag between water surface elevation and the pressure is found to decrease when wave period is close to the natural period of floating panel. The variation of this phase lag is opposite to that of the phase lag between water surface elevation and floating panel motion, which is found to

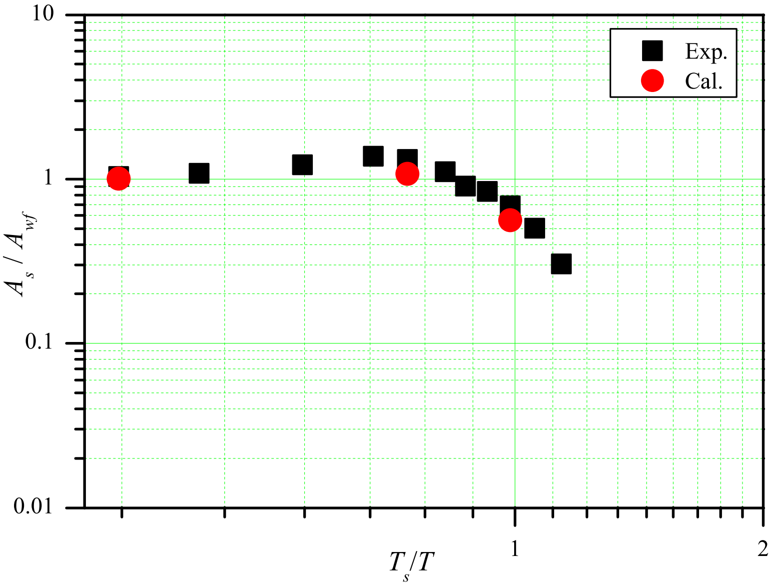

Figure **3.27** The relation of the normalized amplitude A_s/A_{wf} to T_s/T

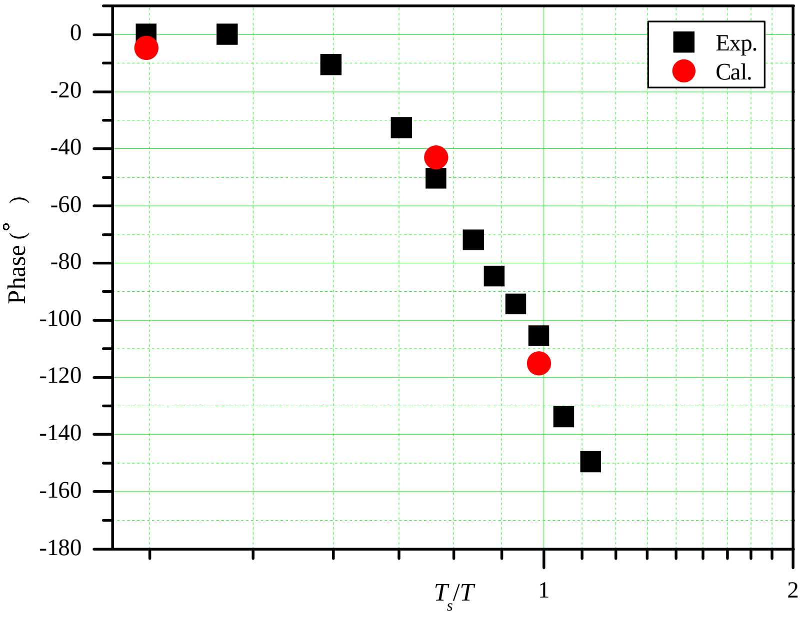

Figure **3.28** The relation of the phase lag to T_s/T

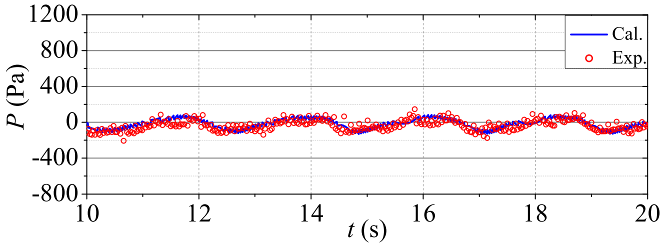

(a) h=0.425m,H=0.04m,T=2.24s

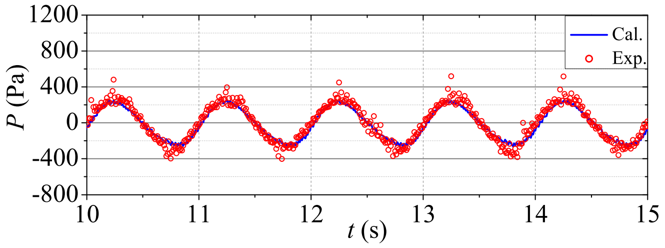

(b) h=0.425m,H=0.04m,T=1.00s

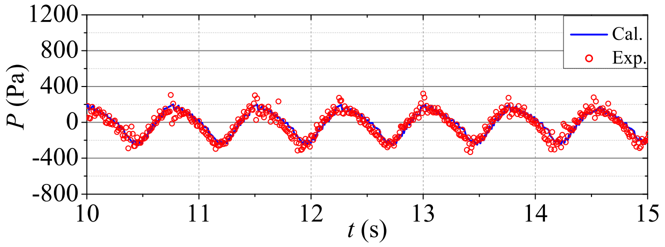

(c) h=0.425m,H=0.04m,T=0.75s

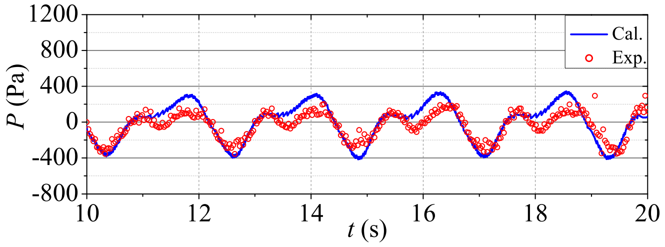

(d) h=0.425m,H=0.10m,T=2.24s

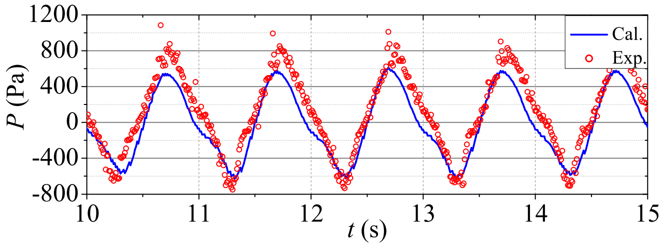

(e) h=0.425m,H=0.10m,T=1.00s

Figure **3.29** Temporal variation of pressure acting on the bottom of floating panel

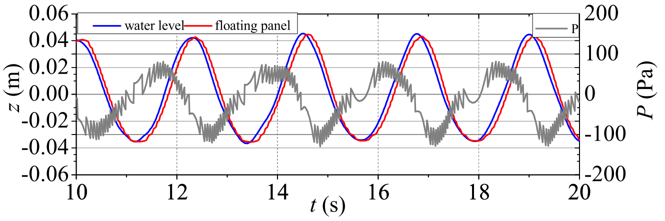

(a) h=0.425m,H=0.04m,T=2.24s

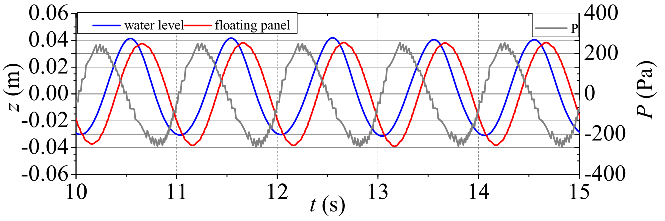

(b) h=0.425m,H=0.04m,T=1.00s

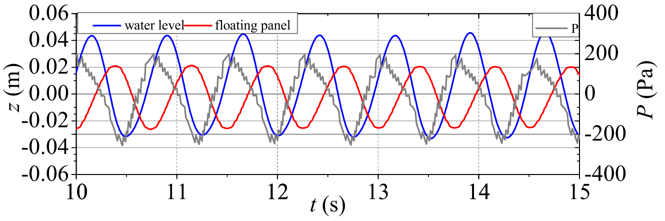

(c) h=0.425m,H=0.04m,T=0.75s

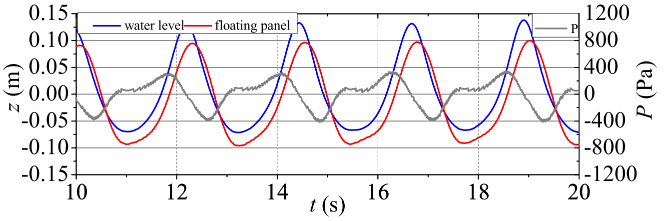

(d) h=0.425m,H=0.10m,T=2.24s

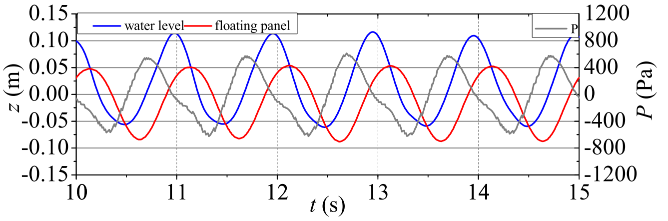

(e) h=0.425m,H=0.10m,T=1.00s

Figure **3.30** Temporal variation of pressure acting on the bottom of floating panel, water surface elevation and floating panel motion increase when wave period is close to the natural period of floating panel.

3.4 Conclusions

Nonlinear interaction between wave and a movable structure, which is named floating panel for wave overtopping reduction, was discussed experimentally and numerically in this chapter. First, the laboratory experiments were examined in order to point out characteristic of wave overtopping reduction and dynamic behavior of a floating panel for wave overtopping reduction countermeasure, in which a floating panel was installed to the front of an existing upright seawall. The equation of motion was then modified to realize the dynamic behavior of floating panel under wave action. The proposed numerical model was furthermore used to analyze nonlinear interaction of wave and the floating panel. The verification of the numerical results was also implemented through the comparisons between calculated and measured ones. Main conclusions are stated as follows:

1. It was found from the experimental examination that floating panel had a great effect on wave overtopping reduction under regular wave action by following the water surface elevation in front of the seawall. Wave overtopping characteristics were classified in two types of Type 1 and Type 2. Type 1 is that water mass overtops floating panel. Type 2 represents that water overflow into top of the seawall through the gap between the seawall and floating panel. Furthermore, the phase lag between floating panel motion in the vertical direction and water surface elevation in front of the seawall was seen to increase when incident wave period was close to the natural period of floating panel motion in the vertical direction. A collision between floating panel and steel frame on the floating panel motion was also observed.

2. In order to consider the influence of the friction force induced by the collision between the floating panel and the steel frame on the floating panel motion, a damping term was introduced into the motion equation of floating panel in the vertical direction. Rotational and horizontal motion, which were seen small compared with vertical motion in the laboratory experiments, were neglected.

3. Nonlinear interaction and dynamic behavior of floating panel under wave action were numerically investigated in terms of variation of floating panel motion and water surface elevation, wave overtopping characteristics, and pressure acting on the front and the back side of the panel. In terms of two former investigations, the following results were obtained: 1) Floating panel follows water surface elevation in front of the seawall; 2) The phase lag between the water surface elevation and floating panel motion increases when wave period was close to the

natural period of floating panel in the vertical direction; 3) Wave overtopping characteristics were influenced by the relationship between water surface elevation and floating panel motion. These results were seen consistency qualitatively with experimental ones. The proposed model was, therefore found capable of reproducing the nonlinear interaction and dynamic behavior of floating panel under wave action. In terms of the investigation on pressure acting on the sides of floating panel, it was found that when wave period was far from the natural period of floating panel in the vertical direction, the pressure had a same distribution with hydrostatic distribution, as in normal thought. When wave period was close to the natural period, however, a significant difference between the pressure acting on the front side and that on the back side of the floating panel was revealed. It was proven that this revelation is very important for designing a floating panel. Note that the pressure acting on the sides of the floating panel has not been obtained in the laboratory experiment because of the difficulties in installing the pressure gauges on these sides, the validity of the proposed model was furthermore stated.

4. Numerical results were compared with experiment results in term of variation of water surface elevation in front of the panel, dynamic behavior of floating panel under wave action, pressure acting on the bottom of the floating panel. Through good agreement between the calculated and measured results, the validity and the utility of the proposed model was confirmed.

CHAPTER 4
GENERAL CONCLUSIONS AND PERSPECTIVE

In order to explore and exploit natural resources of seas and oceans such as water, food and energy as well as to provide means for transport and other substructures, variety of coastal and offshore structures have been built and utilized. No matter what type they are and what functions they are used for, one thing is common, they are all under wave actions, which have been noted nonlinear, severe in harsh sea conditions, dominant compared with other impacts such as wind and current. Understanding the interaction between wave and structure is therefore, one of the most important requirements to design and install safe, functional and economical coastal/offshore structures. In the present study, this motivation was realized by developing a numerical wave tank model capable of reproducing nonlinear wave-structure interaction for both fixed and movable structures, considering the interaction between air and water phase. Starting with the idea that the interaction between wave and coastal and offshore structures may be considered as representation of the interaction among the solid phase (structures), the gas phase (air) and the liquid phase (water), a multiphase flow model with solid-gas-liquid interaction was used to developed a numerical wave tank. The validity and utility of the proposed numerical wave tank model were then verified by a series of simulations on wave propagation and energy dissipation zone effects, wave propagation over a submerged dike and wave breaking process on the different uniform slopes. Next, the proposed model was utilized to analyze the nonlinear interaction between wave and a floating panel for wave overtopping reduction. This chapter aims at presenting a review on main findings of conducted works as well as discussing future works.

Background of nonlinear interaction between coastal/offshore structures was introduced in chapter 1. A literature review on numerical wave tank models was furthermore conducted. All discussions showed the necessity of a new numerical wave tank, which can model the nonlinear interaction between waves and both fixed and movable structures, considering the interaction between air and water phase.

Chapter 2 developed a numerical wave tank based on a multiphase flow model with solid-gas-liquid interaction proposed by Kawasaki and co-workers (2005~2009), in which a non-reflective wave generator proposed by Kawasaki et al. (1998), and energy dissipation zone treatments presented by Cruz et al (1993) and Hinatsu (1992) were employed to realize the numerical wave tank. In order to enhance the computational accuracy, a CIP-CSL2 (Constrained Interpolation Profile- Conservative Semi-Lagragian 2) method and the third-order Adams-Bashforth scheme were incorporated in the numerical model. Key figures of the proposed numerical wave tank are summarized as follows,

1. In the present numerical wave tank model, solid, gas and liquid phase might represent for structures, air and water, respectively. As a result, it can be said that the interaction between air and water was considered in this numerical wave tank model.

2. A non-reflective wave generator was installed in the analysis domain, and energy dissipation zones were employed at both sides of the computational domain to dissipate waves from the analysis domain.

3. The flow is represented by one set of governing equations, and therefore no special treatment is needed for the boundary among three phases. This figure might enable the numerical model to advantageously simulate interaction between wave and both fixed and unfixed structures.

Besides, the validity and the utility of the proposed numerical wave tank were confirmed through a series of simulations in chapter 2. For the verification part of wave propagation, good agreements between calculated and theoretical results in terms of water surface profile and water particle velocities verified the validity of non-reflective wave generation method as well as the interface capturing scheme tangent CIP. On the other hand, the examination of spatial distribution of water surface elevation revealed the validity of energy dissipation zone treatments. For the analysis of wave propagation over a submerged dike and the simulation of wave breaking process on different uniform slopes, good agreement between numerical and experimental results confirmed the capability of the model in analyzing nonlinear interaction between wave and a fixed structure. Compared with previous numerical wave tanks model, the present numerical wave tank shows advantages in simply treating boundaries of solid bodies and in considering the interaction between air and water phase. Moreover, it was suggested from the analysis of wave propagation over a submerged dike that the relationship between the generation of higher harmonic and the spatial distribution of the large velocities on the water surface and on the top of the submerged dike should be considered in practical design because these large velocities might cause the erosion of the material on the top of a submerged dike. In terms of pressure acting on the top of the dike, the difference between the pressure acting on the top layer at the weather side and that at the lee side should be also noted because this difference might result in the sliding failure mode of the dike.

A countermeasure for wave overtopping reduction including a vertical seawall and a floating panel installed in the steel frame, which is attached at the upright of the seawall, have been investigated by Kawasaki and co-worker since 2010. Funahashi (2011) experimentally and analytically discussed the wave overtopping reduction effect of a floating panel with different cross sections under both regular and irregular wave, whereas nonlinear interaction between wave and a floating panel for wave overtopping reduction under regular wave action, whose cross section is rectangle, were experimentally and numerically studied in chapter 3 of this study. First, the laboratory experiments were examined in order to point out characteristic of wave overtopping reduction and dynamic behavior of a floating panel. The equation of motion was then modified to realize the dynamic behavior of floating panel under wave action by proposing a damping term, which was assumed representing the friction force induced by the collision between floating panel and steel frame. The newly proposed numerical model was then used to analyze nonlinear interaction between wave and the floating panel under regular wave action. Verifications of the numerical model were furthermore implemented through the comparisons between calculated and measured results. Good agreements between the numerical and measured ones confirmed the validity of the proposed model. Main findings about nonlinear interaction between wave and the floating panel are stated as follows,

1. It was found from experimental examination that floating panel had a great effect on wave overtopping reduction under regular wave action by following the water surface elevation in front of the seawall. Wave overtopping characteristics were classified in two types of Type 1 and Type 2. Type 1 is that water mass overtops floating panel. Type 2 represents that water overflow into top of the seawall through the gap between the seawall and floating panel. Furthermore, the phase lag between floating panel motion in the vertical direction and water surface elevation in front of the seawall was seen to increase when incident wave period was close to the natural period of floating panel motion in the vertical direction. A collision between floating panel and steel frame on the floating panel motion was also observed.

2. Nonlinear interaction and dynamic behavior of floating panel under wave action were numerically investigated in terms of variation of floating panel motion and water surface elevation,

wave overtopping reduction effects, and pressure acting on the front and the back side of the panel. In terms of two former investigations, the following results were obtained: 1) Floating panel was confirmed to have a good reduction effects of wave overtopping under wave actions by following the water surface elevation in front of the seawall; 2) The phase lag between the water surface elevation and floating panel motion increases when wave period was close to the natural period of floating panel in the vertical direction; These results were seen consistency qualitatively with experimental ones. The proposed model was, therefore found capable of reproducing the interaction and dynamic behavior of floating panel under wave action. In terms of the investigation on pressure acting on the sides of floating panel, it was found that when wave period was far from the natural period of floating panel in the vertical direction, the pressure had a same distribution with hydrostatic distribution, as in normal thought. When wave period was close to the natural period, however, a significant difference between the pressure acting on the front side and that on the back side of the floating panel was revealed. It was proven that this revelation is very important for designing a floating panel. Note that the pressure acting on the sides of the floating panel has not been obtained in the laboratory experiment because of the difficulties in installing the pressure gauges on these sides, the validity of the proposed model was further stated.

Regarding the perspective of the proposed numerical wave tank model, some further works are mentioned here. First, although dynamic behavior of floating panel under wave action was well reproduced with the consideration of the friction force by introducing a constant damping term into the equation of motion, another fully numerical approach, in which a collision term variable with motions of floating body, should be furthermore studied. On the other hand, it was shown from this study that the numerical model is capable of reproducing wave breaking and wave overtopping considering the interaction between air and water phase. This revelation suggests that the proposed model can be available to simulate the interaction between waves and structure considering wind effects, a development of the present model to realize this problem therefore should be pursued. Moreover, although a three-dimensional numerical wave tank was developed, three-dimensional applications have not been addressed. The validity and utility of the numerical wave tank model in analyzing three-dimensional applications such as generating multi-directional wave and nonlinear interaction between wave and a three-dimensional floating body therefore should be further investigated.

REFERENCE

Ashgriz, N. & Poo, J., 1991. FLAIR: Flux line-segment model for advection and interface reconstruction. *Journal of Computational Physics*, 93(2), pp.449-68.

Atomic Energy Society of Japan, 1993. *Numerical analysis of two-phase flow*. Asakura, Japan.

Baraff, D., 1997. An introduction to physically based modeling: Rigid body simulation I—unconstrained rigid body dynamics. *SIGGRAPH Course Notes*.

Battjes, J., 2005. Surf similarity. *Proceedings of the 14th Coastal Engineering Conference*, American Society of Civil Engineers, pp.466-79.

Beji, S. & Battjes, J., 1993. Experimental investigation of wave propagation over a bar. *Coastal Engineering*, 19(1-2), pp.151-62.

Beji, S. & Battjes, J., 1994. Numerical simulation of nonlinear wave propagation over a bar. *Coastal Engineering*, 23(1-2), pp.1-16.

Bindoff, N. et al., 2007. *Observations: Oceanic climate change and sea level*. Cambridge University Press.

Boo, S., Kim, C. & Kim, M., 1994. A numerical wave tank for nonlinear irregular waves by 3-D higher order boundary element method. *International Journal of Offshore and Polar Engineering*, 4(4), pp.265-72.

Brackbill, J., Kothe, D. & Zemach, C., 1992. A continuum method for modeling surface tension. *Journal of computational physics*, 100(2), pp.335-54.

Brennen, C., 2005. Fundamental of multiphase flow. Cambridge Univ Pr., ISBN-13 978-0-521-84804-6.

Brorsen, M. & Larsen, J., 1987. Source generation of nonlinear gravity waves with the boundary integral equation method. *Coastal Engineering*, 11(2), pp.93-113.

Buchner, B., 2007. The impact of extreme wave loading on offshore platforms and FPSOs. *Presentation*, Maritime Research Institute Netherlands (MARIN).

Buchner, B. & Bunnik, T., 2007. Extreme wave effects on deepwater floating structures. *Offshore Technology Conference*, OTC-18493, Houston.

Cornett, A., Li, Y. & Budvietas, A., 1999. Wave overtopping at chamfered and overhanging vertical structures. *Proc. International Workshop on Natural Disasters by Storm Waves and Their Reproduction in Experimental Basins*, Kyoto, Japan, pp.45-58.

Cruz, E., 1993. Boundary condition for non-linear gravity equations. *Proc. of Coastal Engineering*, 40, pp.46-50.

Dean, R. & Dalrymple, R., 1991. *Water wave mechanics for engineers and scientists*. World Scientific Pub Co Inc.

Faltinsen, O., Newman, J. & Vinje, T., 1995. Nonlinear wave loads on a slender vertical cylinder. *Journal of Fluid Mechanics*, 289(-1), pp.179-98.

Ferrant, P., 1995. Time domain computation of nonlinear diffraction loads upon three dimensional floating bodies. *Proc. 5th Intl. O shore and Polar Engng. Conf.*, 3, pp.280-88.

Fletcher, C., 2009. Sea level by the end of the 21st century: A review. *Shore ¥& Beach*, 77(4), p.4.

Funahashi, T.2011. Development of Floating Panel for Wave Overtopping Reduction and Its Effectiveness. *Master Thesis,* Nagoya University. 99p.

Geeraerts, J. et al., 2006. Reduction of wave overtopping at sea dikes: Stilling wave basin. *Proceedings of 30th International Conference on Coastal Engineering*, pp.4680-91.

Germano, M., Piomelli, U., Moin, P. & Cabot, W., 1991. A dynamic subgrid-scale eddy viscosity model. *Physics of Fluids A: Fluid Dynamics*, 3, p.1760.

Goda, Y., 1975. Irregular wave deformation in the surf zone. *Coastal engineering in Japan*, 18, pp.13-26.

Grilli, S.T., Skourup, J. & Svendsen, I.A., 1989. An efficient boundary element method for nonlinear water waves. *Engineering Analysis with Boundary Elements*, 6(2), pp.97-107.

Hieu, P., Katsutoshi, T. & Ca, V., 2004. Numerical simulation of breaking waves using a two-phase flow model. *Applied Mathematical Modelling*, 28(11), pp.983-1005.

Hieu, P. & Tanimoto, K., 2006. Verification of a VOF-based two-phase flow model for wave breaking and wave-structure interactions. *Ocean engineering*, 33(11-12), pp.1565-88.

Hinatsu, M., 1992. Numerical Simulation of Unsteady Viscous Nonlinear Waves Using Moving Grid System Fitted on a Free Surface. *Journal of the Kansai Society of Naval Architects, Japan*, 217, pp.1-11.

Hirt, C. & Nichols, B., 1981. Volume of fluid (VOF) method for the dynamics of free boundaries* 1. *Journal of computational physics*, 39(1), pp.201-25.

Huang, C. & Dong, C., 1999. Wave deformation and vortex generation in water waves propagating over a submerged dike. *Coastal engineering*, 37(2), pp.123-48.

Hu, C. & Kashiwagi, M., 2004. A CIP-based method for numerical simulations of violent free-surface flows. *Journal of marine science and technology*, 9(4), pp.143-57.

Hu, C., Kashiwagi, M. & Faltinsen, O., 2005. 3-D Numerical Simulation of Freely Moving Floating Body by CIP Method. *Proc. ISOPE*, 4, pp.674-79.

Idelsohn, S., Onate, E., Pin, F. & Calvo, N., 2006. Fluid-structure interaction using the particle finite element method. *Computer methods in applied mechanics and engineering*, 195(17-18), pp.2100-23.

Jr, C.G., 1968. Breaker type classification on three laboratory beaches. *Journal of Geophysical Research*, 73(12), pp.3651-59.

Kashiwagi, M., 2000. Non-linear simulations of wave-induced motions of a floating body by means of the mixed Eulerian-Lagrangian method. *Proceedings of the Institution of Mechanical Engineers, Part C: Journal of Mechanical Engineering Science*, 214(6), pp.841-55.

Kawasaki, K., 1999. Numerical simulation of breaking and post-breaking wave deformation process around a submerged breakwater. *Coastal Engineering Journal*, 41(3), pp.201-23.

Kawasaki, K., 2005a. Numerical Model of 2-D Multiphase Flow with Solid-Liquid-Gas Interaction. *International Journal of Offshore and Polar Engineering*, 15(3), pp.198-203.

Kawasaki, K. 2005b. Numerical simulation of solid-gas-liquid phase flow in a three-dimensional field. *Proceedings of 3rd International Conference on Asian and Pacific Coasts*, 1868-1879.

Kawasaki, K. & Hakamata, M., 2006. Numerical analysis of time-changing wave force acting on drifting rigid structure with solid-gas-liquid phase flow model. *Proceedings of 30th International Conference on Coastal Engineering*, pp.4507-19.

Kawasaki, K., Ogiso, K., Takasu, Y. (2009): Bingham Fluid Flow Simulation with Three-dimensional Multiphase Flow Numerical Model "DOLPHIN-3D", *Proceedings of 5th International Conference on Asian and Pacific Coasts*, Vol.4, pp.121-127.

Kawasaki, K. & Mizutani, N., 2007. Numerical simulation of bore-induced dynamic behavior of rigid body using 2-D multiphase flow numerical model. *Proceedings of International Conference on Coastal Structures 2007*, pp.1477-88.

Kawasaki,K., Dinh Ut, Han, Funahashi, T. and Fukumoto, T. 2011. Experimental Investigation on Adaptive Countermeasure Using Floating Panel for Wave Overtopping Reduction, *International Offshore and Polar Engineering Conference* (in press).

Kim, C., Clement, A. & Tanizawa, K., 1999. Recent research and development of numerical wave tanks-a review. *International Journal of Offshore and Polar Engineering*, 9(4), pp.241-56.

Kortenhaus, A., Haupt, R. & Oumeraci, H., 2001. Design aspects of vertical walls with steep foreland slopes. *Proc. of the Int. Conf. on Coastlines, Structures and Breakwaters, ICE, London*, pp.221-32.

Lin, P. & Liu, P., 1998. A numerical study of breaking waves in the surf zone. *Journal of Fluid Mechanics*, 359(-1), pp.239-64.

Longuet-Higgins, M. & Cokelet, E., 1976. The deformation of steep surface waves on water. I. A numerical method of computation. *Proceedings of the Royal Society of London. A. Mathematical and Physical Sciences*, 350(1660), p.1.

Madsen, P., Murray, R. & Sorensen, O., 1991. A new form of the Boussinesq equations with improved linear dispersion characteristics. *Coastal Engineering*, 15(4), pp.371-88.

Ma, Q., Wu, G. & Taylor, R.E., 2001. Finite element simulation of fully non-linear interaction between vertical cylinders and steep waves. Part 1: Methodology and numerical procedure. *International journal for numerical methods in fluids*, 36(3), pp.265-85.

Ma, Q. & Yan, S., 2009. QALE-FEM for numerical modelling of non-linear interaction between 3D moored floating bodies and steep waves. *International Journal for Numerical Methods in Engineering*, 78(6), pp.713-56.

Mehaute, B.L. & Webb, L., 1964. Periodic gravity waves over a gentle slope at a third order of approximation. *Proceeding of the 9th International Conference on Coastal Engineering, ASCE*, pp.23-40.

Moan, T., 2003. Marin structures for the future. *Lecture, Centre for Offshore Researchtre for Offshore Research*, National Univisity of Singapor; CORE Report No.2003-01.

Moan, T., 2005. Safety of offshore structures. *Lecture, Centre for Offshore Research, Cetre for Offshore Research*, National University of Singapor, CORE Report No.2005-04.

Moan, T., 2007. Accident and near-misses in the offshore oil and gas industry-how and why? *Lecture, Centre for Offshore Research*, National University of Singapor.

Nakamura, T., Tanaka, R., Yabe, T. & Takizawa, K., 2001. Exactly conservative semi-Lagrangian scheme for multi-dimensional hyperbolic equations with directional splitting technique. *Journal of computational physics*, 174(1), pp.171-207.

Nakamura, T. & Yabe, T., 1999. Cubic interpolated propagation scheme for solving the hyper-dimensional Vlasov-Poisson equation in phase space. *Computer physics communications*, 120(2-3), pp.122-54.

Norsk-Standard, 2007. Actions and action effects. *N-003*, 1.

Ohyama, T. & Nadaoka, K., 1991. Development of a numerical wave tank for analysis of nonlinear and irregular wave field. *Fluid Dynamics Research*, 8(5-6), pp.231-51.

Ohyama, T. & Nadaoka, K., 1994. Transformation of a nonlinear wave train passing over a submerged shelf without breaking. *Coastal engineering*, 24(1-2), pp.1-22.

Peregrine, D., 1967. Long waves on a beach. *Journal of Fluid Mechanics*, 27(04), pp.815-27.

Salvetti, M. & Banerjee, S., 1995. A priori tests of a new dynamic subgrid-scale model for finite-difference large-eddy simulations. *Physics of Fluids*, 7, p.2831.

Sawaragi, T., Deguchi, I. & Park, S., 1988. Reduction of Wave Overtopping Rate by the Use of Artificial Reefs. *Proceedings of the International Twenty-first Coastal Engineering Conference*, pp.335-49.

Sethian, J., 1999. Level set methods and fast marching methods: Evolving interfaces in computational geometry, fluid mechanics, computer vision, and materials science. *Cambridge Univ Pr., ISBN 0-521-64557-3.*, (3).

She, K., Created, C. & Easson, W., 1992. Development of a two dimensional numerical wave tank. *2nd Int. Conffrence Offshore and Polar Engineering, USA*.

Sheikh, R. & Swan, C., 2005. The Interaction Between Steep Waves and a Vertical, Surface-Piercing Column. *Journal of Offshore Mechanics and Arctic Engineering*, 127, p.31.

Shuto, N., 1974. Nonlinear long waves in a channel of varied section. *Coastal engineering in Japan*, 17, pp.1-12.

Smagorinsky, J., 1963. General circulation experiments with the primitive equations. *Monthly weather review*, 91(3), pp.99-164.

Sorensen, R., 2006. *Basic coastal engineering*. Springer Verlag.

Stansberg, C., Kristiansen, T., Hansen, E. & Rortveit, G., 2005. Extreme wave amplification and impact loads on offshore structures., 2005.

Sussman, M., Smereka, P. & Osher, S., 1994. A level set method for computing solutions to incompressible two-phase flow. *J. Comput. Phys*, 114(1), pp.146-59.

Svendsen, I., 1987. Analysis of surf zone turbulence. *Journal of Geophysical research*, 92(C5), pp.5115-24.

Swan, C., Taylor, P. & Langen, H.V., 1997. Observations of wave-structure interaction for a multi-legged concrete platform. *Applied ocean research*, 19(5-6), pp.309-27.

Takewaki, H., Nishiguchi, A. & Yabe, T., 1985. Cubic interpolated pseudo-particle method (CIP) for solving hyperbolic-type equations. *Journal of Computational Physics*, 61(2), pp.261-68.

Tanizawa, K., 2000. The state of the art on numerical wave tank., 2000.

Ting, F. & Kirby, J., 1994. Observation of undertow and turbulence in a laboratory surf zone. *Coastal Engineering*, 24(1-2), pp.51-80.

Tsai, C., Chen, H., Hwung, H. & Huang, M., 2005. Examination of empirical formulas for wave shoaling and breaking on steep slopes. *Ocean engineering*, 32(3-4), pp.469-83.

Unverdi, S. & Tryggvason, G., 1992. A front-tracking method for viscous, incompressible, multi-fluid flows. *Journal of Computational Physics*, 100(1), pp.25-37.
U.S. Army Corps of Engineers', 2003. Coastal Engineering Manual.

Welch, J., Harlow, F., Shannon, J. & Daly, B., n.d. A computing technique for solving viscous, incompressible, transient fluid-flow problems involving free surfaces. *Report LA-3425 (Los Alamos Scientific Laboratory, Los Alamos, New Mexico, 1966)*.

Xiao, F., Yabe, T., Ito, T. & Tajima, M., 1997. An algorithm for simulating solid objects suspended in stratified flow. *Computer physics communications*, 102(1-3), pp.147-60.

Xu, H. & Yue, D., 1992. Numerical study of three-dimensional overturning water waves., 1992.

Yabe, T. & Aoki, T., 1991a. A universal solver for hyperbolic equations by cubic-polynomial interpolation I. One-dimensional solver. *Computer Physics Communications*, 66(2-3), pp.219-32.

Yabe, T. & Aoki, T., 1991b. A universal solver for hyperbolic equations by cubic-polynomial interpolation I. Two and Three-dimensional solver. *Computer Physics Communications*, 66(2-3), pp.233-42.

Yabe, T., Tanaka, R., Nakamura, T. & Xiao, F., 2001. An exactly conservative semi-Lagrangian scheme (CIP-CSL) in one dimension. *Monthly weather review*, 129(2), pp.332-44.

Yabe, T. & Xiao, F., 1993. Description of complex and sharp interface during shock wave interaction with liquid drop. *JOURNAL-PHYSICAL SOCIETY OF JAPAN*, 62, pp.2537-37.

Yabe, T., Xiao, F. & Utsumi, T., 2001. The constrained interpolation profile method for multiphase analysis. *Journal of Computational Physics*, 169(2), pp.556-93.

Yan, S. & Ma, Q., 2007. Numerical simulation of fully nonlinear interaction between steep waves and 2D floating bodies using the QALE-FEM method. *Journal of Computational Physics*, 221(2), pp.666-92.

Youngs, D., 1982. Time-dependent multi-material flow with large fluid distortion. *Numerical methods for fluid dynamics*, ed. Morton, K.M. and Baines, M.J., Academic Press(1), p.517.

Zhang, S., Yue, D. & Tanizawa, K., 1996. Simulation of plunging wave impact on a vertical wall. *Journal of Fluid Mechanics*, 327(-1), pp.221-54.

Zhao, Q., Armfield, S. & Tanimoto, K., 2000. A Two-Dimensional Multi-Scale Turbulence Model for Breaking Waves.

Zhao, Q., Armfield, S. & Tanimoto, K., 2004. Numerical simulation of breaking waves by a multi-scale turbulence model. *Coastal engineering*, 51(1), pp.53-80.

Zhu, X., 2006. Application of the CIP method to strongly nonlinear wave-body interaction problems. Doctoral Dissertation, Norwegian University of Science Technology, Norway.

Zhu, X., Faltinsen, O. & Hu, C., 2007. Water entry and exit of a horizontal circular cylinder. *Journal of Offshore Mechanics and Arctic Engineering*, 129, p.253.